

Giant Magnetoresistance and Magnetic Properties of Ferromagnetic Hybrid Nanostructures

by

Conrad Rizal

A THESIS SUBMITTED IN PARTIAL FULFILLMENT OF
THE REQUIREMENTS FOR THE DEGREE OF

DOCTOR OF PHILOSOPHY

in

THE FACULTY OF GRADUATE STUDIES

(Electrical and Computer Engineering)

THE UNIVERSITY OF BRITISH COLUMBIA

(Vancouver)

April 2012

© Conrad Rizal, 2012

Abstract

Significant advances in the growth, measurement, and characterization methods in the field of nanoengineering have made Co-based magnetic hybrid (ferromagnetic and non-magnetic) nanostructures increasingly important for the development of giant magnetoresistance (GMR) sensors and high magnetic-moment biocompatible nanoparticles for use in the future magnetic technology. This thesis presents the growth, measurement, and characterization of magnetic hybrid nanostructures (multilayers, alloys, and nanoparticles) that exhibit interesting magnetoresistance (MR) and magnetic properties, which are significant in the development of state-of-the-art magnetic technology for use in the electronics and biomedical sectors.

Firstly, Co/Au multilayers have been grown on glass substrates using e-beam evaporation, and then Co/Ag and Co/Cu multilayers have been grown on polyimide substrates using pulsed-current deposition. All of these multilayers exhibited the GMR effect at room temperature. The maximum MR for Co/Au, Co/Ag, and Co/Cu multilayers was 2.1 %, 9.1 %, and 4.1 %, respectively. The e-beam evaporated multilayers exhibited strong magnetic anisotropy when the films were deposited at the angle of 45° . The electrodeposited multilayers exhibited strong magnetic anisotropy when strain was introduced externally. In both the cases, the GMR is strongly influenced by the ferromagnetic and nonmagnetic layer thicknesses and interfacial states between layers.

Secondly, novel nanocomposites Co nanoparticles embedded in Au matrix have been developed using pulsed-current deposition on polyimide substrates. They exhibited interesting MR, grain size, and saturation magnetization characteristics. The maximum room temperature GMR found was 4.6 %. X-ray diffraction, magnetization, and low temperature measurements suggest that a smaller grain size formed during higher current density correlates with the larger MR values for these nanocomposites.

Thirdly, high-magnetic-moment biocompatible FeCo nanostructures have been developed using pulsed-current deposition. The nanostructures exhibited saturation magnetization of up to 240 emu/g, which is much larger than the saturation magnetization of either Co or Fe.

The less expensive and highly sensitive GMR sensors if coated with specific probes, and if the target biomolecules are labelled with high-moment biocompatible nanoparticles presented in this thesis, the GMR sensors have potential for use in improving the early detection and treatment of chronic diseases (e.g., prostate and lung cancer) using biomagnetic technology.

Preface

The author of this thesis is solely responsible for writing this thesis, conducting the literature review, choosing research direction, carrying out experiment, developing theory, and interpreting results. Some of the measurement and characterization was carried out at the Advanced Engineering Material Laboratory, Muroran Institute of Technology, Japan by the author. The low temperature measurement results in Chapter 5 were obtained from the Center for Instrumental Analysis, Muroran Institute of Technology, Japan. The results presented in this thesis are published or accepted for publication in various top international journals. The coauthors of these papers provided guidance, theoretical analysis, and data analysis.

A version of Chapter 2 has been published. It consists of one peer-reviewed journal article.

- i. Rizal, C. (2007) Study of magnetic anisotropy and magnetoresistance effects in ferromagnetic Co/Au multilayer films prepared by e-beam evaporation. *Journal of Magnetism and Magnetic Materials*. 310: e646-e648

A version of Chapter 3 has been published or accepted for publication. Sections 3.3.1 through 3.3.5 consist of one published peer-reviewed journal article and Sections 3.3.6 through 3.3.11 consist of one accepted conference paper.

- i. Rizal, C. and Ueda, Y. (2009) Magnetoresistance and magnetic anisotropy properties of strain-induced Co/Ag multilayers. *IEEE Transactions on Magnetics*. 45: 2399-2402
- ii. Rizal, C., Gyawali, P., Kshatry, I. B., and Pokharel, R. K. (2011) Effect of strain on magnetoresistance and magnetic properties of Co(t_{Co})/Ag nanostructures. *Proceeding of the IEEE Nanotechnology Materials and Devices Conference (IEEE NMDC-2011)*. The Shela Jeju, Korea. 5 pages.

A version of Chapter 4 has been published or accepted. It consists of two peer-reviewed journal articles. Sections 4.3.2 through 4.3.5 consist of one published peer-reviewed journal article and Sections 4.3.6 through 4.3.8 consist of one accepted peer-reviewed journal article.

- i. Rizal, C. (2010) Magnetoresistance and magnetic properties of Co(t_{Co})/Cu multilayer films. *IEEE Transactions on Magnetics*. 46: 2394-2396
- ii. Rizal, C., Gyawali, P., Kshatry, I., and Pokharel, R.K. (2012) Strain-induced magnetoresistance and magnetic anisotropy properties of Co/Cu multilayers. *Journal of Applied Physics. American Institute of Physics*. 111: 07C107. 3 pages.

A version of Chapter 5 has been published. It consists of one peer-reviewed journal article.

- i. Rizal, C., Ueda, Y., and Pokharel, R.K. (2011) Magnetotransport properties of Co-Au granular alloys. *International Journal of Applied Physics and Mathematics*. 3:161-166

A version of Chapter 6 has been accepted as a conference paper.

- i. Rizal, C., Gyawali, P.R., and Pokharel, R.K. (2012) Magnetic and microstructural characterizations of Fe/FeCo nanostructures. *Digest of the IEEE International Magnetic Conference (Intermag-2012)*. Vancouver, BC, Canada. 2 pages.

Table of Contents

Abstract	ii
Preface	iii
Table of Contents	v
List of Tables	ix
List of Figures	x
List of Symbols	xv
List of Abbreviations	xvii
Acknowledgments	xviii
Dedication	xx
Chapter 1: Introduction	1
1.1 Films	4
1.1.1 Microstructural Characteristics	5
1.1.2 Electrical Characteristics	5
1.1.3 Mechanical Characteristics	5
1.1.4 Magnetic Characteristics	6
1.2 Electrical Resistivity and Magnetism	6
1.3 Magnetoresistance Types	7
1.3.1 Ordinary Magnetoresistance	7
1.3.2 Anisotropic Magnetoresistance.....	8
1.3.3 Giant Magnetoresistance	9
1.3.3.1 Mechanism of the GMR Effect in Multilayers.....	9
1.3.3.2 Mechanism of the GMR Effect in Granular Alloys	12
1.4 Experimental Survey of the GMR Effect in Multilayers	13
1.4.1 Current-in-the-Plane Geometry	13
1.4.2 Current-Perpendicular-to-the-Plane Geometry	17
1.5 Experimental Survey of the GMR Effect in Alloys.....	18
1.6 Induced Magnetic Anisotropy in Multilayers.....	19
1.6.1 Artificial Generation of Magnetic Anisotropy.....	20
1.6.1.1 Oblique Incidence Evaporation.....	20
1.6.1.2 Magnetic Annealing	20
1.6.1.3 Application of Strain	21
1.7 Electron Transport and Magnetic Anisotropy in 3- <i>d</i> Metals and Multilayers	22
1.7.1 Electrical Conductivity in Metals	22
1.7.2 Electron Mobility in Metals.....	22

1.7.3	Spin-dependent Resistivity in Ferromagnetic Metals	23
1.7.4	Spin-dependent Resistivity in Magnetic Multilayers	25
1.7.5	Magnetic Anisotropy	26
1.7.5.1	Anisotropy in Cubic Structures	26
1.7.5.2	Anisotropy in Hexagonal Structures	28
1.7.5.3	Anisotropy Measurement from Torque Curves	29
1.7.5.4	Anisotropy Measurement from Magnetization Curves	30
1.7.5.4.1	Magnetic Field towards Easy Axis	31
1.7.5.4.2	Magnetic Field towards Hard Axis	32
1.8	Film Preparation, Measurement, and Characterization	33
1.8.1	Classification of Film Preparation Methods	33
1.8.2	Measurement and Characterization	34
1.8.2.1	Experimental Methods	34
1.8.2.2	Composition and Thickness Analysis	35
1.8.2.3	X-ray Diffraction	35
1.8.2.4	Magnetoresistance Measurement	36
1.8.2.5	Vibrating Sample Magnetometer	37
1.8.2.6	Superconducting Quantum Interference Device	37
1.9	Thesis Outline	38
Chapter 2: Magnetoresistance Effect and Magnetic Properties of Co/Au Multilayers		39
2.1	Introduction	39
2.2	Experimental Procedure	40
2.3	Results and Discussions	40
2.3.1	Magnetic Anisotropy from Magnetization Curves	41
2.3.1.1	Normal Incidence Evaporation	41
2.3.1.2	Oblique Incidence Evaporation	42
2.3.2	Microstructural Analysis	43
2.3.3	Field Dependence of Magnetoresistance	43
2.3.3.1	Randomly Oriented Multilayers	44
2.3.3.2	Uniaxially Oriented Multilayers: Field Parallel to Easy Axis	45
2.3.3.3	Uniaxially Oriented Multilayers: Field Parallel to Hard Axis	46
2.3.4	Nonmagnetic Layer Thickness Dependence of the MR Ratio	47
2.3.5	Magnetic Layer Thickness Dependence of the MR Ratio	48
2.3.6	Magnetic Anisotropy and the MR Ratio	49
2.4	Summary	50
Chapter 3: Magnetoresistance Effect and Magnetic Properties of Co/Ag Multilayers		51
3.1	Introduction	51

3.2	Experimental Procedure	53
3.3	Results and Discussions	54
3.3.1	Magnetic Anisotropy from Magnetization Curves	55
3.3.1.1	Randomly Oriented Multilayers.....	55
3.3.1.2	Uniaxially Oriented Multilayers.....	56
3.3.2	Field Dependence of the MR Ratio in Low Fields	57
3.3.2.1	Randomly Oriented Multilayers.....	57
3.3.2.2	Uniaxially Oriented Multilayers: Current Parallel to Easy Axis	58
3.3.2.3	Uniaxially Oriented Multilayers: Current Parallel to Hard Axis.....	59
3.3.3	Cobalt Layer Thickness and the GMR Effect.....	60
3.3.4	Cobalt Layer Thickness and Magnetic Anisotropy.....	61
3.3.5	Magnetic Anisotropy and the MR Ratio.....	62
3.3.6	Magnetic Anisotropy and Torque Curves.....	63
3.3.7	Field Dependence of the MR Ratio in High Fields.....	64
3.3.8	Degree of Magnetic Anisotropy and the MR Ratio	65
3.3.9	Cobalt Layer Thickness and Electrical Characteristics.....	66
3.3.9.1	Randomly Oriented Multilayers.....	66
3.3.9.2	Uniaxially Oriented Multilayers.....	67
3.3.10	Strain and the Field Dependence of Magnetization	68
3.3.11	Strain and Degree of Anisotropy	69
3.4	Summary	69
Chapter 4: Magnetoresistance Effect and Magnetic Properties of Co/Cu Multilayers.....		71
4.1	Introduction	71
4.2	Experimental Procedure	72
4.3	Results and Discussions	73
4.3.1	Stress versus Strain Profile	73
4.3.2	Magnetic Anisotropy and the MR Ratio in Low Fields.....	74
4.3.3	Cobalt Layer Thickness and MR	75
4.3.4	Field Dependence of Magnetization	76
4.3.5	Cobalt Layer Thickness and Degree of Anisotropy.....	77
4.3.6	Degree of Anisotropy and the MR Ratio.....	77
4.3.7	Strain and Magnetic Anisotropy	79
4.3.8	Strain and the MR Ratio	79
4.4	Summary	81
Chapter 5: Magnetoresistance Properties of Co-Au Granular Alloy Films.....		82
5.1	Introduction	82
5.2	Experimental Procedure	83

5.3	Results and Discussions	84
5.3.1	Compositional Analysis.....	84
5.3.2	Composition Dependence of the MR Ratio.....	85
5.3.3	Composition Dependence of the Saturation Magnetization.....	86
5.3.4	Microstructural Analysis	87
5.3.5	Estimation of Cobalt Grain Size	88
5.3.5.1	Grain Size Estimation at 3 mA/cm ² (As-deposited).....	88
5.3.5.2	Grain Size Estimation at 5 mA/cm ² (As-deposited).....	89
5.3.5.3	Grain Size Estimation at 5 mA/cm ² (Annealed).....	90
5.4	Summary	91
Chapter 6: Magnetic Properties of FeCo Nanostructures		92
6.1	Introduction	92
6.2	Experimental Procedure	93
6.3	Results and Discussions	93
6.3.1	Saturation Magnetization.....	94
6.3.2	Microstructural Analysis	94
6.4	Summary	95
Chapter 7: Summary, Conclusions, Potential Applications, and Future Prospects		96
7.1	Summary	96
7.2	Conclusions	97
7.3	Potential Applications	98
7.4	Future Prospects	99
References		100
Appendix A: Vibrating Dipole Moment		109
Appendix B: Measurement and Data Analysis		111

List of Tables

Table 1-1	Reports of the GMR effect in multilayers	16
Table 1-2	Reports of the GMR effect in alloys	18
Table 1-3	Relationships between the magnetic moments and their orientations.	28

List of Figures

Figure 1-1	Classification of thin films based on their dimensions.....	4
Figure 1-2	Temperature dependence of resistivity of ferromagnetic Ni and paramagnetic Pd [51].	7
Figure 1-3	(a) Schematic of a film showing the direction of the magnetization and the current (b) resistivity versus magnetic field.	8
Figure 1-4	The GMR effect in ferromagnetic hybrid nanostructures.	9
Figure 1-5	Cross-sectional view of a Co/Cu multilayer and the scattering of the 4-s conduction electrons by the local magnetic moments (a) at the zero magnetic field (b) at the applied magnetic field, H	10
Figure 1-6	Isotropic multilayer (i.e., magnetic moments are randomly orientated) and (b) anisotropic multilayer (i.e., magnetic moments are uniaxially oriented).	11
Figure 1-7	The GMR mechanism in the granular alloys consisting of superparamagnetic (circles) and ferromagnetic (ellipsoids) nanoparticles in the non-magnetic matrix [59].	12
Figure 1-8	The GMR effect in Fe/Cr multilayers [62].	13
Figure 1-9	Magnetization curves of Fe/Cr multilayers [62]	14
Figure 1-10	Cu layer thickness dependence of the MR ratio for Co/Cu multilayers (the subscript 30 indicates the number of bilayers in the film) [63].	15
Figure 1-11	Schematic of the array of Co/Cu nanowires in an insulating polymer matrix [78].	17
Figure 1-12	(a) Schematic of oblique incidence evaporation for the as-deposited layer with randomly arranged atoms. θ is the angle between the evaporated vapor and the substrate surface.	20
Figure 1-13	(a) Schematic of magnetic annealing and (b) alignment of magnetic moments towards the applied magnetic field, H	21
Figure 1-14	Experimental setup showing the direction of the force and the magnetic field and (b) normal view of a film. <i>Reprinted from [6] with permission. © 2012 American Institute of Physics.</i>	21
Figure 1-15	Schematic representation of the density of states of 3-d transition metal. Note the density of d states with spin down at the Fermi energy, E_F	24
Figure 1-16	Schematic illustration of two-current model for 3-d transition ferromagnetic metals.	25
Figure 1-17	Schematic illustration of Mott's two-current model applied to multilayers when the magnetic moments of the adjacent ferromagnetic layers are (a) antiparallel ($H = 0$) and (b) parallel ($H \neq 0$). The black arrows represent the current channels.	26
Figure 1-18	Two dimensional view ($x - y$ plane) of a cubic lattice structure.	27
Figure 1-19	(a) Single crystal of hcp-Co and (b) initial magnetization curves for applied field along the c - and a - axes. θ is the angle between the magnetization and the c - axis.	28

Figure 1-20	Magnetization rotation model: (a) the direction of spontaneous magnetization, M_s , and the easy axis ($\theta = 0$) and (b) M_s makes an angle, θ with the easy axis.	29
Figure 1-21	Magnetization rotation model for small fields, H	30
Figure 1-22	Various film preparation processes.	34
Figure 1-23	Bragg's diffraction.	35
Figure 1-24	Various magnetoresistance measurement configurations.	36
Figure 1-25	(a) Schematic of a four-point probe method and (b) a resistor circuit. The current is fed through terminals 1 and 4 and the voltage is measured between terminals 2 and 3.	37
Figure 2-1	$M - H$ loops for the randomly oriented (isotropic) films. The notations // and \perp indicate the direction of the magnetic field along the parallel and perpendicular to the easy axis, respectively.	41
Figure 2-2	$M - H$ loops for the uniaxially oriented (anisotropic) multilayer films. The notations // and \perp indicate the direction of the magnetic field along the parallel and perpendicular to the easy axis, respectively.	42
Figure 2-3	XRD patterns of [Co 1.0 nm/Au 2.0 nm] ₂₀ multilayer.	43
Figure 2-4	Field dependence of the MR ratio for the randomly oriented (isotropic) multilayer films. The notations // and \perp denote the direction of the applied field parallel and perpendicular to the current, respectively.	44
Figure 2-5	Field dependence of the MR ratio for the uniaxially oriented (anisotropic) multilayers. The notations // and \perp denote the direction of the applied field parallel and perpendicular to the easy axis current, respectively.	45
Figure 2-6	Field dependence of the MR ratio for the uniaxially oriented multilayers. The notations // and \perp denote the direction of the applied field parallel and perpendicular to the hard axis current, respectively.	46
Figure 2-7	The MR ratio of the randomly oriented (isotropic) and uniaxially oriented (anisotropic) [Co 1.0 nm/Au (tAu) nm] ₂₀ multilayers at various Au layer thicknesses. Each point in the graph represents the average of two data.	47
Figure 2-8	The MR ratio versus Au layer thickness at various Co layer thicknesses.	48
Figure 2-9	The MR ratio and Ku versus annealing temperature: open circles (o): $H // I$ and closed circles: (•) $H \perp I$ for uniaxially oriented multilayers, and cross (x): $H // I$ or $H \perp I$ for randomly oriented multilayers.	49
Figure 3-1	Typical pulsed-current waveform.	52
Figure 3-2	(a) Diagram showing the principle of pulsed-current deposition, (b) deposition time versus potential corresponding to the pulsed-current, and (c) film structures corresponding to (b).	52
Figure 3-3	Schematic of pulsed-current deposition [122].	54

Figure 3-4	$M - H$ hysteresis loops for the randomly oriented, i.e., as-deposited ($\epsilon = 0$) [Co 1.5 nm /Ag 1.5 nm] ₂₀ multilayer.....	55
Figure 3-5	$M - H$ hysteresis loops for the uniaxially oriented, i.e., strain-induced ($\epsilon = 1.5\%$) [Co 1.5 nm /Ag 1.5 nm] ₂₀ multilayer.	56
Figure 3-6	Field dependence of the MR ratio and the corresponding magnetization curve for the randomly oriented ($\epsilon = 0\%$) [Co 1.5 nm /Ag 1.5 nm] ₂₀ multilayer.	57
Figure 3-7	Field dependence of the MR ratio and the corresponding magnetization curve for the uniaxially oriented ($\epsilon = 1.5\%$) [Co 1.5 nm /Ag 1.5 nm] ₂₀ multilayer, when the magnetic field was applied parallel to the easy axis.	58
Figure 3-8	Field dependence of the MR ratio and the corresponding magnetization curve for the uniaxially oriented ($\epsilon = 1.5\%$) [Co 1.5 nm /Ag 1.5 nm] ₂₀ multilayer, when the magnetic field was applied perpendicular to the easy axis.	59
Figure 3-9	Co layer thickness dependence of the MR ratio for Ag layer thickness of 1.5 nm: (a) randomly oriented [Co (tCo) nm/Ag 1.5 nm] _N film and (b) and (c) uniaxially oriented [Co (tCo) nm/Ag 1.5 nm] _N films: field // hard axis and field // easy axis, respectively, at 21 kOe.....	60
Figure 3-10	Relationship between the anisotropy constant, Ku , and the Co layer thickness, tCo , for the [Co 1.5 nm /Ag 1.5 nm] _N multilayer.	61
Figure 3-11	The MR ratio versus anisotropy constant, Ku , for the [Co 1.5 nm/Ag 1.5 nm] _N multilayer for (a) magnetic field, H // hard axis and (b) magnetic field, H // easy axis.	62
Figure 3-12	(a) Co/Ag multilayer showing the direction of strain, the direction of magnetic field, and the direction of induced easy axis due to strain, (b) schematic of a torque meter, and (c) torque curve.	63
Figure 3-13	Field dependence of the MR ratio for [Co 3.0 nm /Ag 1.5 nm] ₂₀ multilayer at $H = \pm 21$ kOe: open triangle, Δ , is for the isotropic multilayers, and open circles, \circ , H // easy axis and closed squares, \blacksquare , H // hard axis are for the anisotropic multilayers. Solid lines are guides for the eyes.	64
Figure 3-14	The MR ratio versus degree of anisotropy, β , for the anisotropic [Co (tCo) nm/Ag 1.5 nm] _N multilayers: (a) H // easy axis and (b) H // hard axis, measured at 21 kOe.	65
Figure 3-15	(a) Isotropic multilayer and two different measurement configurations and (b) (i) R vs. tCo , (ii) ΔR vs. tCo , and (iii) MR ratio vs. tCo , for the [Co (tCo) nm/Ag 1.5 nm] _N multilayer.	66
Figure 3-16	(a) Anisotropic multilayer showing various measurement configurations, circles (\bullet , \circ) indicate H // easy axis and squares (\blacksquare , \square) indicate H // hard axis, with the direction of the current in parallel and perpendicular to the applied field, b(i) R vs. tCo , (ii) ΔR vs. tCo , and (iii) MR vs. tCo for the [Co (tCo) nm/Ag 1.5 nm] _N multilayer.	67

Figure 3-17	Field dependence of magnetizations for various values of ε (0 to 1.5 %). The magnetic field was applied along the parallel and perpendicular to the easy axis.	68
Figure 3-18	Relationship between the remnant magnetization ratio (M_r/M_s) and strain, ε . ε is increased from 0 to 1.5 %, superimposed with a 90 % best linear fit.	69
Figure 4-1	Schematic of stress, σ , versus strain, ε . The slope of the tangent gives rise to Young's modulus, E , and, σ_{YS} , is the yield strength. Elastic and plastic regions and allowable strain limits are labeled in the diagram. <i>Reprinted from [6] with permission. © 2012 American Institute of Physics.</i>	73
Figure 4-2	(a) Magnetization ($M - H$) curves and (b) field dependence of the MR ratio at low fields. Magnetization curves were measured along the field parallel and the perpendicular to the direction of the easy axis at room temperature (R.T.).	74
Figure 4-3	Co layer thickness dependence of the MR ratio for [Co (tCo) nm/Cu 1.5 nm] _N : (a) randomly oriented film, (b) and (c) uniaxially oriented films: field // hard axis and field // easy axis, respectively.....	75
Figure 4-4	Experimental room temperature magnetization for the [Co (tCo) nm /Cu 1.5 nm] _N multilayers for various Co layer thicknesses at $\varepsilon = 1.5$ %.	76
Figure 4-5	Remnant magnetization ratio, β , versus Co layer thickness.....	77
Figure 4-6	The MR ratio versus the degree of anisotropy, β , a ratio of $M_r//$ (magnetization measured when the applied magnetic field was perpendicular to strain, i.e., parallel to the easy axis) and $M_r\perp$ (magnetization measured when the applied field was parallel to strain, i.e., perpendicular to the easy axis). The inset shows % ΔMR versus β , being superimposed with a 95 % best linear fit.	78
Figure 4-7	Relationship between the magnetic anisotropy constant, Ku , and the induced strain, ε . The inset in it shows magnetization curves at various strain values ($\varepsilon = 0$ to 1.5 %).	79
Figure 4-8	Correlation between the MR ratio and strain, ε , (a) closed circles (●): $H \perp Ie. a.$ and (b) open circles (○): $H // Ie. a.$. Directions of applied magnetic fields, current, and strain are indicated with the corresponding arrows.	80
Figure 5-1	Co at % in the alloy versus Co at % in the electrolyte as the Co at % in the electrolyte is changed from 10 to 98 at %. Closed triangles (▲): $J = 1$ mA/cm ² and closed circles (●): $J = 5$ mA/cm ²	84
Figure 5-2	The MR ratio versus Co (at %) in the alloy. Open circles (○) and open squares (□) represent MR values at the current densities of 1 and 5 mA/cm ² , respectively.	85
Figure 5-3	Composition dependence of saturation magnetization for the as-deposited and annealed Co-Au alloys. Open squares (□) and open circles (○) represent magnetization for the as-deposited alloy at the current density of 1 and 5 mA/cm ² , respectively. Closed squares (■) and closed circles (●) represent magnetization for the annealed alloy.....	86

Figure 5-4	X-ray diffraction patterns for the as-deposited $\text{Co}_{35}\text{Au}_{65}$ alloys at various current densities (1, 3, and 5 mA/cm^2) as the diffraction angle, 2θ is changed from 36 to 46°	87
Figure 5-5	Saturation magnetization for the as-deposited $\text{Co}_{35}\text{Au}_{65}$ alloys deposited at 3 mA/cm^2 : closed circles (●) indicate field-cooled (298 K to 5 K at 50 Oe) and open circles (o) indicate zero-field-cooled (5 K to 298 K). ZFC and FC in the diagram represent zero-field-cooled and field-cooled, respectively.	88
Figure 5-6	Saturation magnetization for the as-deposited $\text{Co}_{35}\text{Au}_{65}$ alloy deposited at 5 mA/cm^2 : closed circles (●) field-cooled (298 K to 5 K at 50 Oe) and open circles (o) zero-field-cooled (5 K to 298 K). ZFC and FC in the diagram represent zero-field-cooled and field-cooled, respectively.	89
Figure 5-7	Saturation magnetization for the annealed $\text{Co}_{35}\text{Au}_{65}$ alloys deposited at 5 mA/cm^2 and annealed: closed circles (●) indicate field-cooled (298 K to 5 K at 50 Oe) and open circles (o) indicate zero-field-cooled (5 K to 298 K). ZFC and FC in the diagram represent zero-field-cooled and field-cooled, respectively.	90
Figure 6-1	(a) (i) Deposition time versus potential (corresponding to the pulsed-current) and (ii) cross-section of the nanostructure with the total thickness, d , and (b) shows the same but with a higher stacking number, n	93
Figure 6-2	Magnetization, M_s , versus Co (at %) in the film as the stacking number, n , is increased from 30 to 300.....	94
Figure 6-3	(a) Magnetization, M_s , versus stacking number, n : open triangles (Δ): lattice constant and open circles (o): saturation magnetization.....	95

List of Symbols

a	Lattice Constant
Ag	Silver
AgI	Silver Iodide
Au	Gold
B	Boron
Cd	Cadmium
Cl	Chlorine
Co	Cobalt
Cr	Chromium
Cu	Copper
e	Electronic Charge
E	Electric Field
F	Force
Fe	Iron
Ga	Gallium
g	Gram
H	Magnetic Field
Hz	Hertz
I	Current
K_A	Anisotropy Constant
K	Kelvin
k_B	Boltzmann's Constant
KI	Potassium Iodide
kOe	Killo Orested
L	Torque
M	Magnetization
m	Magnetic Moment
mA	Milliampère
Mg	Magnesium
N	Number of Free Electrons
Na	Sodium
Ni	Nickel

<i>Oe</i>	Orested
<i>Pb</i>	Lead
<i>Pd</i>	Palladium
<i>Pt</i>	Platinum
<i>r</i>	Radial Distant
<i>R</i>	Resistance
<i>T_B</i>	Blocking Temperature
<i>Sn</i>	Tin
<i>Ti</i>	Titanium
<i>V</i>	Volt
<i>Zn</i>	Zinc

List of Abbreviations

AMR	Anisotropic Magnetoresistance
ASTM	American Society for Testing and Materials
CIP	Current-in-the-Plane
CMOS	Complementary-Metal-Oxide-Semiconductor
CPP	Current-Perpendicular-to-the-Plane
DC	Direct Current
emu	Electromagnetic Unit
FC	Field-cooled
fcc	Face-centred Cube
FM	Ferromagnetic
GMR	Giant Magnetoresistance
MBE	Molecular Beam Epitaxy
MR	Magnetoresistance
MRAM	Magnetic Random Access Memory
NM	Nonmagnetic
OMR	Ordinary Magnetoresistance
PLD	Pulsed Laser Deposition
rf-SQUID	Radio Frequency-Superconducting Quantum Interface Device
RKKY	Ruderman-Kittel-Katsuya-Yoshida
VSM	Vibrating Sample Magnetometer
XRD	X-Ray Diffraction
ZFC	Zero-field-cooled

Acknowledgments

The time spent on this PhD dissertation was one of the most exciting and memorable journeys of my research career. Many people have contributed directly and indirectly to bring this thesis into the current shape. Primarily I wish to express my intense gratitude to my academic advisor Dr. Nicolas A. F. Jaeger for his valuable guidance, fruitful suggestions, and critical assessment that he provided me in bringing this thesis to its present form. Especially valuable asset was the financial support that he extended and liberty that he provided in choosing research directions. In addition, his manifold mentorship is the major factors behind my developing into an independent and poised scholar.

Thanks are due to Dr. John Madden, Dr. Edmond Cretu, Dr. Lukas Chrostowski, and Dr. William Dunford, UBC Electrical and Computer Engineering for agreeing to serve on my dissertation committee, and for their keen interest and suggestions in materializing this work. I would like to extend my gratitude to Dr. David Pulfrey, Dr. Tim Salcudean, and Dr. Robert Schober for their timely guidance, and Dr. Konrad Walus, Dr. Alireza Nojeh, and Dr. Shuo Tang for their constructive remarks during my initial stage of PhD life. I wish to thank posthumously Yuiji Ueda for his contribution to my research¹. I wish to greatly acknowledge the contribution of Dr. Karen Kavanagh, Simon Fraser University, for making many fruitful remarks and suggestions during manuscript preparations.

I greatly appreciate the amiable assistance received from Kirsten Frankish, Daniel Fritz, and Julie Hodge (UBC Faculty of Graduate Studies), Cathleen Holtvogt, Sonia Dhillon, Kristie Henriksen, and Andrey Vlassov (UBC Department of Electrical and Computer Engineering), Anne Coates (UBC Department of Economics), and Doris Metcalf (UBC Faculty of Medicine) for their support in various forms. I am thankful to all of the members in electrooptics laboratory and members of Dr. Lukas Chrostowski's laboratory for the collaboration that they extended in carrying out experiment.

I would like to thank all my collaborators from around the globe for their contributions to this work. I also would like to thank domestic and international students and their families at the UBC Acadia Park Housing Complex, who enriched my graduate life in many ways.

My late parents — Durga-Datta and Manodhara Rizal — sacrificed their valuable time for the sake of my personal development. Similarly, I owe my deepest thanks to my wife Sushma and my children Eliza, Dave, and Edmond who always stood by me throughout my research and pulled me through against impossible odds at times. My parents-in-laws, brothers, sisters, brothers-in-laws, sisters-in-laws, nephews, and nieces have always been supportive during the course of my research.

¹ Two papers included in this thesis contain material to which Yuiji Ueda contributed before his untimely passing in 2007.

Finally, I would like to thank the Natural Science and Engineering Research Council (NSERC), UBC Faculty of Graduate Studies, and UBC Faculty of Applied Science for providing financial support in the form of awards, bursary, and scholarships.

Dedication

To my parents who always stood behind me and knew I would succeed.

To my wife who always stood behind me but always underestimated me.

To my children who always overestimated me.

To my co-workers who had their own interpretations.

Chapter 1: Introduction

Artificially synthesized ferromagnetic hybrid nanostructures such as, multilayers, alloys, and nanoparticles are central to modern research projects due to the interesting electronic, magnetic, and spin related properties that these nanostructures demonstrate, have opened up numerous applications in electronics, automotive, and biomedical industries [1], [2]. Besides these areas, the application of electrochemical and oblique incidence vacuum evaporation principles used in the production of these nanoengineering materials is undergoing paradigm shift. Combining ferromagnetic, nonmagnetic, and organic materials into new nanoelectronic materials is a dynamic area of research. The objective of this thesis is to develop Co-based hybrid nanostructures, such as, magnetic multilayers [3]–[6], granular alloys [7], and biocompatible nanoparticles [8], [2], [9] with, the promise to yield innovative device materials with increased functionality, that will impact future magnetronic and biomedical technologies.

Magnetic multilayers based on *3-d* transition metal Co and group IB nonmagnetic metals Cu, Ag, and Au grown at the nanometer scale have great potential to become technologies not only in spintronics (e.g., magnetic random access memory, field detectors, quantum information devices, reconfigurable logic devices, etc.) [10], automation controls (e.g., wheel speed sensors, speed and position sensors, steering wheel sensors, etc.) [11], but also in biomedical sectors (e.g., surface plasmon resonance biosensors, magnetoresistance sensors for real time detection of cancer biomarkers) [8], [2], [9], [12], [13]. This is mainly because these magnetic multilayers exhibit the giant magnetoresistance (GMR) effect, a large decrease in electrical resistance due to a small applied magnetic field, and a possibility of inducing strong magnetic anisotropy, a dependence of the internal energy on the orientation of magnetic moments, leading towards the development of highly sensitive GMR sensors. Due to the quantum mechanical effect that occurs in these nanostructures and the sensitivity to small magnetic field as compared to the anisotropic magnetoresistance (AMR) effect, a decrease or increase in electrical resistance depending on the direction of the applied field and the current, reported so far [14], [15], they enable GMR sensors to be extremely small size. Both the high sensitivity and the miniaturized size of the GMR sensors will be necessary requirements for the next-generation magnetronic industry, which demands GMR sensors with the room temperature MR of 10 % or above [12], which is over four times larger than the AMR effect [14].

While the GMR and magnetic properties exhibited by nanomagnetic multilayers continue to attract great attention in terms of fundamental research and technological applications [16], [17], these multilayers seldom exhibit any magnetic anisotropy. Although several reviews on inducing magnetic anisotropy in ferromagnetic multilayers via external means, such as the application of magnetic field [18] and magnetic annealing [19], are available in the literature [20], [21], only a few have addressed magnetic anisotropy using strain [22]. The questions of how and to what extent strain has an effect on the physical properties of these multilayers have yet to be answered.

In addition, GMR and magnetic anisotropy properties of the magnetic multilayers have been strongly influenced by the ferromagnetic and nonmagnetic layer thicknesses and the interfacial states between the layers [23], [24]. The quality of the interfacial states between the ferromagnetic and the nonmagnetic layers affecting magnetoresistance (MR) and magnetic anisotropy is dependent upon the types of growth methods employed [25]. The primary physical methods involved in the growth of these multilayers are normal evaporation [26], [27] and oblique incidence evaporation [28], both at high vacuum, whereas chemical methods involve potentiostatic and galvanostatic deposition in aqueous electrolytes [29], [30]. However, it is still uncertain as to what extent the growth methods has an effect on the physical characteristics of these multilayers. In this thesis, magnetic multilayers and alloys have been produced both using pulsed-current deposition and e-beam evaporation growth methods, and their effect on the GMR and magnetic anisotropy properties have been investigated.

Co based magnetic alloys prepared via pulsed-current deposition in aqueous electrolytes have been found to possess very interesting microstructure, magnetization, and MR effects [31]. Several researchers [31], [32] have reported room temperature MR of 0.5 % for the as-deposited Co-Au alloys and of up to 1.5 % when annealed at 573 K. Previous studies [33] have shown GMR values of up to 4.0 % for the as-deposited Co-Au alloys prepared using pulsed-current deposition in a cyanide solution and demonstrated how closely GMR and saturation magnetization are correlated with the film thickness and composition [34]. However, it is not yet fully clear to what extent deposition current density, annealing, and layer thickness have an effect on the grain size and on the electrical and magnetic properties of Co-Au alloys. Therefore, the study in this thesis describes the effect of current density and annealing on the composition and particle size of Co in the Au matrix for the Co-Au alloy prepared using pulsed-current deposition. A relationship between the MR ratio, saturation magnetization, and Co grain sizes in the alloys has also been investigated. Both deposition current density and annealing have been found to have appreciable effects on the GMR, saturation magnetization, and grain size of Co in the Au matrix. A low temperature measurement suggested that the larger MR ratio in the Co-Au nanocomposites correlates with the smaller Co grain size [34], [7].

Ferromagnetic nanoparticles such as FeCo possess many interesting magnetic properties. One such property consists of engineering the saturation magnetization by manipulating layer thickness, composition, and lattice spacing [35], [36]. The same cannot be achieved for 3-*d* transition metals Fe and Co and their bulk alloys [37]. So far, maximum reported saturation magnetization in FeCo is 212 emu/g [38], and 205 emu/g [39] at room

temperature. This limits its use in magnetic biosensing. In addition, the questions as to how and in what way the internal states of these nanostructures have an effect on the saturation magnetization has not yet been fully understood. In this thesis, the saturation magnetic moment of the FeCo nanostructure is studied as the stacking number is changed. By adjusting the width and the interval time of the pulsed-current wave, FeCo nanostructures have been produced by alternately stacking Fe and FeCo in various ratios. The FeCo nanostructures produced at the atomic scale exhibited saturation magnetization values of up to 240 emu/g at room temperature, which is much larger than the magnetization values of either Fe or Co reported so far [38], [39]. The magnitude of the saturation magnetization is found to be strongly dependent on the microstructure [40], [41].

A specially designed oblique incidence arrangement has been used in this thesis to grow buffer layers and multilayers on polyimide and glass substrates at various angles of evaporation to induce magnetic anisotropy by preferential growth of crystalline Co. The oblique incidence e-beam evaporation method is very efficient because the materials are directly heated by electron bombardment and the evaporation rate can be easily controlled via electron beam intensity.

Pulsed-current deposition is another preferred method used in this thesis, in which magnetic multilayers, alloys, and nanoparticles have been grown from a single electrolyte [42]–[46]. This method has many merits over high vacuum and elevated temperature deposition methods. For example, pulsed-current deposition is a room temperature technology, which offers precision in growth on an atomic scale. The pulsed-current plating set-up is simple. It is also a cost effective deposition method as compared to high vacuum vapor deposition methods. The electrical and magnetic properties can be easily manipulated by controlling the film composition (pulse amplitude) and thicknesses (pulse widths) on the atomic scale. In addition, it does not require extensive training to develop nanostructured films [47].

The materials produced in this thesis will enable researchers to develop these GMR sensors in an array chip to detect stray magnetic fields induced by high-magnetic moment nanoparticles that can be attached to human cells to detect early symptoms of chronic diseases. These results lay out the basis for developing magnetronic and biomagnetic technology to be used in improving the early detection and treatment of various chronic diseases.

The introduction section starts with a discussion of the films (Section 1.1) and temperature dependence of their resistivity (Section 1.2) and various MR effects (Section 1.3). It reports on various types of MR characteristics and discusses and lists experimental surveys of the GMR effect in magnetic multilayers with current-in-the-plane (CIP) and current-perpendicular-to-the-plane (CPP) geometries (Section 1.4). In addition, it reports MR characteristics and experimental surveys of the GMR effect in magnetic granular alloys (Section 1.5). Section 1.6 discusses the induced magnetic anisotropy in magnetic multilayers related to this thesis.

While ferromagnetic *3-d* transition metals exhibit the AMR effect and large magnetic anisotropies (crystalline and shape) depending on which crystalline axis the magnetic field is applied to, the magnitude is small [14]. On the other hand, ferromagnetic multilayers and alloys exhibit the GMR effect, which is much

larger than the effect exhibited by *3-d* transition metals and their alloys, but they do not exhibit large magnetic anisotropies. Although the discussion of the MR effect in *3-d* transition metals, multilayers, and alloys points to the qualities that make these nanostructures very attractive for industrial applications, it also reveals the shortcomings of the physical properties, such as the lack of strong magnetic anisotropy, low sensitivity, and small saturation magnetization in these structures. These are the issues that motivated me to conduct research presented in this thesis.

This thesis follows the manuscript-based thesis guidelines and Chapters 2 through 6 consist of manuscripts that are published or accepted for publication. The repetition of contents from chapter to chapter has been avoided. Chapters 2 through 4 of this thesis present results on Co/Au, Co/Ag, and Co/Cu multilayers. Chapter 5 presents results on Co-Au nanocomposites, and Chapter 6 presents results and discussions on high-moment FeCo nanostructures. The theory of electron transport in metals, magnetic multilayers, and alloys, starting with the electrical conductivity in *3-d* transition metals, has been addressed in Sections 1.7.1 through 1.7.4. Similarly, the theory on magnetic anisotropy in ferromagnetic nanostructures has been discussed in Section 1.7.5. Section 1.8 briefly discusses various film preparation methods and approaches taken to characterize magnetic nanostructures. The remainder of Chapter 1 discusses scope of the current research and organization of the thesis. Chapter 7 presents conclusions, focusing mainly on the contributions resulting from this research, and highlights practical implications of this research, describes some of the limitations, and suggests for future work regarding the use of ferromagnetic hybrid nanostructures in spintronic and magnetic technologies.

1.1 Films

In spin-electronics, typically the term “film” refers to thin films [48]. Magnetic multilayers and alloys are also termed as films. Figure 1-1 shows a range of films based on thicknesses. Films that have thicknesses of up to 10 nm are called ultra-thin films, that have thicknesses in the range of 10 nm to 1 μm are called thin films, films that have thicknesses greater than 1 μm, and up to few tens micrometers are termed as thick films. Due to the quantum nature of ultra-thin films, they exhibit unique properties that cannot otherwise be observed in thick films.

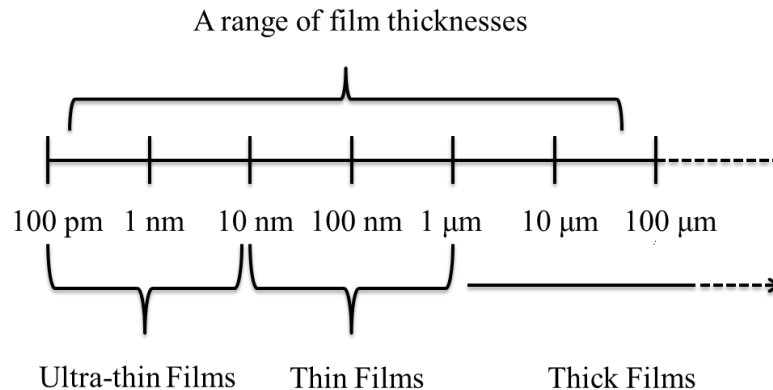


Figure 1-1 Classification of thin films based on their dimensions.

Ultra-thin films have been increasingly popular for industrial applications in material science and engineering due to the presence of interesting characteristics that they demonstrate. The physical properties of ultra-thin films are highly sensitive to microscopic phenomena.

With the current state-of-the-art technology, ultra-thin films can be grown with much more accuracy and surface flatness. With the advancement of fabrication technology, any number of atomic or molecular layers in a stack can be controlled to tailor new physical properties. In addition, new techniques can be applied to introduce impurities and alloying. The major applications of ultra-thin films are in microelectronic devices, etc., [49].

In the following sections, 1.1.1 through 1.1.4, some of the physical characteristics exhibited by ultra-thin films, relevant to this thesis, are briefly discussed.

1.1.1 Microstructural Characteristics

The microstructural characteristics of ultra-thin films are governed by variety of sources. One of them is deposition method. The size of the deposited grains varies from several nanometers to several micrometers depending on how films are grown. Others include current density, substrate temperature, crystal structure of the substrate surface, and annealing. For example, the sizes of the grains of electrodeposited films are found to be smaller when deposited at higher current densities [7]. Similarly, grain sizes of the vacuum deposited films are found to depend on the substrate temperature at which they are grown [1]. Irrespective of growth methods, the crystalline states of the deposited films are found to be strongly influenced by the crystal structure of the substrate surface on which they are grown. In addition, a post-deposition annealing treatment at higher temperature modifies the grain sizes. The overall characteristics of these particles are governed by nucleation and diffusion of atoms on the surface during deposition.

1.1.2 Electrical Characteristics

The electrical characteristics of ultra-thin films depend on the lattice defects and scattering of the conduction electrons at the interface between the layers in multilayers and the grain boundaries in the granular alloys. Hence, the electrical resistance of such films is higher than the electrical resistance of the thick films. In addition, when the mean free path of the electrons become smaller than the ferromagnetic layer thickness in the multilayer or than the diameter of the ferromagnetic grains in the alloys or nanoparticles, the probability of electron scattering at the interface increases, resulting in significantly higher electrical resistance of the films. The mechanism of electron scattering and how it relates to the electrical conductivity in *3-d* transition metals, multilayers, and alloys will be discussed in Sections 1.7.1 through 1.7.4.

1.1.3 Mechanical Characteristics

The mechanical characteristics of ultra-thin films are different from those of thick films. For example, ultra-thin films may be characterized by a strong internal stress and numerous lattice defects. Due to the high internal stress resulting from the smaller grain size, the hardness of the ultra-thin films is significantly greater than the hardness of the thick films. On the other hand, the lattice defects have the effect of increasing elastic strength.

The mechanical strength of ultra-thin films can be several hundred times larger than that of thick films. One of the challenges with ultra-thin films is that the bonding strength of the deposited film to the substrate is usually low, and, therefore, the probability that the deposited film will either peel off or develop cracks, is high.

1.1.4 Magnetic Characteristics

The magnetic properties of ultra-thin films have been found to vary significantly depending on their dimensions. In normal conditions, thin films exhibit isotropic characteristics, i.e., the magnetization is independent of the direction of the applied magnetic field. However, by controlling deposition parameters, they can be tailor made to exhibit remarkable electrical and magnetic anisotropy. For instance, by specially depositing films at an oblique angle, using magnetic annealing, and introducing strain via stress, the shape and size of the deposited grains in the film can be manipulated, and the easy axis of the magnetization (an energetically favorable direction of spontaneous magnetization) can be rotated from its parallel to perpendicular state or vice versa. This is further discussed in Sections 1.6 and 1.7.5.

In the following, Sections 1.2 through 1.5, electrical and magnetic characteristics of ultra-thin films are discussed, and start with the *3-d* transition metals.

1.2 Electrical Resistivity and Magnetism

The discovery of how electrical resistivity changes with temperature in transition metals (both ferromagnetic and non-magnetic) dates back to the mid-19th century [50]. In particular, experimental evidence was given on the high electrical resistance of Group 10 (also referred to VIII) transition metals (Ni, Pd, and Pt) and their alloys with Group 11 (also referred to IB) metals (Cu, Ag, and Au). It was demonstrated that the effective number of conduction electrons of Group 10 metals is almost the same as the effective number of conduction electrons of Group 11 metals [51]. In addition, the mean free path of the Group 10 conduction electrons is believed to be very small (~ 1 nm). That means under the influence of small lattice vibrations, these conduction electrons can make transitions to the un-occupied *d* states. The probability of having these transitions is several times greater than the probability of ordinary scattering in Group IB metals. Since the *3-d* electrons are responsible for the ferromagnetism in *3-d* transition metals, it is believed that there exists a direct relationship between the electrical resistivity and magnetism in these materials.

Figure 1-2 shows experimental measurements of the normalized electrical resistance versus normalized temperature curve for ferromagnetic Ni and nonmagnetic Pd, both being Group 10 transition elements [51]. In Figure 1-2, R_{T_c} is the electrical resistance at the Curie temperature of Ni, T_c (670 K). The electrical resistivity of ferromagnetic Ni below 670 K is always smaller than that of Pd. At 670 K, Ni experiences its order-disorder transition, whereas Pd does not. Above 670 K, the resistivity curves follow the same path for both metals. This kind of transition of electrical resistance at 670 K is believed to arise from the magnetic spin states of ferromagnetic Ni, whereas in Pd the spin states are unaffected by the variation of temperature. The mechanism of electron transport in ferromagnetic metals is further discussed in Section 1.7.3.

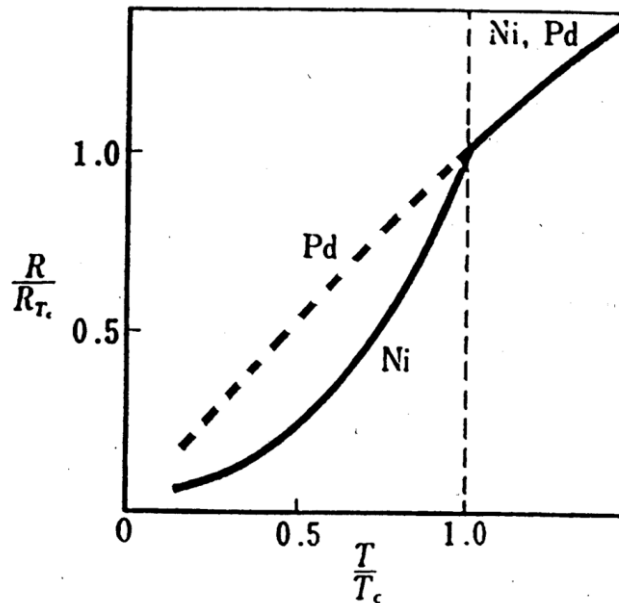


Figure 1-2 Temperature dependence of resistivity of ferromagnetic Ni and paramagnetic Pd [51].

1.3 Magnetoresistance Types

In the preceding section, the effect of temperature on the electrical resistivity of Ni and Pd is introduced. In this section, the effect of magnetic field on the electrical resistivity of the transition metals, multilayers, and alloys will be discussed. All metals and their multilayers or alloys exhibit the MR effect, a change in electrical resistance due to an external magnetic field [51]. However, the magnitude of MR can be positive (increase in resistivity) or negative (decrease in resistivity), depending on the electronic configuration of the metals or their positions in the periodic table. Moreover, the MR effect depends not only on the strength of the applied magnetic field but also on how the magnetic field is applied with respect to the current. Three distinct categories of MR effects will be reviewed here: (1) ordinary magnetoresistance, (2) anisotropic magnetoresistance, and (3) giant magnetoresistance. The materials and mechanisms for all three MR effects are markedly different.

1.3.1 Ordinary Magnetoresistance

The ordinary magnetoresistance (OMR) effect is an increase in electrical resistance (the resistivity of the material is always positive) due to an external field, and is independent of the direction of an applied field. Although the effect is small, the transverse resistivity, ρ_{\perp} , i.e., the resistivity of a material when the magnetic field is applied perpendicular to the current, is always larger than the longitudinal resistivity, ρ_{\parallel} , i.e., the resistivity of a material when the magnetic field is applied parallel to the current [52]. The OMR effect is demonstrated by non-magnetic metals, i.e., metals that do not possess spontaneous magnetization, such as Cu, Ag, Au, Mg, Zn, Cd, Ga, Ti, Sn, Pd, Pt, etc., [52], [53]. The magnitude of the OMR effect (< 1 %) makes it unsuitable to most technological applications.

1.3.2 Anisotropic Magnetoresistance

The anisotropic magnetoresistance (AMR) effect is an increase or decrease of the electrical resistance due to an external magnetic field. It depends on the direction of applied field and the angle that the spontaneous magnetization makes with the direction of the current [14]. Figure 1-3 shows (a) a normal view of a film, direction of magnetization, M , and the angle, θ , that it makes with the current, I , and (b) the resistivity, ρ , when the magnetic field is applied parallel or perpendicular to the current. As shown in Figure 1-3(b), ρ is a maximum when both the magnetic field and the current are parallel to each other and a minimum when they are perpendicular to each other.

ρ is given by [14],

$$\rho = \rho_{\perp} + \Delta\rho_{AMR} \cos^2 \theta, \quad (1.1)$$

where $\Delta\rho_{AMR} = \rho_{\parallel} - \rho_{\perp}$. The resistivity of the film is a function of the angle between the magnetization, M , and the current, I . The ratio $\frac{\rho_{\parallel} - \rho_{\perp}}{\rho_{\perp}}$ is known as the anisotropic magnetoresistance (AMR) ratio.

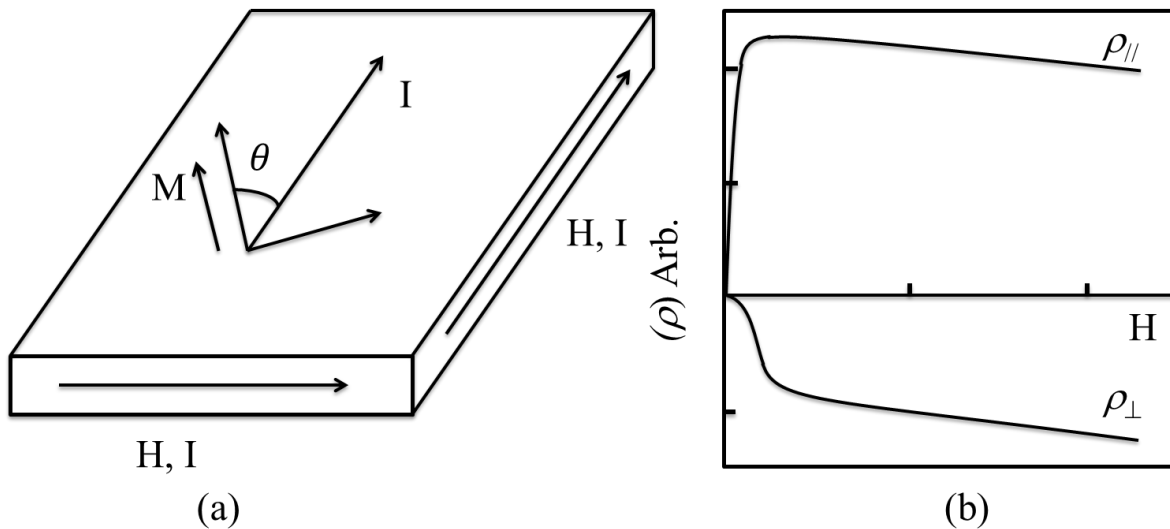


Figure 1-3 (a) Schematic of a film showing the direction of the magnetization and the current (b) resistivity versus magnetic field.

The maximum reported AMR effect in ferromagnetic metals and alloys is on the order of 2-3 %. This effect is believed to be due to the spin-orbit interaction, which affects the scattering rate of conduction electrons when the magnetic field is applied, and thus, the electrical resistivity of the 3-d transition metals. Although this magnitude is small, the AMR effect in ferromagnetic transition metals is several orders of magnitude greater than the OMR effect in metals.

1.3.3 Giant Magnetoresistance

The giant magnetoresistance (GMR) effect, as the name suggests, is a large change in electrical resistivity due to a small applied magnetic field, H . Figure 1-4 shows a schematic of the GMR effect in magnetic multilayers. At $H = 0$, it shows a high resistivity and at $H \neq 0$, it shows a low resistivity. If the electrical resistivity at the zero magnetic field and the applied magnetic field are denoted by $\rho(0)$ and $\rho(H)$, respectively, the change in the electrical resistivity per original resistivity is called the MR ratio, and is given as:

$$MR = \frac{[\rho(H) - \rho(0)]}{\rho(0)}. \quad (1.2)$$

What distinguishes the GMR effect from the OMR or AMR effects is not only that its magnitude is large but also that it is independent of the direction of the current or the applied magnetic field.

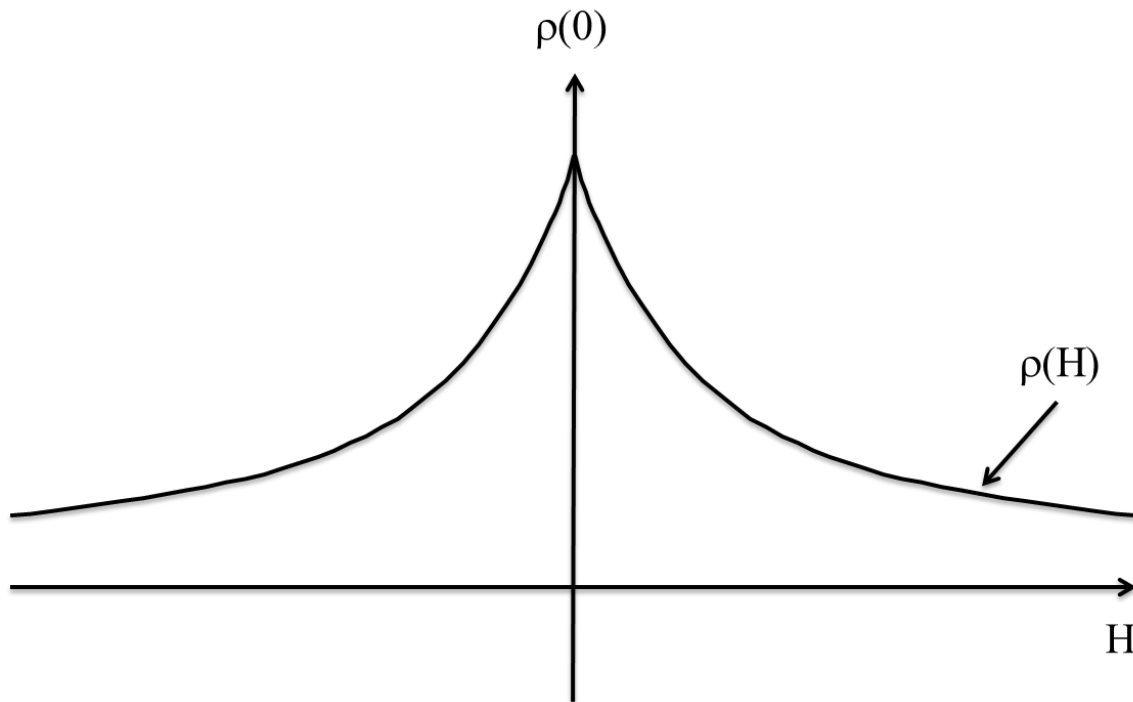


Figure 1-4 The GMR effect in ferromagnetic hybrid nanostructures.

1.3.3.1 Mechanism of the GMR Effect in Multilayers

The mechanism responsible for the GMR effect is believed to be different from the mechanism responsible for AMR or OMR effects. The GMR effect is believed to arise from the spin-dependent scattering, i.e. the interaction of the $4-s$ electrons of the nonmagnetic metals and the $3-d$ electrons of the ferromagnetic metals at the interface between the ferromagnetic and nonmagnetic layers. The probability of scattering conduction electrons depends on the relationship between the spin direction of the $4-s$ conduction electrons in the nonmagnetic layer and the direction of the magnetization of the $3-d$ electrons in the magnetic layers [54].

Figure 1-5 shows a cross-sectional view of a Co/Cu multilayer consisting of alternating layers of ferromagnetic Co and nonmagnetic Cu. The direction of the magnetic moments of 3-*d* electrons in Co (grey arrows with large arrowheads) and the 4-*s* conduction electrons in Cu (small black arrows in open circles) are labeled with the corresponding arrows. The long black arrows are connected to the conduction electron's scattering path. Under normal conditions, when no magnetic field is applied, such as the case in Figure 1-5(a), ferromagnetic moments in the adjacent Co layers are aligned antiparallel. In this situation, 4-*s* conduction electrons of Cu with spin up and parallel to the magnetic moments of 3-*d* electrons of Co pass through the first Co layer without scattering. However, when they encounter the second Co layer that has magnetic moments of 3-*d* electrons aligned antiparallel to the spin direction of the 4-*s* conduction electrons of Cu, they are scattered (it is assumed that the spin orientation of the conduction electrons is not changed even after scattering). Similarly, the 4-*s* conduction electrons with spin down and antiparallel to the magnetic moments of 3-*d* electrons undergo multiple scattering in each layer that they travel. The movement of both the spin up and spin down conduction electrons is therefore, repeatedly interrupted by scattering processes. A repeated scattering, therefore, results in high resistivity. If the magnetic field is applied to overcome the antiferromagnetic coupling (antiparallel alignment of magnetic moments) and achieve parallel alignment of magnetic moments in the adjacent ferromagnetic layers as shown in Figure 1-5 (b), although the spin down electrons of Cu are still scattered by the magnetic moments of the 3-*d* electrons of Co, the spin-dependent scattering of the spin up conduction electrons dramatically reduces. The result is the large decrease in resistivity. The decrease in resistivity is so high that it can go up to 2 orders of magnitude.

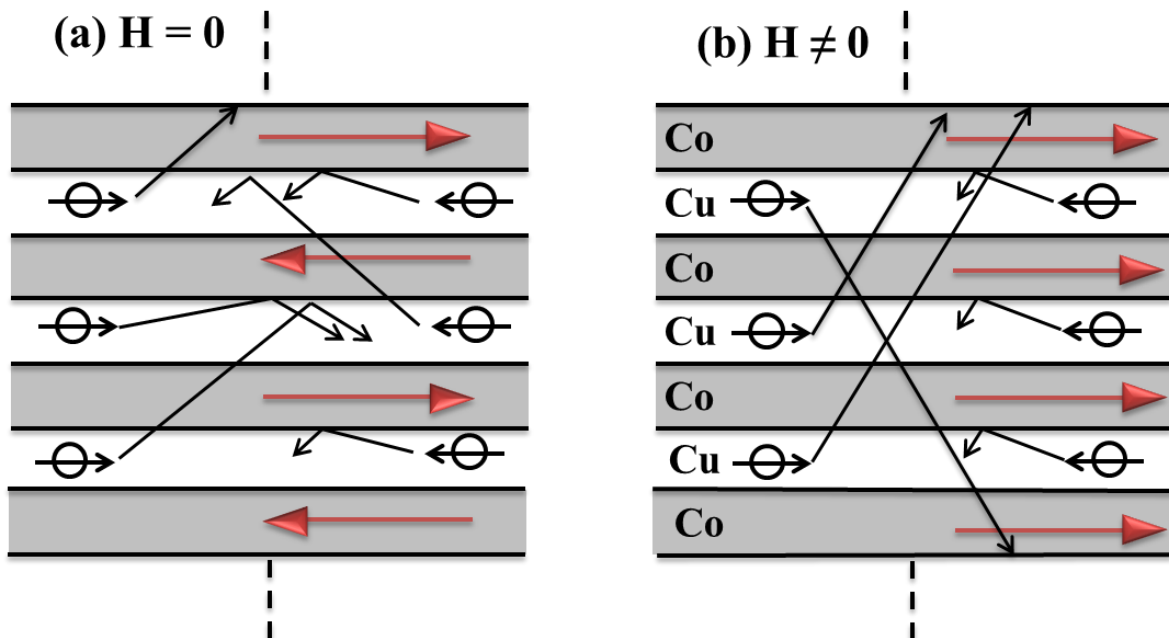


Figure 1-5 Cross-sectional view of a Co/Cu multilayer and the scattering of the 4-*s* conduction electrons by the local magnetic moments (a) at the zero magnetic field (b) at the applied magnetic field, *H*.

For practical multilayers, not only are the spin arrangements along the cross-section of the multilayer important but so are the spin arrangements along the surface of the film. Figure 1-6 shows (a) isotropic and (b) anisotropic multilayers showing magnetic moments along the surface of the ferromagnetic layers. In order to have a large GMR effect, a method is required to change the relative orientation of the magnetic moments in the adjacent magnetic layers from a random orientation, as shown in Figure 1-6 (a) to an uniaxial orientation shown in Figure 1-6 (b). In addition, to have a large GMR effect, the thickness of the non-magnetic layer must always be less than the mean free path of the electrons. Reviews of the GMR effect in ferromagnetic multilayers and granular alloys are discussed in Sections 1.4 and 1.5, respectively. The mechanism of spin-dependent resistivity in magnetic multilayers is discussed in Section 1.7.4.

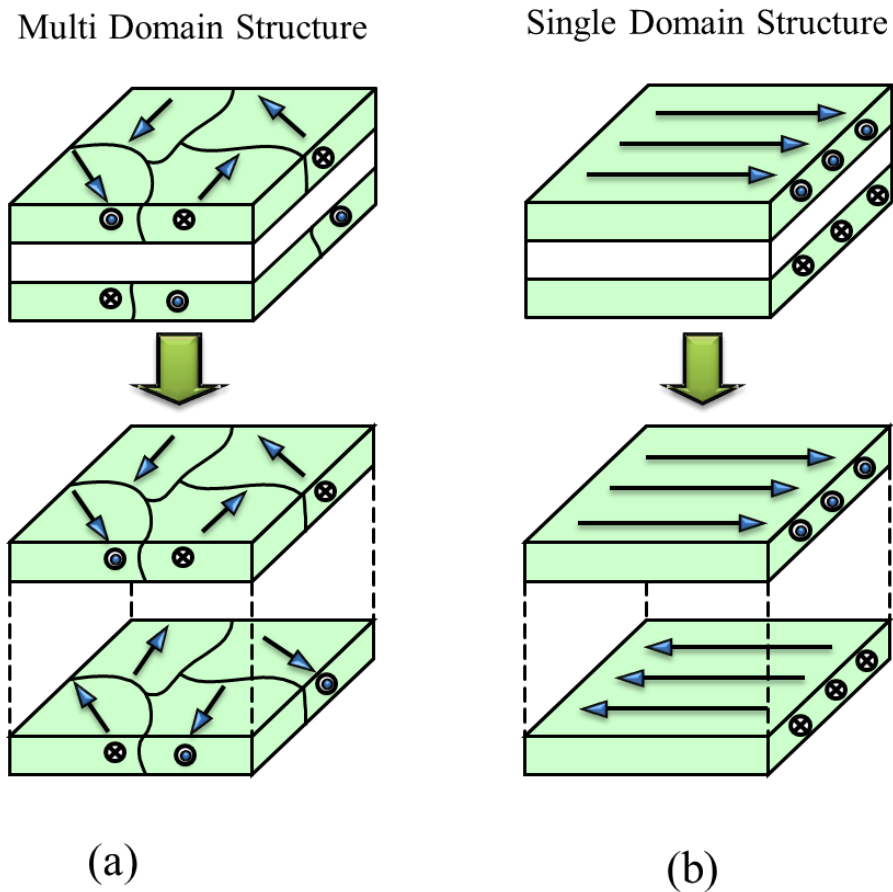


Figure 1-6 Isotropic multilayer (i.e., magnetic moments are randomly orientated) and (b) anisotropic multilayer (i.e., magnetic moments are uniaxially oriented).

Detail discussions of mechanism of transport properties in various types of multilayer structures using semi-classical transport model [25], [55], quantum model [25], Ruderman-Kittel-Katsuya-Yoshida (RKKY) coupling [56], [57], Kondo effect [58], etc., are outside the scope of current work.

1.3.3.2 Mechanism of the GMR Effect in Granular Alloys

The mechanism causing the GMR effect in granular alloys is the same as that of causing the GMR effect in multilayers (see Section 1.3.3.1). In both the cases, the GMR effect arises due to spin-dependent scattering. For magnetic multilayers, the scattering takes place at the interface of the ferromagnetic and nonmagnetic layers, see, Figure 1-5, whereas in granular alloys the same occurs at the interface of the ferromagnetic and nonmagnetic nanoparticles, see, Figure 1-7.

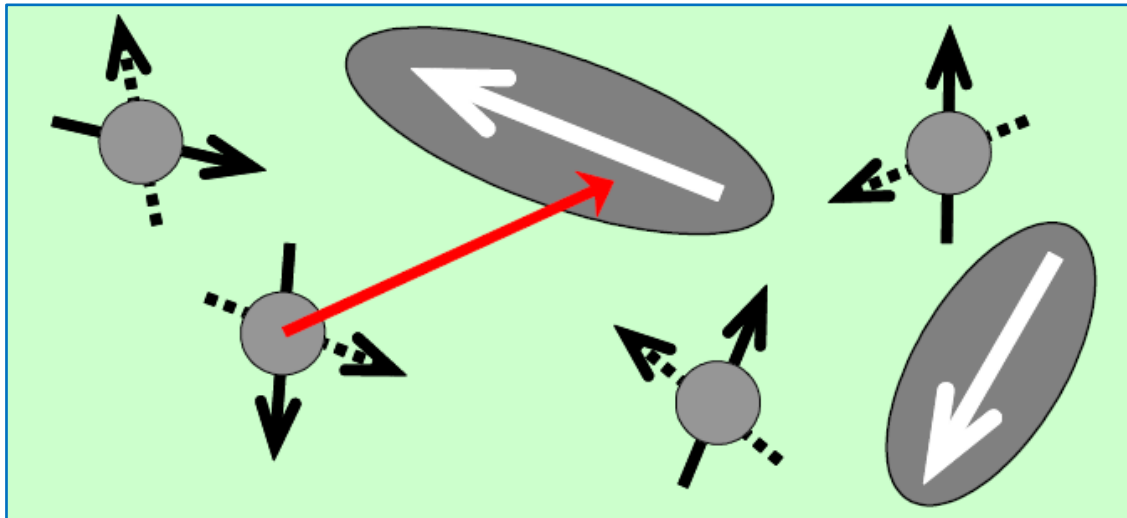


Figure 1-7 The GMR mechanism in the granular alloys consisting of superparamagnetic (circles) and ferromagnetic (ellipsoids) nanoparticles in the non-magnetic matrix [59].

Figure 1-7 shows a scenario of spin-dependent scattering between superparamagnetic (circles) and ferromagnetic nanoparticles (ellipsoids) embedded in a nonmagnetic matrix [59]. The arrows attached to each superparamagnetic nanoparticle indicate random orientation and fluctuation of superparamagnetic nanoparticles. The magnetic moments of the ferromagnetic particles have orientations determined by their shapes. The arrow connecting superparamagnetic and ferromagnetic particles shows a path of a conduction electron in the alloy. An electron polarized by the superparamagnetic nanoparticles can undergo multiple spin-dependent scattering due to the orientation of magnetic moments of the ferromagnetic particles. This results in the GMR effect.

The degree of alignment of the magnetic moments at which spin-dependent scattering takes place, determines the GMR effect. The GMR effect is, therefore, influenced by the overall magnetic states in the alloys. The volume concentration of the magnetic particles, their size distribution, and the inter-particle separations, etc., contributes to the interfacial spin-dependent scattering of the conduction electrons, and, thus, GMR effect. Further details are available in [60].

1.4 Experimental Survey of the GMR Effect in Multilayers

The GMR effect was first observed in 1988 in antiferromagnetic Fe/Cr multilayers. Since then it has been found in many different magnetic multilayers consisting of magnetic layers of a few nanometers thick separated by nonmagnetic layers. In this section, a brief survey of the main experimental results on the GMR effect in ferromagnetic multilayers is presented.

1.4.1 Current-in-the-Plane Geometry

Ferromagnetic multilayers with current-in-the-plane (CIP) geometry (i.e., current flows parallel to the plane of the multilayer) consisting of layer thicknesses in the range of few nanometers have attracted great attention because of the possibility of creating artificial materials with potentially new properties or combinations of new properties [6], [5], [61]. As discussed in Section 1.3.3, an interesting feature of the GMR effect is that there is no difference between the longitudinal (magnetic field applied parallel to the current) and transverse (magnetic field applied perpendicular to the current) MR effects. In addition, the GMR is always negative as opposed to the OMR or AMR effects.

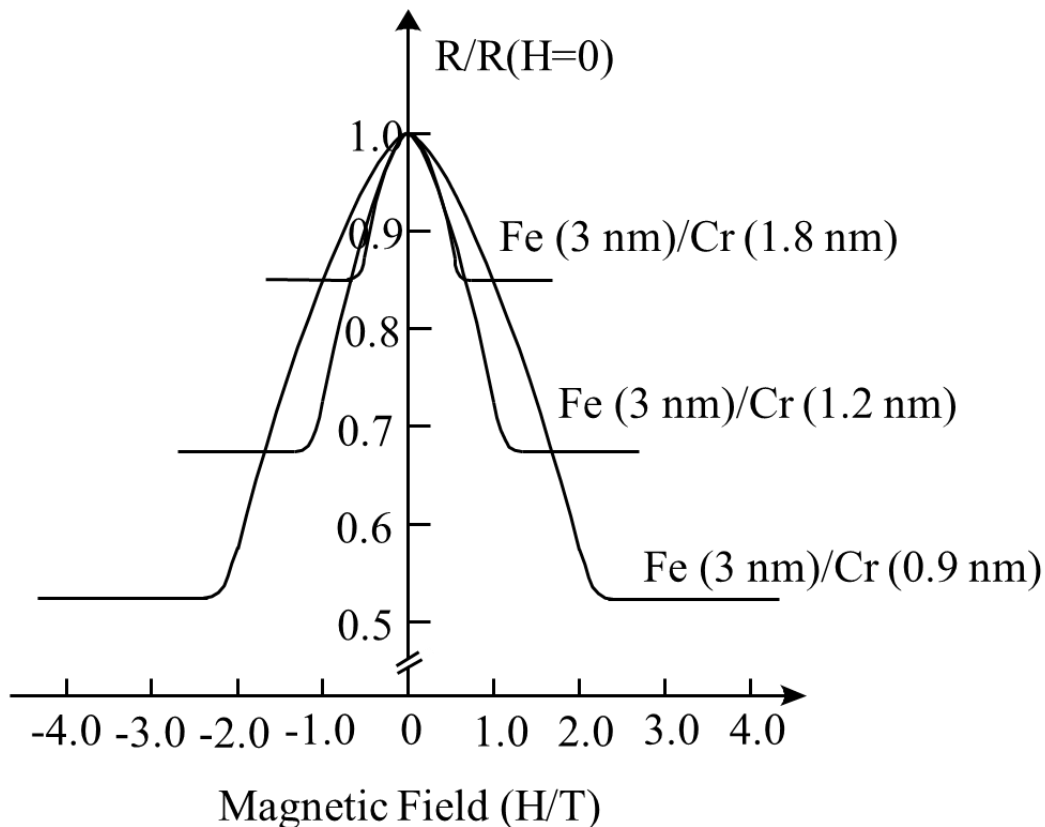


Figure 1-8 The GMR effect in Fe/Cr multilayers [62].

Figure 1-8 shows the MR effect in the experimentally demonstrated CIP Fe/Cr multilayers [62] for three different Cr layer thicknesses. As shown in Figure 1-8, the resistance decreases with the applied magnetic field.

The decrease in resistance is almost the factor of 2 when Cr layer thickness is decreased from 1.8 to 0.9 nm at 4.2 K. The magnetization measurement studies performed on these films using vibrating sample magnetometer showed interesting hysteresis characteristics, which are shown in Figure 1-9. This figure shows magnetization curves for various Fe/Cr multilayers [62]. The strength of the magnetization changes from being a purely ferromagnetic for [Fe (6.0 nm)/Cr (6.0 nm)]₅ multilayers to being poorly paramagnetic for [Fe (3.0 nm)/Cr (0.9 nm)]₆₀ multilayers, where the subscripts 5 and 60 refer to the number of Fe/Cr bilayers. The gradual tilting of hysteresis loop, as the thickness of non-magnetic Cr layer is decreased, is a signature of the change in antiferromagnetic coupling between the adjacent Fe layers.

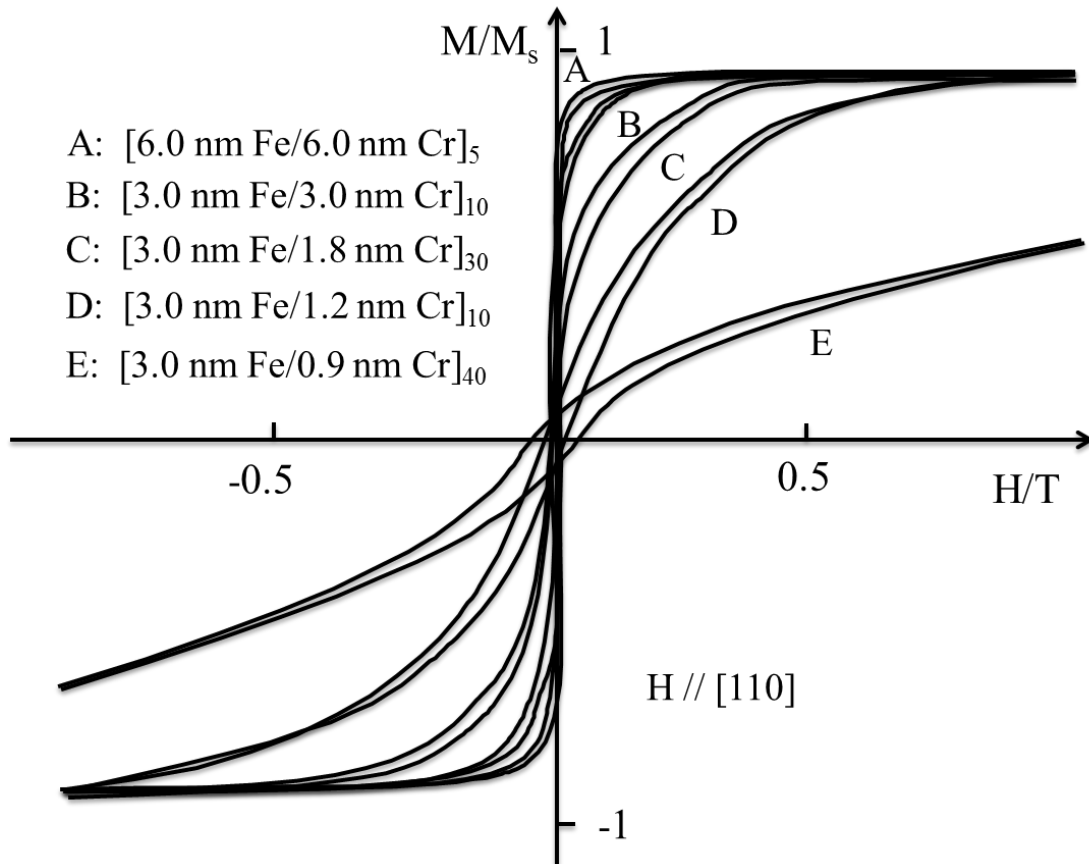


Figure 1-9 Magnetization curves of Fe/Cr multilayers [62].

Following the work of Albert's group in 1988 in the antiferromagnetically coupled Fe/Cr multilayers [61], [62] Parkin's group in 1994 [63] examined the relationship between the GMR effect and antiferromagnetic interaction of magnetic moments in the ferromagnetic Co layers by systematically changing the Cu layer thickness. The effect of the change in Cu layer thickness resulted in the oscillatory GMR effect. This is shown in Figure 1-10. The oscillatory GMR effect in ferromagnetic multilayers has been explained by RKKY coupling theory [56]. Hitherto, many other ferromagnetic multilayers in the CIP geometry have emerged with enhanced GMR effect in Co/Ru [64], Fe/Cu [65], [66], Co/Cu [66], [42], [16], Co/Au [33], Co/Ag [4], etc. In this thesis,

the GMR effect and its mechanism have been studied by systematically varying the ferromagnetic layer thicknesses in Co/Cu [67], Co/Au [3], and Co/Ag [68] multilayers.

Co-based ferromagnetic multilayers and spin-valve nanostructures dominated most of the research in the soft magnetic materials in the last decade and are still a major research focus. Table 1-1 lists the GMR effect in Fe/Cr, Co/Au, Co/Ag, and Co/Cu CIP magnetic multilayers that are relevant to the multilayers prepared in this thesis. The comparison of MR ratio is made among sputtered, MBE grown, e-beam evaporated, and pulsed-current deposited multilayers. The multilayers in this thesis have been prepared using oblique incidence evaporation and pulsed-current deposition methods at room temperature.

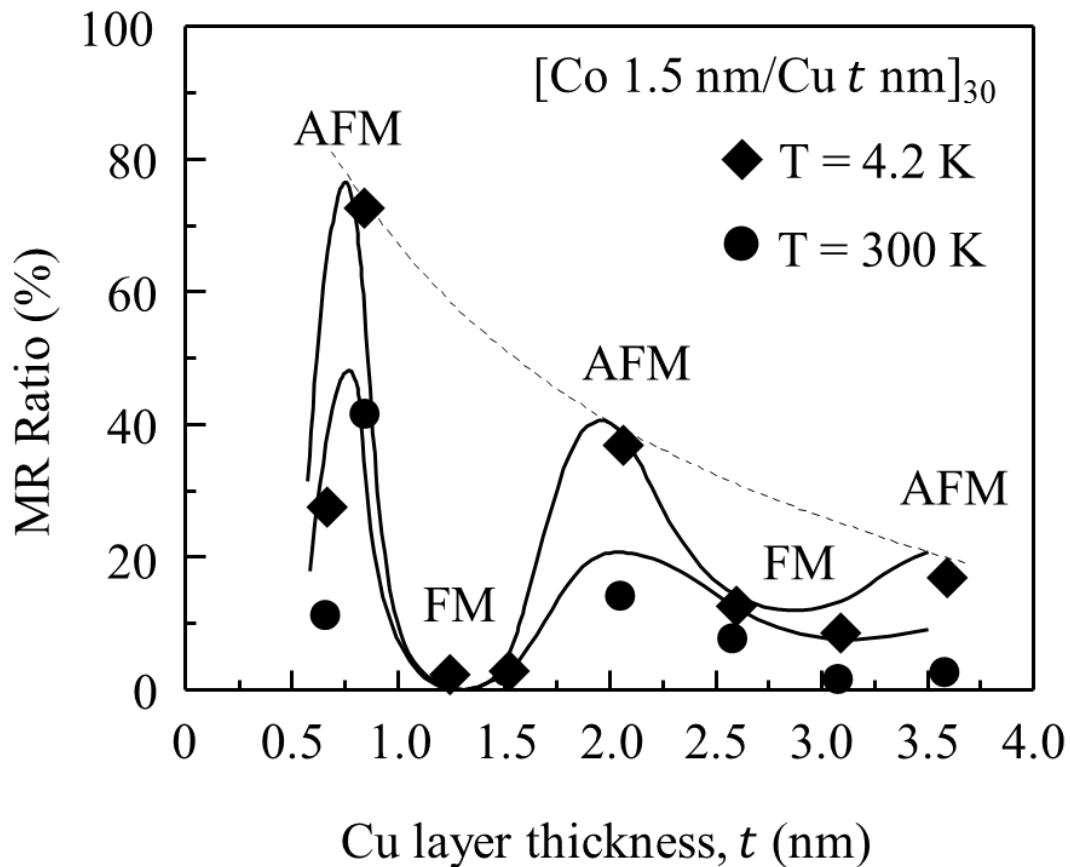


Figure 1-10 Cu layer thickness dependence of the MR ratio for Co/Cu multilayers (the subscript 30 indicates the number of bilayers in the film) [63].

GMR values for Fe/Cr multilayers are large and up to 46 % at low temperature (4 K) and at high magnetic field (50 kOe). While these results are extremely useful from the fundamental point of view studies, they are less significant from the application point of view. Similarly, the GMR ratio of Co/Cu multilayers is found to be up to 46 % for the sputtered deposited films and up to 81 % for the MBE grown films at 5 K and 50 kOe. While these numbers are large, they are not very significant when it comes to real-world applications. Similarly, the

GMR ratio of Co/Ag multilayers is found to be up to 41 % at 77 K and 20 kOe. In order for them to be useful, a large MR ratio at low magnetic field, as well as at room temperature, is highly desirable. The GMR ratios of Co/Au multilayers prepared by all four methods have been found to be low. Magnetization measurements reveal that the hysteresis curves of Co/Au multilayers saturate at low field and also the coercive force is small, which is good for the application point of view. Furthermore, experimental evidence shows that they exhibit magnetic anisotropy at low fields, if proper deposition conditions are established [3].

The overall MR ratio of oblique incidence e-beam evaporated and pulsed-current deposited multilayers is comparable to, and sometimes larger than, the MR ratio of other vapor deposited multilayers as reported in Table 1-1. The MR effects of the oblique incidence evaporated Co/Au multilayer films in this thesis are comparable to the MR effects in multilayers prepared by other vapor deposition methods. Similarly, the MR ratios of pulsed-current deposited films were comparable to, or higher than those of other vapor deposited multilayers, such as Fe/Cr (8 % at 10 kOe), Co/Ag (9.1 % at 10 kOe), Co/Cu (4.1 % at 1kOe), and Co/Au (4.1 % at 20 kOe), all at room temperature.

Table 1-1 Reports of the GMR effect in multilayers

Multilayer Films	Thickness [nm]	Preparation Methods	Temperature [K]	Magnetic Field [kOe]	MR [%]	Ref. #
Fe/Cr	3.0/1.2	DC-Sputtering	4.2	50	8	[69]
	3.0/0.9	MBE	4.2	20	46	[62]
	3.7/0.1	e-beam	77	8	37	[70]
	2.5/0.5	Pulsed-current	300	10	8	[71]
Co/Cu	1.02/2.29	Sputtering	4.2	6.7	46	[22]
	0.9./0.9	MBE	4.2	50	81	[72]
	1.0/1.5	e-beam	300	20	6.1	[42]
	1.0/1.5	Pulsed-current	300	1	4.1	[5]
Co/Ag	1.0/2.0	Sputtering	10	12	37	[73]
	0.6/2.5	MBE	77	20	41	[74]
	1.0/0.4	e-beam	300	3.5	1.5	[75]
	1.0/1.5	Pulsed-current	300	20	9.1	[4]

Multilayer Films	Thickness [nm]	Preparation Methods	Temperature [K]	Magnetic Field [kOe]	MR [%]	Ref. #
Co/Au	1.0/2.5	Sputtering	5K	3	2.1	[76]
	0.4/2.5	MBE	300	1	1.9	[77]
	1.0/2.0	e-beam	300	20	2.1	[3]
	1.0/2.0	Pulsed-current	300	20	4.1	[33]

1.4.2 Current-Perpendicular-to-the-Plane Geometry

In the previous section, we discussed the pros and cons of the GMR effect in the CIP multilayers prepared using both physical and chemical methods. In this section, a brief description is given for the GMR effect in current-perpendicular-to-the-plane (CPP) geometries.

Metallic multilayers with the CPP geometry, where the current is passed to the plane perpendicular to the surface of the multilayers, have great potential for industrial applications [25]. However, the film preparation for the CPP geometry using existing high vacuum evaporation is not as easy as the CIP geometry, discussed in Section 1.4.1. Pulsed-current deposition, on the other hand, can be used to deposit highly confined spaces or complex geometries that are not possible via sputtering or molecular beam epitaxy or e-beam evaporation methods. Figure 1-11 shows an example of magnetic nanowires [78] prepared in an insulating polymer matrix using electrochemical method. It shows Co/Cu multilayered nanowires in cylindrical nanopores of track etched polycarbonate membranes. Further details of the GMR effect in CPP geometry are available in [78].

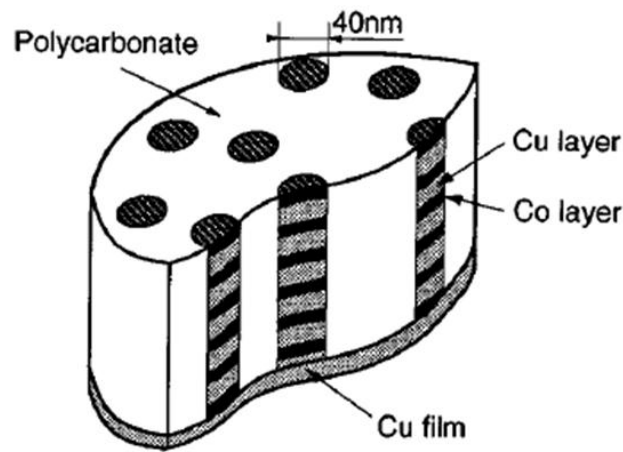


Figure 1-11 Schematic of the array of Co/Cu nanowires in an insulating polymer matrix [78].

1.5 Experimental Survey of the GMR Effect in Alloys

With the discovery of the GMR effect in magnetic multilayers, search for new materials continued and extended to artificial materials consisting of nanometer size ferromagnetic metal granules embedded in nonmagnetic media. This led to the discovery of the GMR effect in Co-Cu [79] and Co-Ag [80] granular alloys, which developed significant interest in further development of GMR granular materials. Further study in magnetic granular alloys is prompted by the simplicity in growth and use of relatively cheap and fast processes [5]. Since then, a large number of magnetic alloys have been reported, e.g., Co-Au [7], FeCo-Au [81], Co-Ag [45], Co-Cu [42], Fe-Cu [82], Fe-Ni-Cu [83], Co-Pt [84], [85]. Further works on granular alloys are available in the literature [7], [21], [18], [86].

The GMR effect and the field sensitivity (MR ratio per applied field) of granular alloys are much larger as compared to the Hall effect in ferromagnetic metals and the AMR effect in Ni-Fe alloys. Although the GMR effect in granular alloys is comparable to or larger than the GMR effect in multilayer system, the field sensitivity of granular materials is still low comparatively. However, granular alloys display a number of very interesting magnetic and transport properties such as, super-paramagnetism, magnetothermal conductivity, etc., making them attractive for both scientific investigation and application in industry.

Like Co-based ferromagnetic multilayers, Co-based magnetic granular alloys have dominated most of the research in soft magnetic materials and they are currently considered to be important. Table 1-2 lists the GMR effect in Co-Cu, Co-Ag, Co-Au, and Fe-Cu granular alloys prepared using wide range of methods, and that are relevant to the granular alloys prepared in this thesis. A random comparison of MR ratios in these alloys is made among sputtered, melt-spun, mechanical alloying, and electrochemically deposited granular alloys. Among all of the reported results, the overall MR ratio of sputtered Fe-Cu and pulsed-current deposited Co-Ag showed the largest room temperature GMR effect of up to 9.1 %.

Table 1-2 Reports of the GMR effect in alloys

Alloys	Composition [at %]	Preparation Methods	Temp. [K]	Field [kOe]	MR [%]	Ref. #
Co-Cu	Co ₁₉ Cu ₈₁	Sputtering	10	20	22	[79]
	Co ₂₀ Cu ₈₀	Sputtering	5	20	17	[87]
	Co ₁₀ Cu ₉₀	Melt-spun	300	6.5	11	[88]
	Co ₁₆ Cu ₈₄	Electrodeposition	300	11	6.2	[89]
Co-Ag	Co ₇₀ Ag ₃₀	Pulsed-current	300	10	9.1	[45]

Alloys	Composition [at %]	Preparation Methods	Temp. [K]	Field [kOe]	MR [%]	Ref. #
	Co ₃₅ Au ₆₅	Pulsed-current	300	1	4.6	[7]
Co-Au	Co ₁₅ Au ₈₅	Arc Melting	5	20	28	[90]
Fe-Cu	Fe ₃₀ Cu ₇₀	Sputtering	5	20	9.0	[91]
	Fe ₇₀ Cu ₃₀	Mechanical Alloying	300	4	1.5	[92]

Based on the results listed in Table 1-2, the pulsed-current deposition method seems to be one of the best methods when it comes to growing magnetic alloys and nanoparticles. In addition, a literature search revealed that composition modulated alloys prepared by the pulsed-current deposition method show GMR values that were comparable to the GMR values reported for multilayers and granular alloys [93]. An up-to-date and extensive literature review is available in [33] and [59]².

1.6 Induced Magnetic Anisotropy in Multilayers

Magnetic anisotropy is a very important material characteristic, in which the internal energy of ferromagnetic metals, multilayers and alloys, and nanoparticles is dependent on the direction of the spontaneous magnetization [14]. In magnetic hybrid nanostructures it is classified into three categories: (1) crystalline anisotropy (due to the crystalline structure), (2) shape anisotropy (due to the size and shape of the film), and (3) induced uniaxial anisotropy (e.g., stress/strain, high magnetic fields, etc.). Crystalline anisotropy is an intrinsic characteristic, which does not depend on the shape or size of the materials. One such metal that shows crystalline magnetic anisotropy is hcp-Co (see Figure 1-19). Shape anisotropy arises from the dipole-dipole interaction, and as the name suggests, it depends on the shape of the film. For ultra-thin films, shape anisotropy usually favors in-plane anisotropy [94], [95].

Many magnetic multilayers and granular alloys developed so far, are isotropic in nature, i.e., they do not naturally exhibit any permanent magnetic anisotropy properties. However, magnetic anisotropy can be induced via external means, such as strain and magnetic annealing. Experimental evidence has shown that obliquely deposited materials also exhibit magnetic anisotropy [96]. Induced uniaxial anisotropy in ultra-thin films arises from dipole-dipole interaction, and a good thing about it is that the effect does not go away even if the forces are removed. The following section briefly describes various contributions to magnetic anisotropy in ferromagnetic nanostructures relevant to this thesis.

² These papers include some of the author's earlier work, not included in this thesis.

1.6.1 Artificial Generation of Magnetic Anisotropy

Magnetic anisotropy in ferromagnetic hybrid structures can be induced artificially in many ways [22], [4], [97]. In this section, experimental approaches taken to generate magnetic anisotropy artificially in magnetic nanostructures, again relevant to this thesis is briefly covered.

1.6.1.1 Oblique Incidence Evaporation

Oblique incidence evaporation is one of the preferred methods for inducing magnetic anisotropy in magnetic thin films [3], [28], [98]. In this method, films are deposited on the surface of the substrate by changing the deposition angle. Figure 1-12 shows a schematic of oblique incidence evaporation and corresponding atomic positions on the surface of the substrate. The easy axis of magnetization is found to align along the perpendicular to the plane of oblique incidence of evaporation.

The mechanism behind magnetic anisotropy in this process can be explained as [94]:

- The deposited particles form a chain of crystallites, leaving behind some vacant sites (this is also known as the shadowing effect).
- The area that is left behind with vacant sites leads to an array of fine crystals and a chain of the crystals extending in a direction perpendicular to the direction of incidence.
- The easy axis of magnetization lies along the direction of these chains, which is perpendicular to the plane of incidence of evaporation.

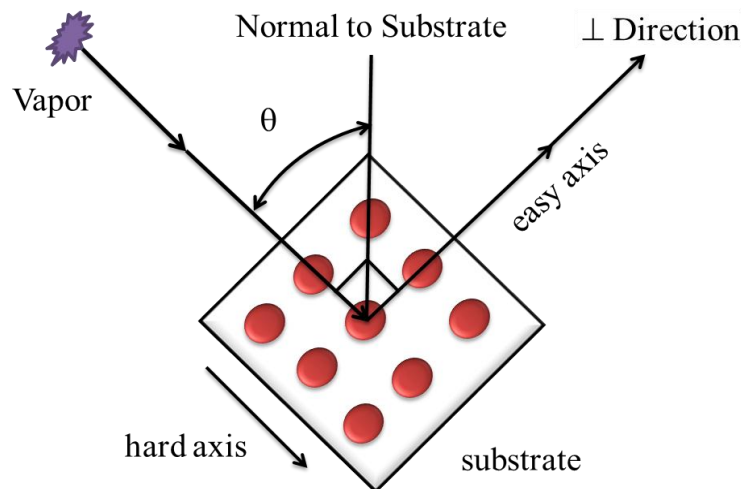


Figure 1-12 (a) Schematic of oblique incidence evaporation for the as-deposited layer with randomly arranged atoms. θ is the angle between the evaporated vapor and the substrate surface.

1.6.1.2 Magnetic Annealing

Magnetic annealing is a thermal process in which a film is heated and cooled down in the magnetic field [3], [19], [99]. This causes magnetic moments to align along the direction of the applied field.

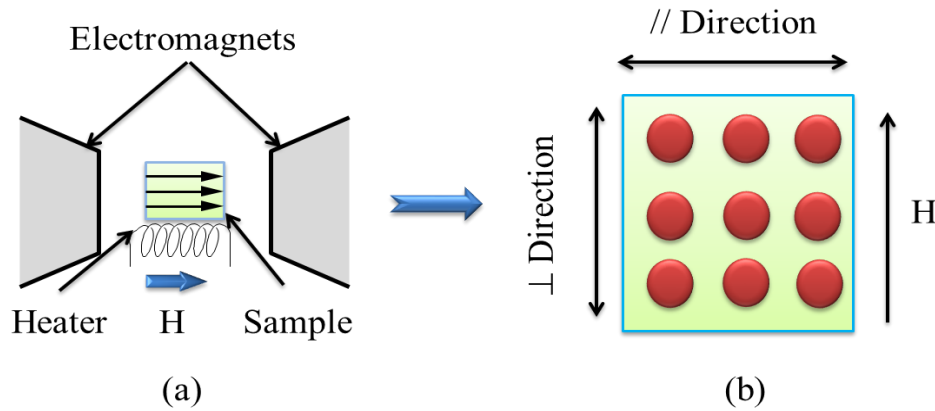


Figure 1-13 (a) Schematic of magnetic annealing and (b) alignment of magnetic moments towards the applied magnetic field, H .

Figure 1-13 shows (a) a schematic of magnetic annealing (i.e., a film is placed between two electromagnets and heated at a pressure below 10^{-6} Torr) and (b) the alignments of atoms (magnetic moments) along the direction of the applied field. The magnetic field must be large enough to saturate the film if the resulting anisotropy to be developed to its maximum extent [100]. Multilayers produced in this thesis were able to develop maximum anisotropy at the magnetic field of 3 kOe.

1.6.1.3 Application of Strain

This section briefly describes how uniaxial magnetic anisotropy is induced via strain. Figure 1-14 (a) shows the direction of the applied force and the magnetic field and (b) correspondingly induced strain in the films. The easy axis of magnetization is along the field perpendicular to the direction of strain.

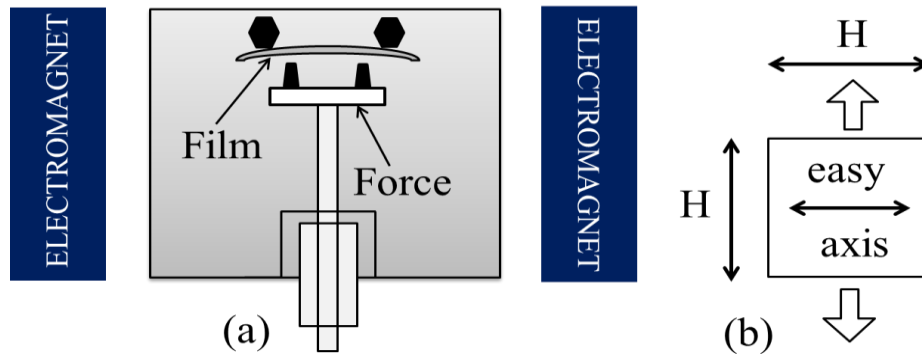


Figure 1-14 Experimental setup showing the direction of the force and the magnetic field and (b) normal view of a film. Reprinted from [6] with permission. © 2012 American Institute of Physics.

Theoretical aspects of magnetic anisotropy in ferromagnetic materials relevant to this thesis are covered in Section 1.7.5 using the spin-pair model. Further details of the theory have been described elsewhere [101], [102].

1.7 Electron Transport and Magnetic Anisotropy in 3-d Metals and Multilayers

In Sections 1.1 through 1.6, we introduced various MR effects in ferromagnetic metals, multilayers, and alloys, and means for artificial generation of magnetic anisotropy in these materials. This section begins with the free electron model applied to metals [103]. It is the simplest theory, but still gives a very good description of the conductivity in metals. The theory will be expanded to multilayers from the quantum theory point of view. The section ends with a description of magnetic anisotropy using dipole-dipole interaction and spin-pair models.

1.7.1 Electrical Conductivity in Metals

The electrical conductivity of a metal is derived from Ohm's law of electrical resistance, where an electron is considered to move freely independently of others. It is usually expressed in terms of voltage and current, but can also be expressed in the form of current density (current per unit area) and electrical potential (voltage per meter). The conduction is an intrinsic property of a metal. When an electric field is applied to a metal, electrons experience a constant force, $F = -eE$, where, e is the electronic charge and E is an electric field experienced by the charge. The velocity of electrons under this force is given as [103],

$$v = \frac{e\tau}{m} E, \quad (1.3)$$

where τ is the time constant (half-time between successive collisions) and m is the electron mass (mass of a free electron). If, in a constant electric field, there are n electrons per unit volume (electron density), the electrical current density, J , is given as [103],

$$J = \frac{ne^2\tau E}{m}. \quad (1.4)$$

As the current density and electrical fields are related to each other, the electrical conductivity of metals, σ , can be expressed as:

$$\sigma = \frac{J}{E} = \frac{ne^2\tau}{m}. \quad (1.5)$$

In quantum theory of conduction, for real solids, (1.5) still holds true, but with two important modifications: (1) the mass, m is replaced with the effective mass, m^* (where, $m^* > m$), and (2) the time constant, τ is determined from the scattering of spins.

1.7.2 Electron Mobility in Metals

In Section 1.7.1, the conductivity of a material is analyzed using the relaxation time. In this section, the same is expressed using the mobility of the electrons.

The drift velocity of the electron, V_d , is given by the product of the electron mobility and the electric field as:

$$v_d = \mu E. \quad (1.6)$$

Substituting (1.6) into (1.3), we obtain the mobility, μ , as:

$$\mu = \frac{e\tau}{m}. \quad (1.7)$$

By substituting (1.7) into (1.5), the conductivity can be expressed as:

$$\sigma = ne\mu = \frac{1}{\rho}. \quad (1.8)$$

As is obvious from (1.8), the electrical conductivity, σ , is inversely proportional to the resistivity, ρ , and is directly proportional to the electron density, n , and mobility, μ . The large electrical conductivity of metals is primarily due to the high electron density.

1.7.3 Spin-dependent Resistivity in Ferromagnetic Metals

Spin-dependent resistivity in 3-*d* transition metals can be described using Mott's two-current model [51], which arises due to the different resistivities, as a result of the asymmetry in the density of states at the Fermi surface. Figure 1-15 shows the density of occupied states (number of states per unit volume), $N(E)$, of the 3-*d* transition metals that is split into the spin up and spin down bands. The term E inside the parenthesis denotes energy. Note that the magnetic splitting of the *s*-bands is neglected as it has almost no effect on $N(E)$ close to the Fermi energy, E_F . A detail description of the band theory of ferromagnetic metals is beyond the scope of this section, which is described elsewhere [104].

We observe a relative shift of the *d* bands for the spin up and spin down electrons. The $N(E)$ of the 3-*d* spin up electrons is completely filled up and lies below E_F , whereas the $N(E)$ of the spin down electrons is partially filled up, and extends beyond E_F . That means the spin down *s*-electrons, as compared to the spin up *s*-electrons, are more prone to scattering due to the available empty space between the spin down 4-*s* and the spin down 3-*d* bands. Since spin down electrons have more unfilled states to scatter to, the resistivity will be higher for these electrons.

Figure 1-16 shows Mott's two-current model [51] for 3-*d* ferromagnetic transition metals. The model is based on the following assumptions:

1. Spin of the charge carrier is preserved, i.e., no change in spin orientation occurs due to scattering.
2. Conduction takes place almost exclusively by means of *s*-electrons.
3. It is assumed that the resistivities due to the scattering of the spin up 4-*s* and the spin up 3-*d* electrons can be added. Similarly, the resistivities due to the spin down 4-*s* and the spin down 3-*d* electrons can be added.

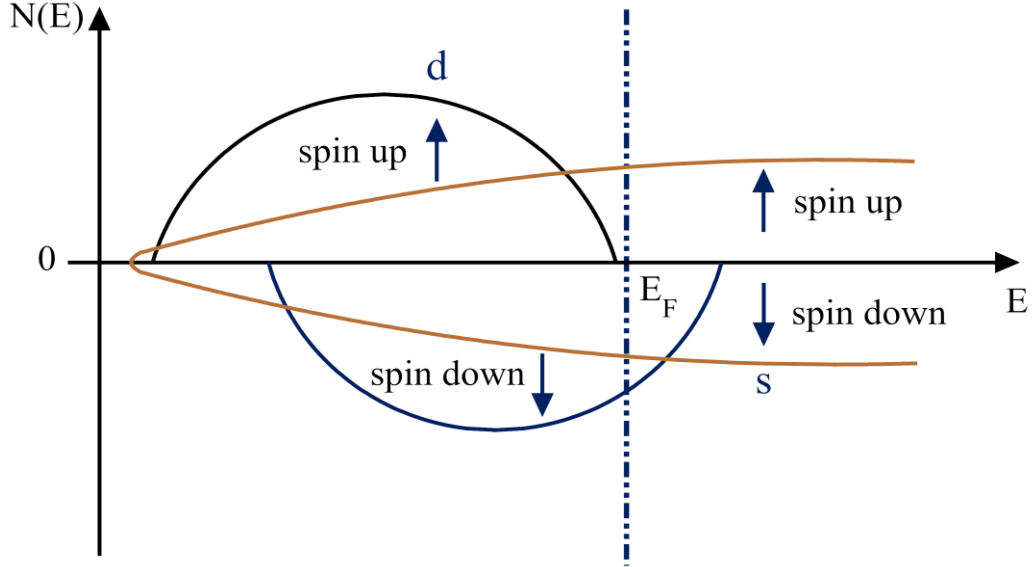


Figure 1-15 Schematic representation of the density of states of 3-d transition metal. Note the density of d states with spin down at the Fermi energy, E_F .

In Figure 1-16, the resistivities arising from the scattering of the 4-s and 3-d electrons are denoted by ρ_{ss} and ρ_{sd} , respectively. The notation ss stands for the interaction that takes place between the 4-s conduction electrons whereas the notation sd stands for the interaction that takes place between the 4-s conduction electrons and the 3-d electrons. The + and - signs indicate spin up and spin down, respectively. As the available empty space in the density of states of the 3-d spin down electrons is much bigger than the density of state of the 4-s spin down electrons (see Figure 1-15), the resistivity due to the sd interaction is much larger than the resistivity due to the ss interaction. On the other hand, as the density of states of the 3-d spin up electrons is completely filled up, the 4-s spin up electrons can only scatter to other 4-s spin up states as there is no room to interact with the 3-d spin up electrons (see again Figure 1-15), the resistivity due to the ss interaction is much larger than the resistivity due to the sd interaction.

In Figure 1-16, the majority of the resistivity in the lower branch is due to the interaction between the spin down 4-s and 3-d electrons whereas the majority of the resistivity in the upper branch is due to the interaction between the 4-s electrons themselves (i.e., $\rho_{ss}^+ \gg \rho_{sd}^+$). Note that due to the symmetry of the density of states of s-electrons, $\rho_{ss}^- = \rho_{ss}^+$. After simplification, the equivalent resistivity, ρ , of the ferromagnetic material is given from the parallel combination of the resistivities due to the spin down ($\rho^- = \rho_{ss}^- + \rho_{sd}^-$) and spin up ($\rho^+ = \rho_{ss}^+ + \rho_{sd}^+$) electrons as:

$$\rho = \frac{\rho^+ \rho^-}{(\rho^+ + \rho^-)}. \quad (1.9)$$

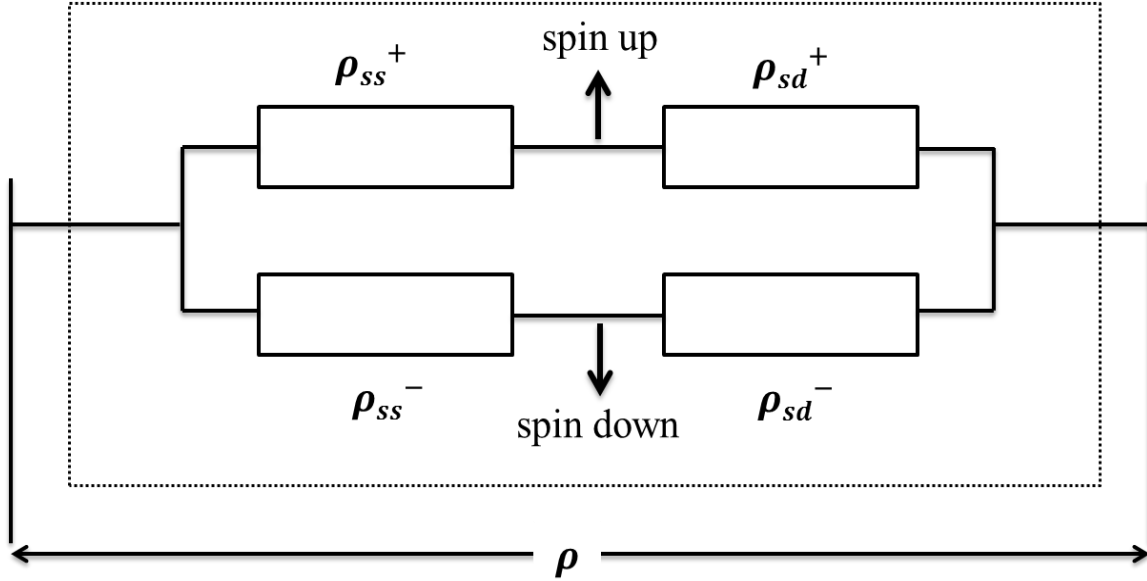


Figure 1-16 Schematic illustration of two-current model for 3-d transition ferromagnetic metals.

1.7.4 Spin-dependent Resistivity in Magnetic Multilayers

The argument given in Section 1.7.3 for ferromagnetic metals is the basis for the quantitative understanding of the GMR effect in magnetic multilayers. Figure 1-17 represents Mott's two-current model (applied to Figure 1-5, page 10, Section 1.3.3.1) when the magnetic moments in the adjacent ferromagnetic layers are (a) antiparallel, i.e., $H = 0$, and (b) parallel, i.e., $H \neq 0$. Figure 1-17(a) shows the resistivity arising from the spin up and spin down electrons (and thus currents), when the magnetic moments in the adjacent ferromagnetic layers are aligned antiparallel to each other (when no field is present), and Figure 1-17(b) shows the same but when the magnetic moments of the adjacent ferromagnetic layers are aligned parallel to each other towards the direction of the applied field.

The change in resistivity due to the applied field can be given as,

$$\frac{\Delta\rho}{\rho_p} = \frac{(\rho_a - \rho_p)}{\rho_p}, \quad (1.10)$$

where ρ_a is the resistivity when no magnetic field is applied, and is obtained from the parallel combinations of the resistivities shown in Figure 1-17 (a) and ρ_p is the resistivity at the applied magnetic field, and is obtained from the parallel combinations of the resistivities shown in Figure 1-17 (b).

After simplification, the relative change in resistivity due to the applied field is given as [25]:

$$\frac{\Delta\rho}{\rho_p} = \frac{(1 - \alpha)^2}{4\alpha}, \quad (1.11)$$

where α is the scattering asymmetry parameter, and is given by ρ^-/ρ^+ . The magnitude of the GMR effect, thus, depends on the difference between ρ^- and ρ^+ in (1.11), i.e., the difference between the spin up (+) and the spin down (-) electrons.

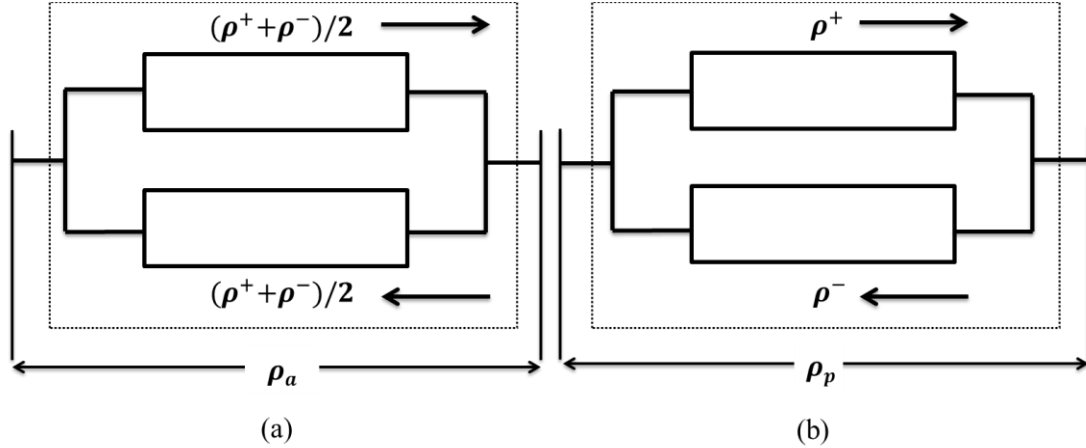


Figure 1-17 Schematic illustration of Mott's two-current model applied to multilayers when the magnetic moments of the adjacent ferromagnetic layers are (a) antiparallel ($H = 0$) and (b) parallel ($H \neq 0$). The black arrows represent the current channels.

1.7.5 Magnetic Anisotropy

Sections 1.7.1 through 1.7.4 covered electron transport in normal metals, 3-*d* transition metals, and ferromagnetic multilayers. This section deals with the magnetic anisotropy, an energy change in the ferromagnetic materials depending on how the magnetic moments are aligned in their crystal lattice. Usually in metals, if no interaction occurs between the adjacent magnetic moments, spontaneous magnetization can point in any directions in the crystal. However, in 3-*d* transition metals Co and Fe, their multilayers, and alloys, the spontaneous magnetization can have several easy axes along which magnetizations prefer to align [105]. Rotation of the magnetic moments away from their easy axis is possible via external forces (e.g., strain, high magnetic field, etc.).

The magnetic anisotropy in ferromagnetic multilayers has been attributed to many likely causes, such as ordered arrays of atoms, crystal magnetic anisotropy due to the symmetry of the crystal, induced magnetic anisotropy (uniaxial magnetic anisotropy), shape magnetic anisotropy (due to the shape of the film), and magnetostriction (fractional change in length of the film). In the subsequent sections, magnetic anisotropy energy will be calculated for the ferromagnetic materials that have cubic and hexagonal lattice structures, relevant to the materials presented in this thesis.

1.7.5.1 Anisotropy in Cubic Structures

Figure 1-18 shows a cubic lattice structure in the *x-y* plane. Since the spin-pair energy for distant-pairs is small, the magnetic anisotropy energy, E , is calculated by considering only the interactions between the first

nearest-neighbour spins along the x - and y - axes. After simplification [105], the energy of the nearest-neighbour spin-pairs (due to the dipole-dipole interaction) is given as [106],

$$E_1 = E_2 = -l \left(\cos^2 \theta - \frac{1}{3} \right) \quad (1.12)$$

and,

$$E_3 = E_4 = -l \left\{ \cos^2 (\pi/2 - \theta) - \frac{1}{3} \right\} / \eta^3,$$

where l is an orbital magnetic moment and is given by $l = 3m^2 / 4\pi\mu_0 r_{ij}^3$ [105], θ is the angle made by the magnetic moment with the direction of the easy axis (along the x - axis), μ_0 is the permeability of vacuum, η is a distance multiplier, and r_{ij} is an interatomic distance between nearest spin-pairs. In Figure 1-18, r_{ij} is denoted by r for simplicity. The length of each spin-pair is assumed to be much smaller than the distance between them. The total energy, E , which is a sum of the interaction energies between the adjacent spin-pairs along the x - and the y - directions in the lattice, is given as:

$$E = \sum_{i=1}^4 E_i = -2l \left(1 - \frac{1}{\eta^3} \right) \cos^2 \theta + const. \quad (1.13)$$

The condition for a minimum magnetization energy is $\eta > 1$, i.e., $(1 - 1/\eta^3) > 0$ and $\theta = 0$.

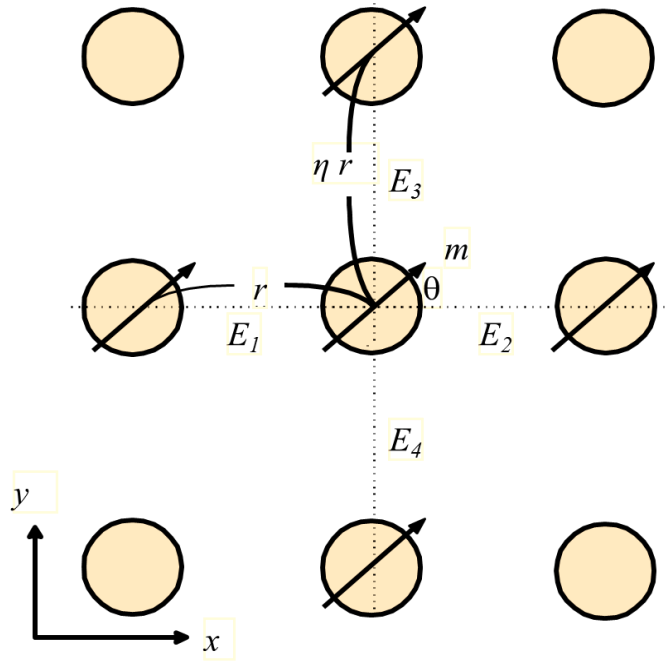


Figure 1-18 Two dimensional view ($x - y$ plane) of a cubic lattice structure.

The relationship between the angle made by the magnetic moment with the easy axis, θ , and the direction of the applied field along the easy and hard axes, as calculated using (1.13) is summarized in Table 1-3.

Table 1-3 Relationships between the magnetic moments and their orientations.

Direction of the applied magnetic field	Atomic spacing	Energy, E	Magnetization direction
x -direction ($\theta = 0^\circ$)	narrow	minimum	$m //$ easy axis
y -direction ($\theta = 90^\circ$)	broad	maximum	$m //$ hard axis

1.7.5.2 Anisotropy in Hexagonal Structures

In this section, the directional magnetic properties of hexagonal Co (also known as hcp-Co) crystals will be studied. At room temperature, the hcp-Co exhibits uniaxial magnetic anisotropy with the easy axis of magnetization lying along the c - axis. Figure 1-19 shows (a) a crystal structure of the hcp-Co and (b) its initial magnetization curves when the magnetic field is applied along the c - axis $[0001]$ (easy axis) and a - axis $[10\bar{1}0]$ (hard axis). Interestingly, all directions in a - axis ($10\bar{1}0$), also known as basal plane, are found to be equally hard. Under these circumstances, the anisotropy energy, E , depends only on the angle, θ , between the direction of the magnetization, M , and the c - axis. The difference seen in the orientation of the magnetization curves in Figure 1-19 (b) is due to the uniaxial magnetic anisotropy.

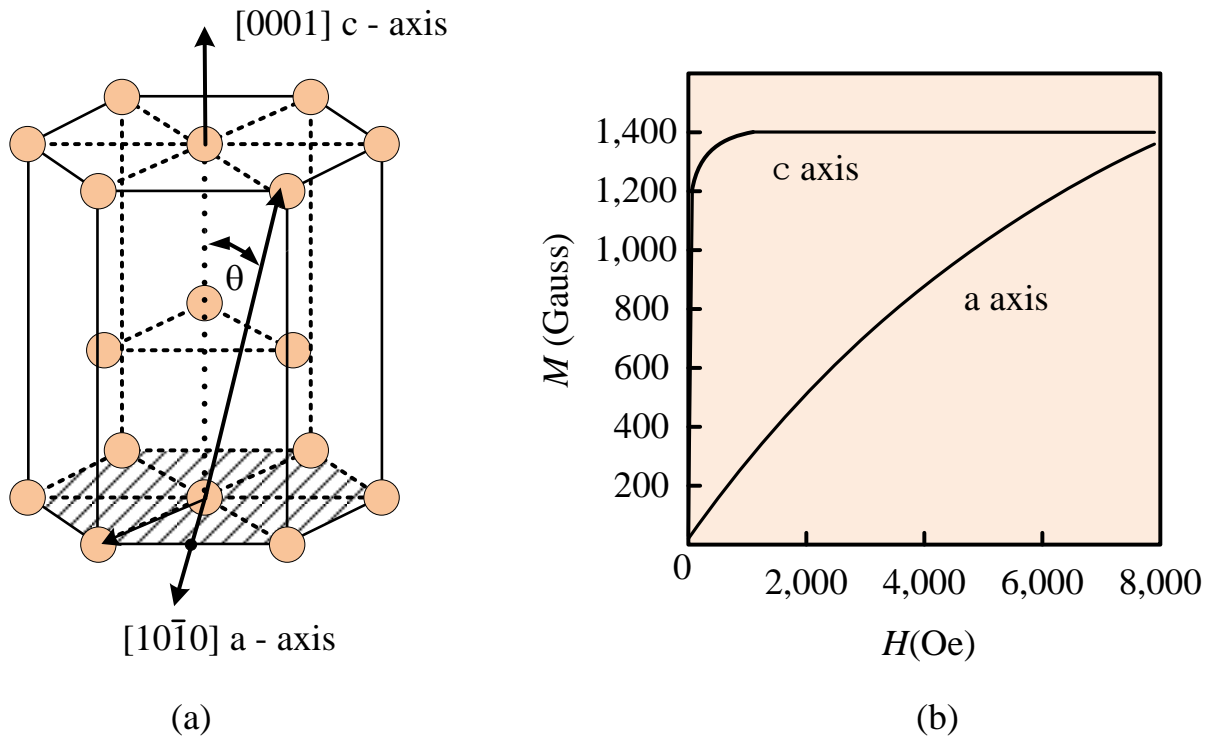


Figure 1-19 (a) Single crystal of hcp-Co and (b) initial magnetization curves for applied field along the c - and a - axes. θ is the angle between the magnetization and the c - axis.

The anisotropy energy needed to turn the magnetic moments from the easy axis towards the hard axis by the angle, θ , can be written to a close approximation as [105],

$$E(\theta) = K_u \sin^2(\theta), \quad (1.14)$$

where K_u is the uniaxial magnetic anisotropy constant and represents the magnitude of the anisotropy energy. In (1.14) higher order anisotropic effects have been omitted. For positive K_u (i.e., $K_u > 0$), the energy in (1.14) is minimum at $\theta = 0$, and the magnetic easy axis lies along the c - axis. In this case, the magnetization can point either up or down only. For negative K_u (i.e., $K_u < 0$), the energy in (1.14) is minimum at $\theta = 90^\circ$, and the magnetic easy axis lies along the a - axis (i.e., the basal plane). When θ is neither 0 nor 90° , the magnetic axis lies anywhere between the easy c - axis and the hard a - axis.

The anisotropy energy in (1.14) of a magnetic material strongly affects the magnetic properties, such as the coercivity and remnance [104]. The property is therefore, of considerable interest in the design of magnetic devices. Experimentally, magnetic anisotropy energy can be calculated using the area surrounded by the magnetization curves between the easy and hard axes.

1.7.5.3 Anisotropy Measurement from Torque Curves

The accurate means of determining the magnetic anisotropy constant, K_u , is using a uniformly magnetized single domain circular film as shown in Figure 1-20. If the film is magnetically isotropic and posses constant permeability, any applied magnetic field will distribute uniform magnetic moments in the film. If the easy axis is near the direction of the magnetization, an application of small magnetic field, H , can easily rotate the magnetization towards the easy axis. Figure 1-20 (a) is a case where the direction of the magnetization is along the easy axis, i.e., it is the minimum magnetic anisotropy energy condition in the absence of H fields. If H is strong enough, the magnetization, M_s , will be parallel to H and the angle between M_s and the easy axis will be the same as the angle between H and the easy axis. This condition is shown in Figure 1-20 (b).

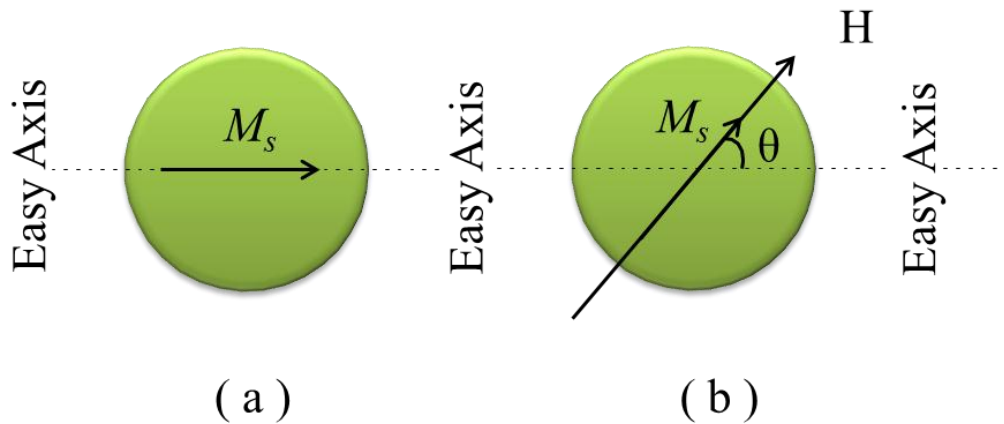


Figure 1-20 Magnetization rotation model: (a) the direction of spontaneous magnetization, M_s , and the easy axis ($\theta = 0$) and (b) M_s makes an angle, θ with the easy axis.

The angle dependence of the anisotropy energy is given from (1.14) as,

$$E(\theta) = K_u \sin^2(\theta), \quad (1.15)$$

where, K_u is the magnetic anisotropy constant. When the energy of the magnetization depends on the angle, the derivative of the energy with respect to the angle gives rise to a torque. The torque on the crystal per unit volume is given as:

$$L(\theta) = -\frac{\delta E(\theta)}{\delta \theta}. \quad (1.16)$$

From (1.15) and (1.16), the torque exerted by the crystal on M_s can be given as:

$$L(\theta) = -K_u \sin(2\theta). \quad (1.17)$$

The torque is, therefore, a function of the angle, θ . K_u is constant for a given material system. Experimentally, K_u can be obtained from the amplitude of the torque curve.

1.7.5.4 Anisotropy Measurement from Magnetization Curves

The analysis in Section 1.7.5.3 is valid when H field is strong enough to align M_s towards its direction. However, in real situations, this condition is not always met, and therefore, we have the situation as shown in Figure 1-21. Here, ϕ is the angle made by H with the easy axis and θ is the angle between M_s and the easy axis. The difference between the direction of H and the direction of M_s is $\phi - \theta$.

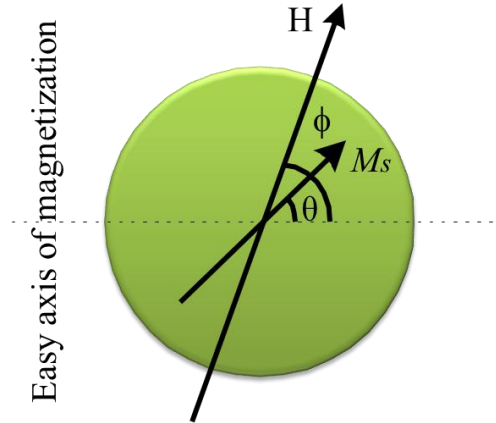


Figure 1-21 Magnetization rotation model for small fields, H .

From again equation (1.14), we have the anisotropy energy, E_A , per unit volume as:

$$E_A = K_u \sin^2(\theta). \quad (1.18)$$

The magnetostatic energy due to the H field is given as:

$$E_H = -M_s H \cos(\phi - \theta). \quad (1.19)$$

The total energy, E , is thus,

$$E = E_A + E_H = K_u \sin^2(\theta) - M_s H \cos(\phi - \theta). \quad (1.20)$$

The condition for minimum total energy is,

$$\frac{\partial E}{\partial \theta} = 2K_u \sin(\theta)\cos(\theta) - M_s H \sin(\phi - \theta) = 0, \quad (1.21)$$

and,

$$\frac{\partial^2 E}{\partial \theta^2} = 2K_u \cos(2\theta) + M_s H \cos(\phi - \theta) > 0. \quad (1.22)$$

From (1.19), the magnetic moment along the direction of the H field is,

$$M = M_s \cos(\phi - \theta). \quad (1.23)$$

Two special cases will be discussed below: (1) magnetic field applied towards the easy axis of magnetization and (2) magnetic field applied towards the hard axis of magnetization.

1.7.5.4.1 Magnetic Field towards Easy Axis

If the strong magnetic field is applied towards the easy axis of the magnetization, ϕ is set to 0, and both H and M_s point towards the positive directions. Equations (1.21) and (1.22) can be re-written as,

$$\frac{\partial E}{\partial \theta} = 2K_u \sin(\theta)\cos(\theta) - M_s H \sin(0 - \theta) = 0, \quad (1.24)$$

or,

$$\cos(\theta) = -\frac{M_s H}{2K_u}, \quad (1.25)$$

and,

$$\frac{\partial^2 E}{\partial \theta^2} = 2K_u \cos(2\theta) + M_s H \cos(0 - \theta) > 0. \quad (1.26)$$

Eliminating θ from (1.25) and (1.26), the value of H is obtained as,

$$H > \frac{2K_u}{M_s} \text{ or } -\frac{2K_u}{M_s} > H. \quad (1.27)$$

Substituting (1.25) into (1.23), the magnitude of the total magnetization, M , at $\phi = 0$ can be determined as:

$$M = -\frac{M_s^2}{2K_u} H. \quad (1.28)$$

Equation (1.28) shows that the magnitude of M is proportional to the magnitude of H . On substituting the value of H , say, $H = \pm \frac{2K_u}{M_s}$ from (1.27) into (1.28), the magnitude of M can be calculated as:

$$M = \mp M_s. \quad (1.29)$$

That means, when H equals to $\frac{2K_u}{M_s}$, the total magnetization, M , is actually the saturation magnetization, M_s . Under this condition, magnetic moments in the film are either aligned along the directions of $\theta = 0$ or $\theta = \pi$, meaning that the magnetization curve is a square hysteresis loop.

1.7.5.4.2 Magnetic Field towards Hard Axis

If the strong magnetic field is applied parallel to the hard axis of magnetization, ϕ is set to $\pi/2$, (1.21) and (1.22) can be re-written as,

$$\frac{\partial E}{\partial \theta} = 2K_u \sin(\theta)\cos(\theta) - M_s H \sin\left(\frac{\pi}{2} - \theta\right) = 0, \quad (1.30)$$

or,

$$\sin(\theta) = \frac{M_s H}{2K_u}, \quad (1.31)$$

and,

$$\frac{\partial^2 E}{\partial \theta^2} = 2K_u \cos(2\theta) + M_s H \cos\left(\frac{\pi}{2} - \theta\right) > 0. \quad (1.32)$$

Eliminating θ from (1.31) and (1.32) gives:

$$H > \frac{2K_u}{M_s} \text{ or } -\frac{2K_u}{M_s} > H. \quad (1.33)$$

The magnitude of M can be obtained by substituting (1.31) into (1.23) as:

$$M = M_s \cos\left(\frac{\pi}{2} - \theta\right) = M_s \sin(\theta) = \frac{M_s^2}{2K_u} H. \quad (1.34)$$

At $H = \pm \frac{2K_u}{M_s}$, (1.34) becomes:

$$M = \frac{M_S^2}{2K_u} H = \frac{M_S^2}{2K_u} \left(\pm \frac{2K_u}{M_S} \right) = \pm M_S. \quad (1.35)$$

When the saturating field, H , equals $\pm \frac{2K_u}{M_S}$, the total magnetization, M , is actually a saturation

magnetization, M_S . In (1.34), M_S and K_u are constants for any material system, meaning that (1.34) represents a straight line of M versus H with a constant positive slope (i.e., no hysteresis).

1.8 Film Preparation, Measurement, and Characterization

In Sections 1.4 through 1.6, we introduced experimental surveys of the GMR effect in multilayers and alloys, and discussed the means for artificial generation of magnetic anisotropy in these nanostructures. Section 1.7 covered theoretical aspects of spin-dependent conductivity and magnetic anisotropy. This section briefly discusses various film preparation methods and experimental approaches taken to characterize magnetic nanostructures developed in this thesis.

1.8.1 Classification of Film Preparation Methods

The properties of magnetic materials are governed by the methods by which they are deposited. A wide variety of deposition methods have been used to develop magnetic thin films, depending on the materials used and their intended application [48]. Figure 1-22 shows various deposition processes used in the development of magnetic hybrid nanostructures. It consists of primarily physical vapor deposition processes, chemical deposition processes, and non-equilibrium deposition processes.

The physical vapor deposition processes are classified into sputtering and thermal processes. Sputtering is a non-thermal process, and has been widely used for the deposition of multilayers [19] and granular alloys [107] that show GMR, and high-moment nanoparticles, mostly because it permits almost any combination of elements to be deposited. It has been useful for depositing high melting point metals. Further literature on these processes is available in [48] and [97].

Thermal deposition processes are further classified into resistive heating, molecular beam epitaxy (MBE), e-beam evaporation, and pulsed laser deposition methods. The resistive heating process is the heating of source materials and evaporating them using resistive filament at pressure below 1×10^{-6} Torr. MBE is a slow deposition process. It demands ultra-high vacuum, at or below 10^{-11} Torr, at all times [28]. E-beam evaporation method used in the growth of the buffer layers and multilayers presented in this thesis is principally similar to the MBE method and is simpler to operate. The non-equilibrium pulsed laser deposition (PLD) method is an improved thermal process, and is considered good to deposit alloys and oxide films with a controlled chemical composition [19], [108]. Other non-equilibrium processes such as melt-spun have been used in the preparation of a long ductile ribbon [109] whereas mechanical alloying [82], [92] has been used in the preparation of granular alloys, however, their use is mostly limited to bulk films.

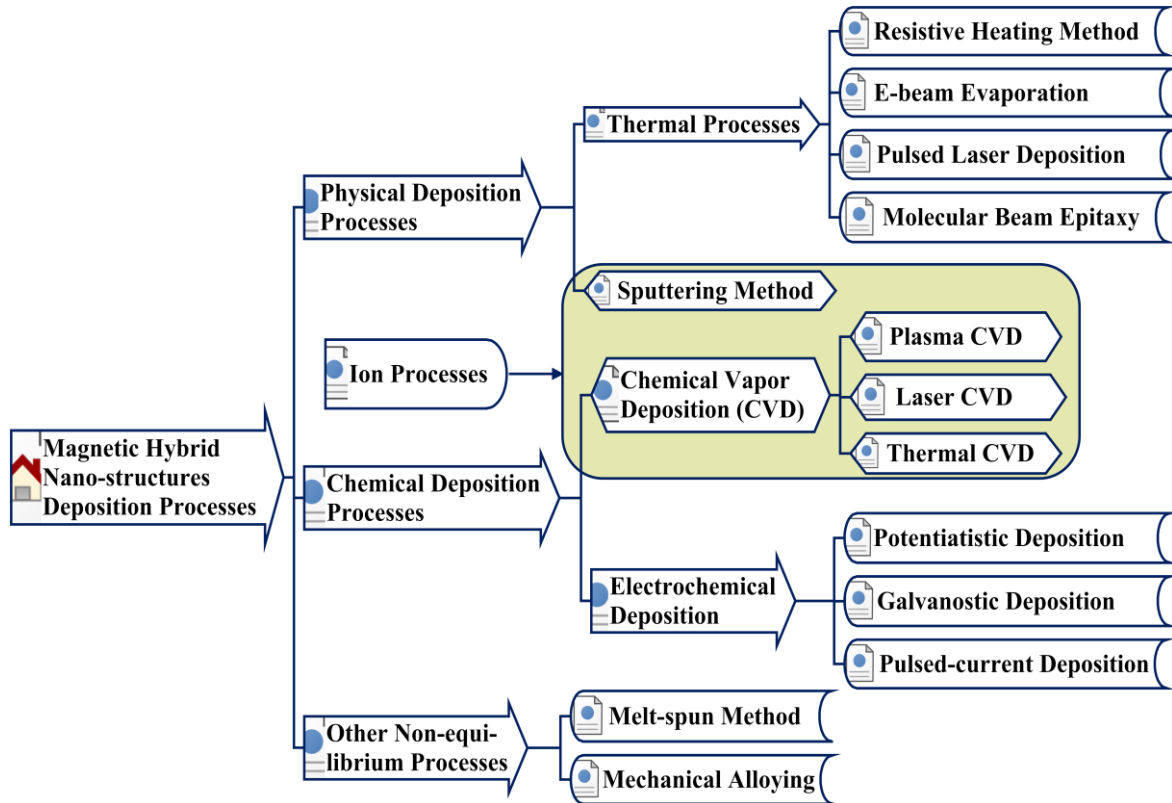


Figure 1-22 Various film preparation processes.

Chemical deposition processes are classified into potentiostatic (voltage controlled) and galvanostatic (current controlled) deposition methods. Galvanostatic methods are further classified into constant-current [110] and pulsed-current [46] deposition methods. Pulsed-current deposition method has several benefits over constant-current deposition method [93], [110], [111] and has become one of the preferred deposition methods due to its simplicity and ease of use. Grain sizes of the nanostructures prepared using pulsed-current deposition method is found to be smaller and finer than that of the grains developed using constant-current method. These benefits make pulsed-current deposition one of the best methods for the development of magnetic sensors and high-magnetic moment nanoparticles. This will be further discussed in Sections 3.1 and 3.2.

1.8.2 Measurement and Characterization

1.8.2.1 Experimental Methods

In this section, experimental methods used in this thesis for the measurement and characterization of the ferromagnetic nanostructures are briefly discussed. Section 1.8.2.2 highlights the composition and the thickness analysis schemes. Section 1.8.2.3 discusses Bragg's diffraction. Section 1.8.2.4 discusses various MR measurement configurations used in this thesis. It also briefly discusses a standard dc four-point probe resistance measurement scheme and its equivalent electrical circuit. Section 1.8.2.5 discusses the measurement of magnetic properties using a vibrating sample magnetometer (VSM). This section concludes with a brief description of the rf-SQUID magnetometer.

1.8.2.2 Composition and Thickness Analysis

The composition of the film was determined using highly sensitive microbalance and energy dispersive and X-ray analysis. The thickness of the film was calculated from the measured mass of the deposited film obtained from the atomic flame emission spectrometer, assuming the density of the film same as the density of bulk material. For the electrodeposited films, the nominal thickness was calculated using chemical methods, which will be discussed in Section 3.2. The periodicity of the multilayers was determined using a low angle X-ray diffractometer.

1.8.2.3 X-ray Diffraction

X-ray diffraction patterns were obtained using a Rigaku diffractometer ($CuK\alpha$ radiation, $\lambda = 0.15406$ nm, 60 kV, 200 mA) to study the crystallographic structure of the ferromagnetic multilayers, granular alloys, and nanoparticles.

Figure 1-23 shows Bragg's diffraction. The condition for constructive interference to occur can be given as,

$$2d \sin \theta_B = n\lambda, \quad (1.36)$$

where θ_B is the diffraction angle, d is the plane spacing, n is the order of reflection, and λ is the wavelength of radiation, which is 0.15406 nm.

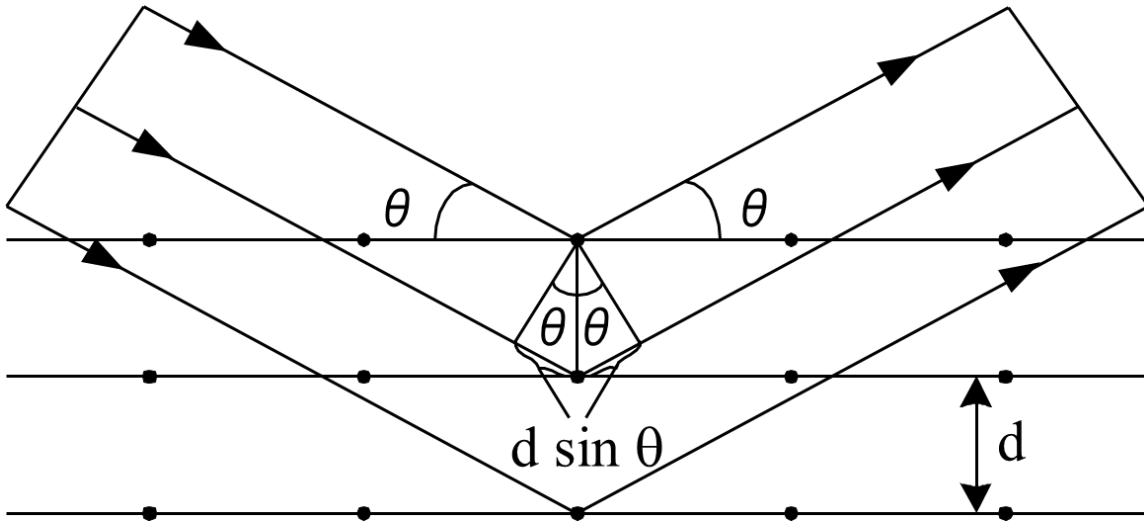


Figure 1-23 Bragg's diffraction.

The particle size of the granular film was estimated using the Shearer's formulae as,

$$t = \frac{0.9 \times \lambda}{B \times \sin \theta_B}, \quad (1.37)$$

where t is the diameter of the particle, B is the full width half maximum, and θ_B is the Bragg's angle.

With the known value of d from (1.36) and crystallographic plane (hkl) from ASTM³ table, the lattice constant of the crystal can also be calculated.

1.8.2.4 Magnetoresistance Measurement

Figure 1-24 shows a normal view of a film and six different measurement configurations. For the randomly oriented (isotropic) films, the MR ratio was examined by varying the field, H , and current, I , in two different configurations, whereas, for the uniaxially oriented (anisotropic) films, the MR ratio was examined by varying the relative direction of H and I in four different configurations. The corresponding arrows show the orientation of spins, the directions of the easy and hard axes, the direction of the applied field, and the direction of the current.

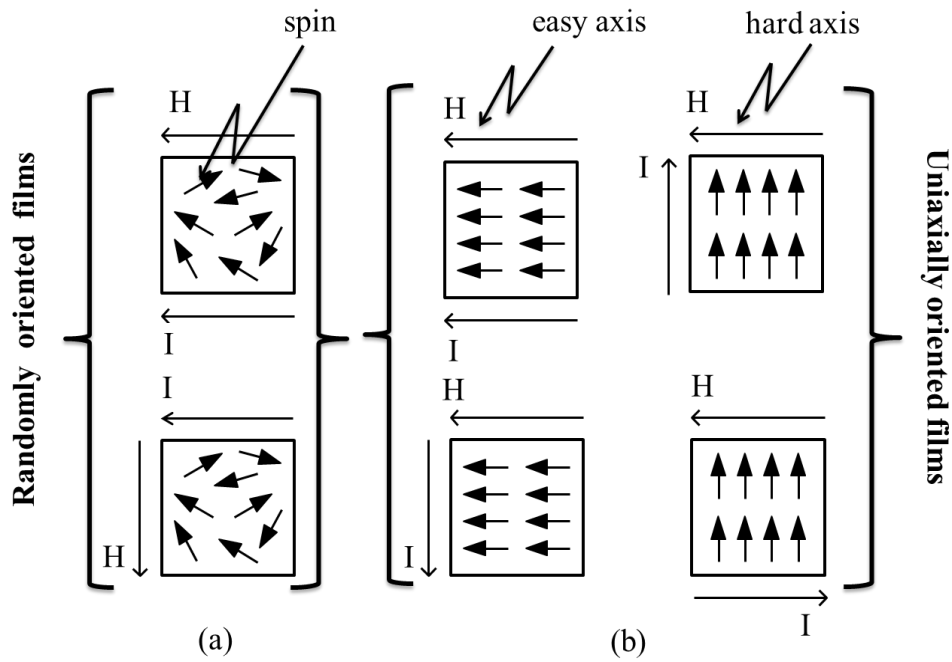


Figure 1-24 Various magnetoresistance measurement configurations.

Figure 1-25 shows (a) the schematic of a four-point probe and (b) the electrical circuit, where R_v is a variable resistor, R_1 , R_2 , and R_3 are the film resistances, E is the drive potential, and x_1 , x_2 , x_3 , and x_4 are the probe resistances.

The current flowing through the circuit can be given as:

$$I = \frac{E}{x_1 + x_4 + R_1 + R_2 + R_3 + R_v}. \quad (1.38)$$

V is the voltmeter reading, which can be given as,

³ American Society for Testing and Materials.

$$V = \frac{ER_2}{x_1 + x_4 + R_1 + R_2 + R_3 + R_v}. \quad (1.39)$$

From (1.38) and (1.39), we obtain,

$$R_2 = \frac{V}{I}. \quad (1.40)$$

A good thing about the four-point probe measurement scheme is that the measured film resistance does not include any probe resistances. This eliminates any errors in the MR measurement. From the information of the amount of the current passed, the distance between the voltage probes, and the cross-sectional area, the resistivity of the films can be determined [112].

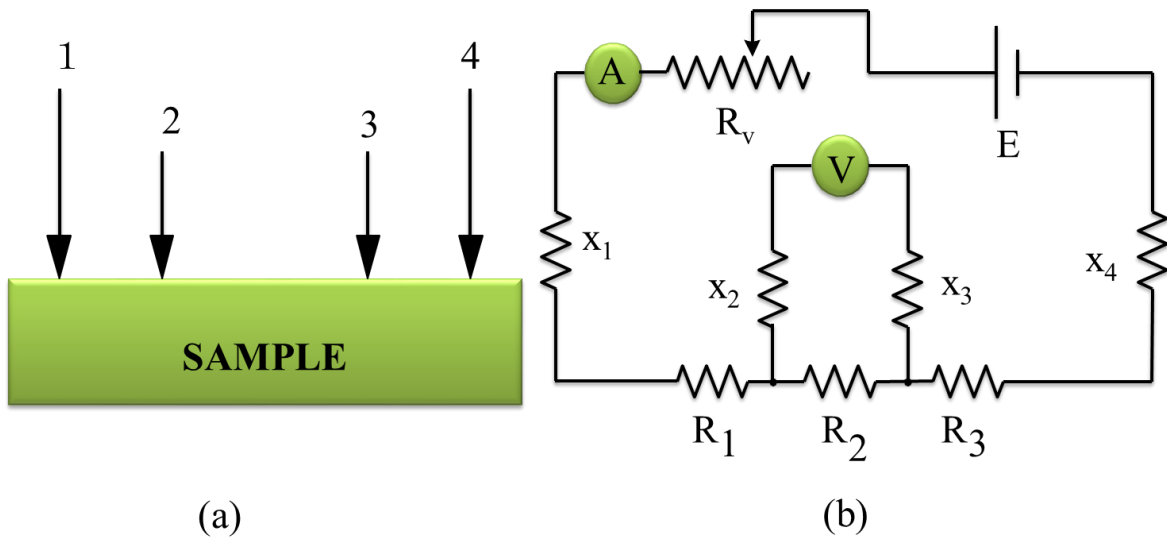


Figure 1-25 (a) Schematic of a four-point probe method and (b) a resistor circuit. The current is fed through terminals 1 and 4 and the voltage is measured between terminals 2 and 3.

1.8.2.5 Vibrating Sample Magnetometer

In this thesis, the effects of magnetic and non-magnetic layer thicknesses and film compositions on the magnetic properties (e.g., saturation magnetization, M_S , remnant magnetization, M_r , coercive force, H_c , anisotropy constant, K_u , etc.) were all studied using a vibrating sample magnetometer (VSM). The VSM was calibrated using the standard Ni film (i.e., a sample with known saturation magnetization) that had the same size and the same shape as that of the films, before taking measurement readings. The theoretical basis for calculating saturation magnetization from the vibrating dipole magnetic moments is given in Appendix A.

1.8.2.6 Superconducting Quantum Interference Device

Superconducting quantum interference device (rf-SQUID) magnetometer is extremely sensitive to the grain interactions and provides a good method for investigating magnetic properties of super-paramagnetic like

granular alloys [1], [80]. In this thesis, rf-SQUID magnetometer was used to obtain the field dependence of magnetization, i.e., zero-field-cooled (ZFC) and field-cooled (FC) magnetization. The blocking temperature of our film was obtained from the ZFC curves.

The mean Co grain size was estimated as,

$$K_A v = 25k_B T_B, \quad (1.41)$$

where K_A is the magnetic anisotropy constant, v is the volume of a super paramagnetic Co grain corresponding to the blocking temperature T_B , and k_B is the Boltzmann's constant.

1.9 Thesis Outline

Chapter 1, Sections 1.7.1 through 1.7.5 of this thesis, consists of theory on the MR effect and magnetic anisotropy. Section 1.8 consists of sample preparation, measurement, and characterization of the magnetic nanostructures. The remainder of this thesis (Chapters 2 through 6) presents manuscripts that have been published or accepted for publication in international journals.

In Chapter 2, the effect of oblique incidence evaporation and magnetic annealing on GMR and magnetic anisotropy of Co/Au multilayers are presented as the ferromagnetic and nonmagnetic layer thicknesses are systematically changed.

Chapter 3 introduces pulsed-current deposition and presents experimental results on the effect of strain on GMR and magnetic properties of Co/Ag multilayers grown on the polyimide substrates as the ferromagnetic layer thickness is changed. It shows a relationship between the field dependence of the MR ratio and the magnetization curves for low magnetic fields.

Chapter 4 presents measured results on the GMR effect and the magnetic properties of Co/Cu multilayers grown using pulsed-current deposition on the polyimide substrates. As in Chapter 3, it reports the effect of strain and ferromagnetic layer thickness on the physical properties of Co/Cu multilayers. It shows a relationship between stress, strain, field dependence of the MR ratio, and magnetic anisotropy.

Chapter 5 presents a detail investigation of the GMR effect, the saturation magnetization, and the microstructure of Co-Au granular alloys. It shows the effect of the deposition current density on the magnetization, microstructure, and grain sizes.

Chapter 6 describes the preparation of the high-magnetic moment FeCo nanostructures. It then presents measured results of the magnetization and microstructure of the FeCo nanostructures.

Chapter 7 is the concluding chapter of the thesis. It summarises the thesis, briefly describes some of the limitations and potential applications, and recommends for future work.

Chapter 2: Magnetoresistance Effect and Magnetic Properties of Co/Au Multilayers⁴

2.1 Introduction

Co/Au multilayers are interesting materials to study for a range of applications that exploit spin-dependent resistivity behavior, under an applied magnetic field [16], [54]. The spin-dependent resistivity of the Co/Au multilayer is influenced by the interfacial states between the layers of Co and Au [26], [113]. There is a 15 % lattice mismatch between Co and Au. In addition, the bulk-phase diagram shows that Co and Au are immiscible at temperature below 693 K [114], meaning that they can be grown with clear and abrupt interfaces [115], [33].

In the study of the non-magnetic layer thickness dependence of the MR ratio, it has been found that the spin-dependent resistivity of the multilayer becomes independent of the relative orientation of the magnetic moments when the ferromagnetic Co layers are separated by the nonmagnetic Au layers that have thicknesses larger than the mean free path of the conduction electrons [116], [117]. However, the influence of the change of the Co and Au layer thicknesses in various ratios on the MR effect of the multilayer has not yet been fully understood.

To investigate these effects, we took following two approaches:

1. Co and Au layers with various thicknesses and ratios were grown by varying the deposition angle using a specially designed oblique incidence evaporation method.
2. The Co/Au multilayers were magnetically annealed at their saturation field to strengthen their magnetic anisotropy.

These multilayers developed strong magnetic anisotropy ($-0.5 \text{ kOe} < H < +0.5 \text{ kOe}$) at room temperature. The MR effect of the anisotropic Co/Au multilayers was found to be larger than the MR effect of the isotropic Co/Au multilayers. The improvement of the MR ratio and the magnetic anisotropy in Co/Au multilayers is attributed to the optimum structure and interfacial states of the film [118].

⁴ A version of this chapter has been published. Reprinted from [3] with permission. © 2007, Elsevier. Rizal, C. Study of magnetic anisotropy and magnetoresistance effects in ferromagnetic Co/Au multilayer films prepared by e-beam evaporation. *Journal of Magnetism and Magnetic Materials*. 3/2007.

2.2 Experimental Procedure

A series of $[\text{Co } (t_{\text{Co}}) \text{ nm/Au } (t_{\text{Au}}) \text{ nm}]_N$ multilayers was grown onto the glass substrates using e-beam evaporation, where t_{Co} and t_{Au} are the thicknesses of the Co and Au layers, respectively. The subscript N outside the parenthesis indicates the number of bilayers in the film. The multilayers were grown by alternatively evaporating Co and Au layers on the polished glass substrate using oblique angle e-beam evaporation. The pressure and deposition rate were maintained at 10^{-6} Torr and 0.1 nm/s, respectively.

The thickness of the deposited film was observed using the quartz crystal monitor and later confirmed using the low angle X-ray diffraction measurement (a preferred method used to study the film periodicity in the multilayers). The X-ray spectra were collected using a Rigaku X-ray diffractometer in the $\theta - 2\theta$ scans with the monochromatic $\text{CuK}\alpha$ radiation ($\lambda = 0.15406$ nm). The calibration of the diffractometer was done using standard Au or Si samples.

The deposition angle, θ , of the direction of evaporation, on the plane of the substrate was changed in the range of $\theta = 0^\circ$ (i.e., its surface normal to the direction of evaporation) to 75° (i.e., at an oblique angle). The oblique incidence evaporation arrangement was locally built inside the e-beam chamber.

It was assumed that the Co particles were randomly distributed along the substrate surface at the onset of the e-beam evaporation. Therefore, the multilayers were magnetically annealed at 3 kOe for 30 minutes (this scheme is given in page 21, Figure 1-13) to strengthen magnetic ordering. The magnetic annealing was carried out in a tubular glass enclosure, by placing multilayers in between two electromagnets (pressure below 1×10^{-6} Torr and temperature at 573 K).

Magnetic properties of the $[\text{Co } (t_{\text{Co}}) \text{ nm/Au } (t_{\text{Au}}) \text{ nm}]_{20}$ multilayers were evaluated using VSM and magnetic balance by applying the magnetic field along the transverse (in plane) and the longitudinal (in plane) directions of the easy axis and the current. The magnetic anisotropy constant was determined from the measured magnetization curves.

The MR was measured in two different configurations for the isotropic multilayers and four different configurations for the anisotropic multilayers, by varying the relative direction of the applied field, H , and the current, I , using the standard four-point probe method at the constant dc current of 3 mA.

The field dependence of the MR ratio was measured in six different configurations (the measurement configurations are shown in page 36, Figure 1-24) by varying the relative direction of H and I as the Co and Au layers were changed. The magnetic field was applied from 0 to ± 21 kOe.

2.3 Results and Discussions

In this section, experimental results of the magnetization, the microstructure, and the MR effect of the (a) as-deposited ($\theta = 0$) and (b) obliquely deposited ($\theta = 45^\circ$) $[\text{Co } (t_{\text{Co}}) \text{ nm/Au } (t_{\text{Au}}) \text{ nm}]_{20}$ multilayer films are presented, where t_{Co} and t_{Au} indicate the thickness of the Co and Au layers, respectively.

2.3.1 Magnetic Anisotropy from Magnetization Curves

In this section, magnetic anisotropy is studied using magnetization curves for the $[\text{Co } 1.0 \text{ nm}/\text{Au } 2.0 \text{ nm}]_{20}$ multilayers deposited at the normal incidence of evaporation (i.e., $\theta = 0$) and the oblique incidence of evaporation (i.e., $\theta \neq 0$). Only the results of the multilayers prepared at $\theta = 0$ and 45° are presented here. Magnetization curves were measured with the field, H , parallel (in plane) and perpendicular (in plane) to the direction of the easy axis at low applied fields ($-1 \text{ kOe} < H < 1 \text{ kOe}$).

2.3.1.1 Normal Incidence Evaporation

Figure 2-1 shows the $M - H$ loops for the $[\text{Co } 1.0 \text{ nm}/\text{Au } 2.0 \text{ nm}]_{20}$ isotropic multilayers deposited at $\theta = 0^\circ$ at low fields ($-1 \text{ kOe} < H < 1 \text{ kOe}$). The H field was applied along the parallel (in plane) and the perpendicular (in plane) to the direction of the easy axis. The magnetism of the multilayer is magnetically isotropic.

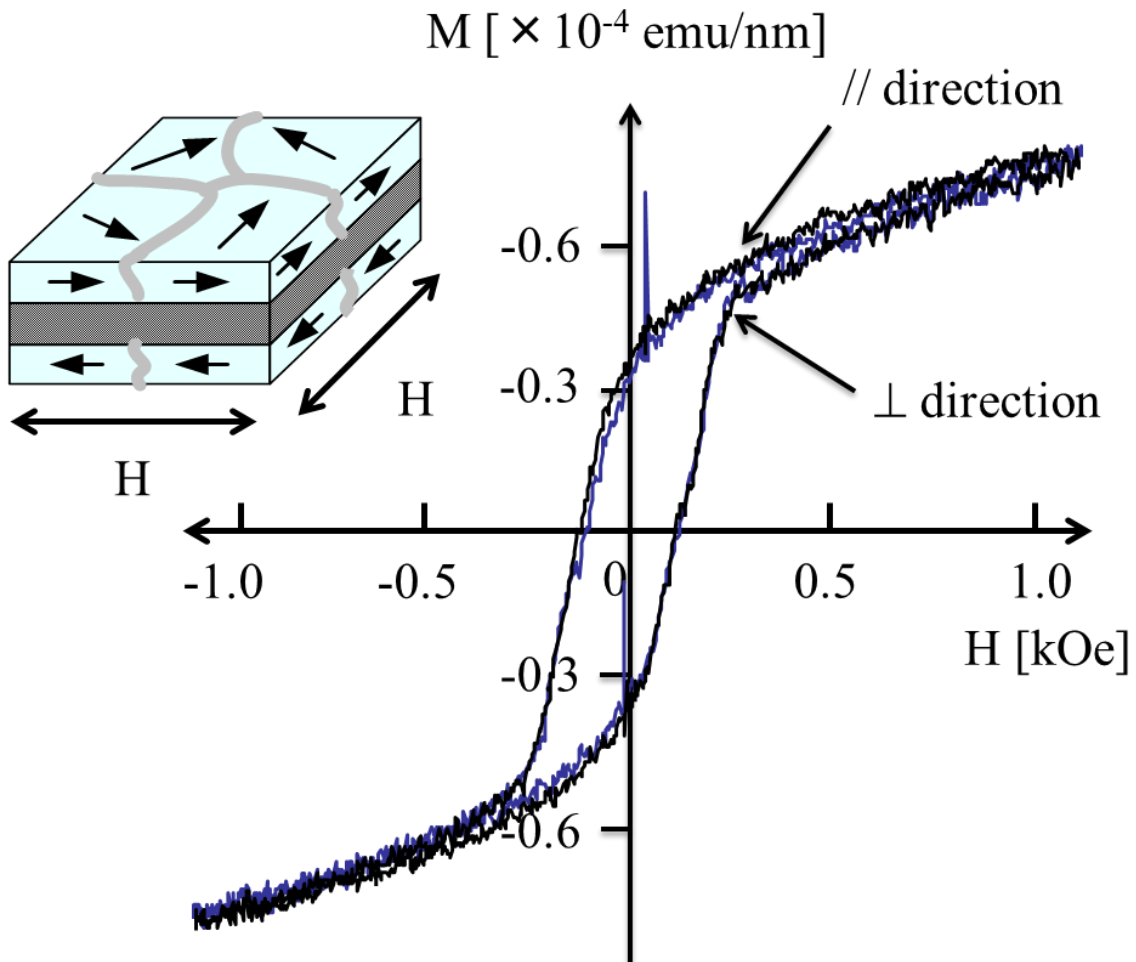


Figure 2-1 $M - H$ loops for the randomly oriented (isotropic) films. The notations // and \perp indicate the direction of the magnetic field along the parallel and the perpendicular to the easy axis, respectively.

2.3.1.2 Oblique Incidence Evaporation

Figure 2-2 shows the $M - H$ loops for the $[\text{Co } 1.0 \text{ nm}/\text{Au } 2.0 \text{ nm}]_{20}$ multilayers deposited at the oblique angle, $\theta = 45^\circ$ when the H field was applied parallel (in plane) and perpendicular (in plane) to the direction of the easy axis. The multilayer showed a remarkable magnetic anisotropy. The easy axis of magnetization was found along the perpendicular to the plane of oblique incidence of evaporation. The strong magnetic anisotropy, at low applied fields ($-1 \text{ kOe} < H < 1 \text{ kOe}$), is believed to be due to the preferential growth (also known as shadowing effect) of crystallites during evaporation [94] (see also Sections 1.6.1.1 and 1.6.1.2).

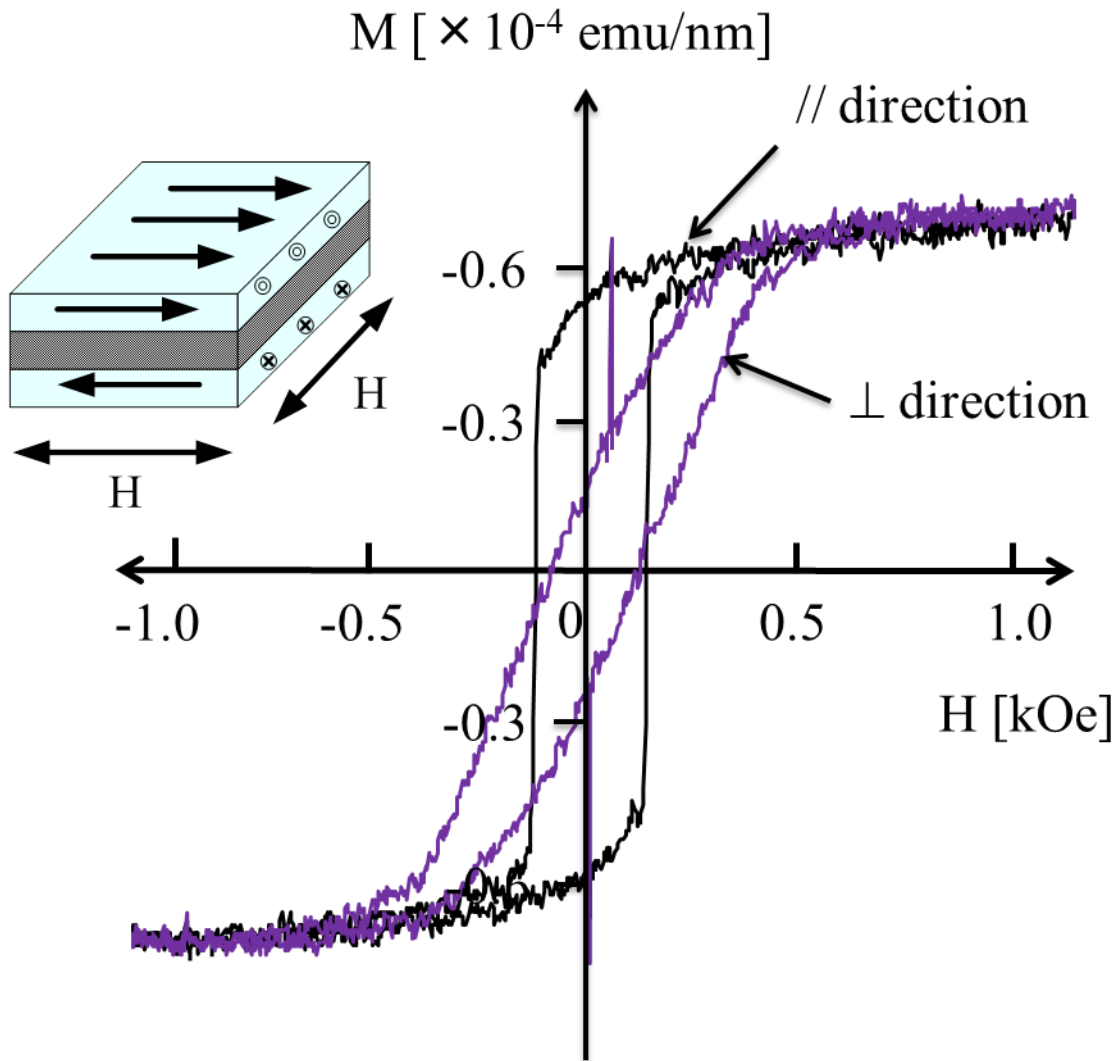


Figure 2-2 $M - H$ loops for the uniaxially oriented (anisotropic) multilayer films. The notations // and \perp indicate the direction of the magnetic field along the parallel and perpendicular to the easy axis, respectively.

2.3.2 Microstructural Analysis

Figure 2-3 shows a low angle X-ray diffraction (XRD) patterns for the $[\text{Co } 1.0 \text{ nm}/\text{Au } 2.0 \text{ nm}]_{20}$ multilayers. A broad peak was observed at the diffraction angle of 2.86° . The weaker intensity of the second peak was because the ratio of Co and Au is 1:2. It is clear that these multilayers have a well-defined periodicity, d , of 3 nm.

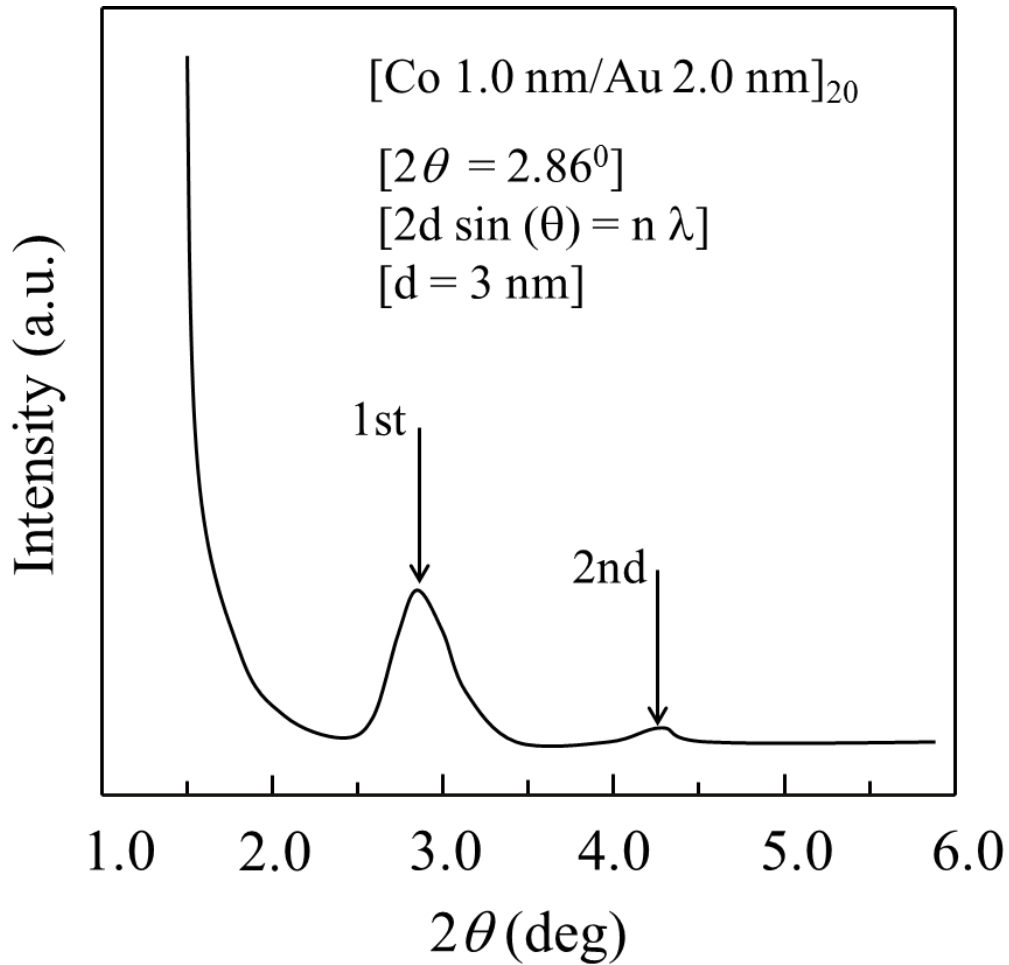


Figure 2-3 XRD patterns of $[\text{Co } 1.0 \text{ nm}/\text{Au } 2.0 \text{ nm}]_{20}$ multilayer.

2.3.3 Field Dependence of Magnetoresistance

The field dependence of the MR ratio was studied to relate the spin-dependent resistivity of the $[\text{Co } 1.0 \text{ nm}/\text{Au } 2.0 \text{ nm}]_{20}$ multilayers with the magnetic field. In the following sections, the field dependence of the MR ratio for the randomly oriented (isotropic) and uniaxially oriented (anisotropic) $[\text{Co } 1.0 \text{ nm}/\text{Au } 2.0 \text{ nm}]_{20}$ multilayer is discussed by considering the direction of the magnetic field and the direction of the current using six different measurement configurations (see Figure 1-24): two measurement configurations for the isotropic and four measurement configurations for the anisotropic multilayers.

2.3.3.1 Randomly Oriented Multilayers

Figure 2-4 shows the field dependence of the MR ratio for the randomly oriented [Co 1.0 nm/Au 2.0 nm]₂₀ multilayer when the magnetic field was applied parallel ($H // I$) and perpendicular to the current ($H \perp I$) at high fields ($-21 \text{ kOe} < H < +21 \text{ kOe}$)⁵. Two different MR contributions were detected for the [Co 1.0 nm/Au 2.0 nm]₂₀ multilayers: (1) isotropic and (2) anisotropic. The field dependence of the MR ratio observed for $H \perp I$ shows the larger value than the MR ratio observed for $H // I$. The AMR effect, shown in the upper part of Figure 2-4, was deduced from the difference between the GMR effects when the magnetic field was applied parallel and perpendicular to the current.

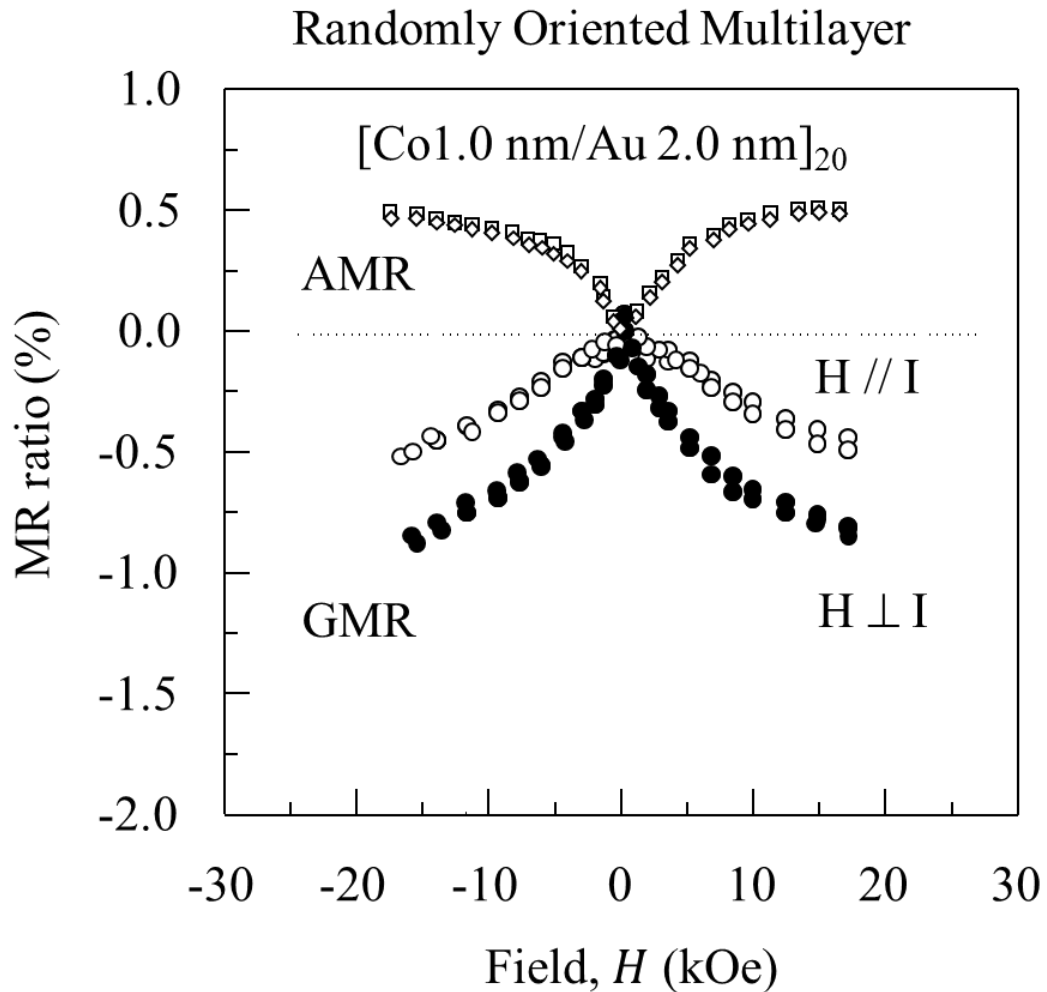


Figure 2-4 Field dependence of the MR ratio for the isotropic multilayer films. The notations // and \perp denote the direction of the applied field parallel and perpendicular to the current, respectively.

⁵ How the data were taken and analysed in this thesis is described in Appendix B.

2.3.3.2 Uniaxially Oriented Multilayers: Field Parallel to Easy Axis

Figure 2-5 shows the field dependence of the MR ratio for the uniaxially oriented [Co 1.0 nm/Au 2.0 nm]₂₀ multilayer when the magnetic field was applied parallel ($H // I_{e.a}$) and perpendicular ($H \perp I_{e.a}$) to the easy axis current at high fields ($-21 \text{ kOe} < H < +21 \text{ kOe}$). As in Section 2.3.3.1, two different MR contributions were detected for the anisotropic [Co 1.0 nm/Au 2.0 nm]₂₀ multilayers. The field dependence of the MR ratio observed for $H \perp I_{e.a}$ is larger than the field dependence of the MR ratio observed for $H // I_{e.a}$. In addition, the MR ratio of the anisotropic multilayer is almost twice than the MR ratio of the isotropic [Co 1.0 nm/Au 2.0 nm]₂₀ multilayers. The upper part in Figure 2-5 shows the AMR effect obtained from the difference between the MR ratio measured for $H \perp I_{e.a}$ and $H // I_{e.a}$.

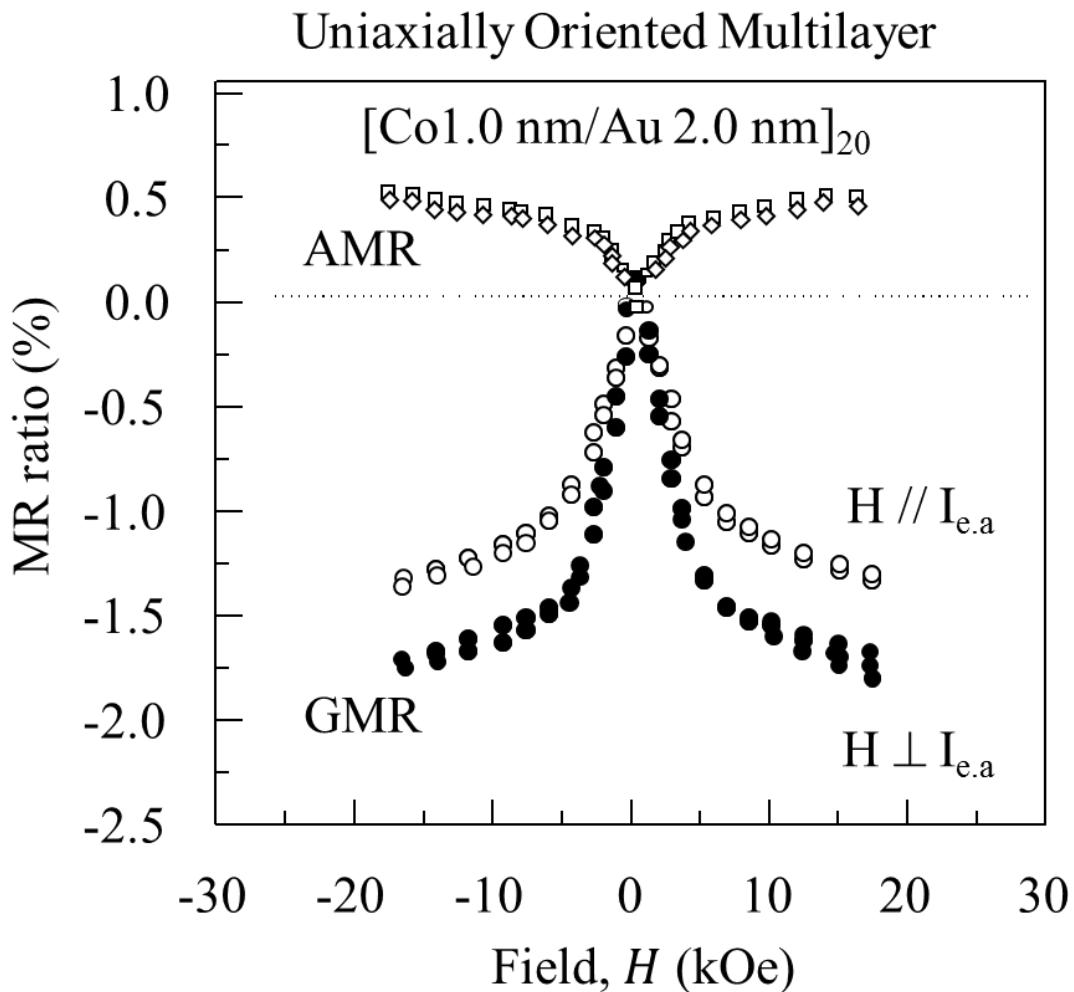


Figure 2-5 Field dependence of the MR ratio for the uniaxially oriented (anisotropic) multilayers. The notations // and \perp denote the direction of the applied field parallel and perpendicular to the easy axis current, respectively.

2.3.3.3 Uniaxially Oriented Multilayers: Field Parallel to Hard Axis

Figure 2-6 shows the field dependence of the MR ratio for the uniaxially oriented $[\text{Co } 1.0 \text{ nm}/\text{Au } 2.0 \text{ nm}]_{20}$ multilayer when the magnetic field was applied parallel ($H // I_{h.a.}$) and perpendicular ($H \perp I_{h.a.}$) to the hard axis current at high fields ($-21 \text{ kOe} < H < +21 \text{ kOe}$). As in Sections 2.3.3.1 and 2.3.3.2, two different MR contributions were detected for the anisotropic $[\text{Co } 1.0 \text{ nm}/\text{Au } 2.0 \text{ nm}]_{20}$ multilayers as well. The field dependence of the MR ratio observed for $H \perp I_{h.a.}$ is larger than the field dependence of the MR ratio observed for $H // I_{h.a.}$. In addition, the overall MR ratio is larger than the MR ratio of both the isotropic and the anisotropic $[\text{Co } 1.0 \text{ nm}/\text{Au } 2.0 \text{ nm}]_{20}$ multilayers presented in Sections 2.3.3.1 and 2.3.3.2. The upper part in Figure 2-6 shows the anisotropic components of the MR ratio.

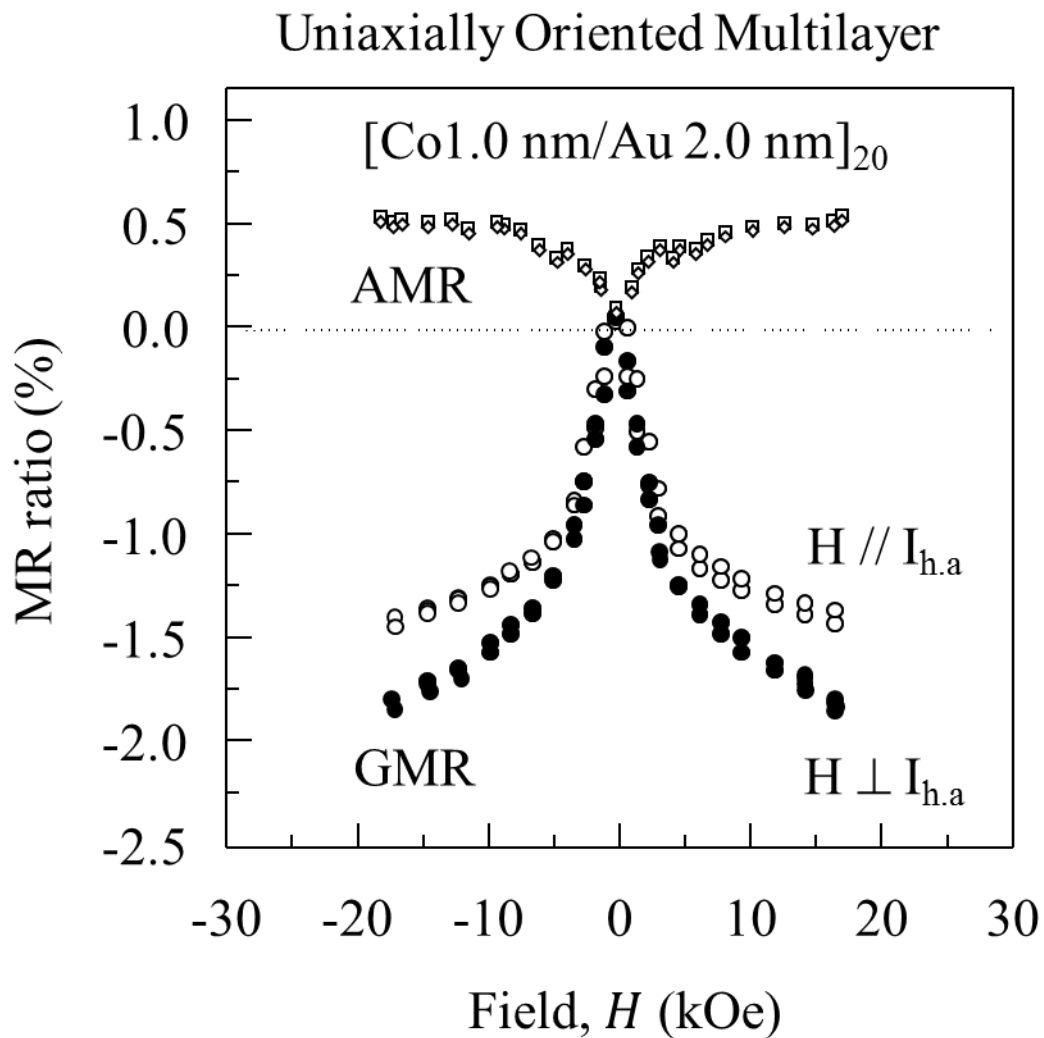


Figure 2-6 Field dependence of the MR ratio for the uniaxially oriented multilayers. The notations // and \perp denote the direction of the applied field parallel and perpendicular to the hard axis current, respectively.

2.3.4 Nonmagnetic Layer Thickness Dependence of the MR Ratio

Figure 2-7 shows the Au layer thickness dependence of the MR ratio for the $[\text{Co } 1.0 \text{ nm}/\text{Au } (t_{\text{Au}}) \text{ nm}]_{20}$ multilayer at high fields ($-21 \text{ kOe} < H < 21 \text{ kOe}$), where t_{Au} denotes the thickness of the Au layer. The MR ratio of the isotropic multilayers shows the average of two data {denoted by open circles (o)} measured by changing the direction of the current when the magnetic field was applied along the easy and hard axes. Similarly, the MR ratio of the anisotropic multilayers shows the average of the two data {denoted by closed circles (•)} measured by changing the direction of the current and the applied magnetic field along the magnetic easy and hard axes. The MR ratio of both the isotropic and anisotropic multilayers shows a maximum at $t_{\text{Au}} = 2.0 \text{ nm}$. Interestingly, the overall MR ratio for the anisotropic $[\text{Co } 1.0 \text{ nm}/\text{Au } (t_{\text{Au}}) \text{ nm}]_{20}$ multilayers is larger than the overall MR ratio for the isotropic $[\text{Co } 1.0 \text{ nm}/\text{Au } (t_{\text{Au}}) \text{ nm}]_{20}$ multilayers.

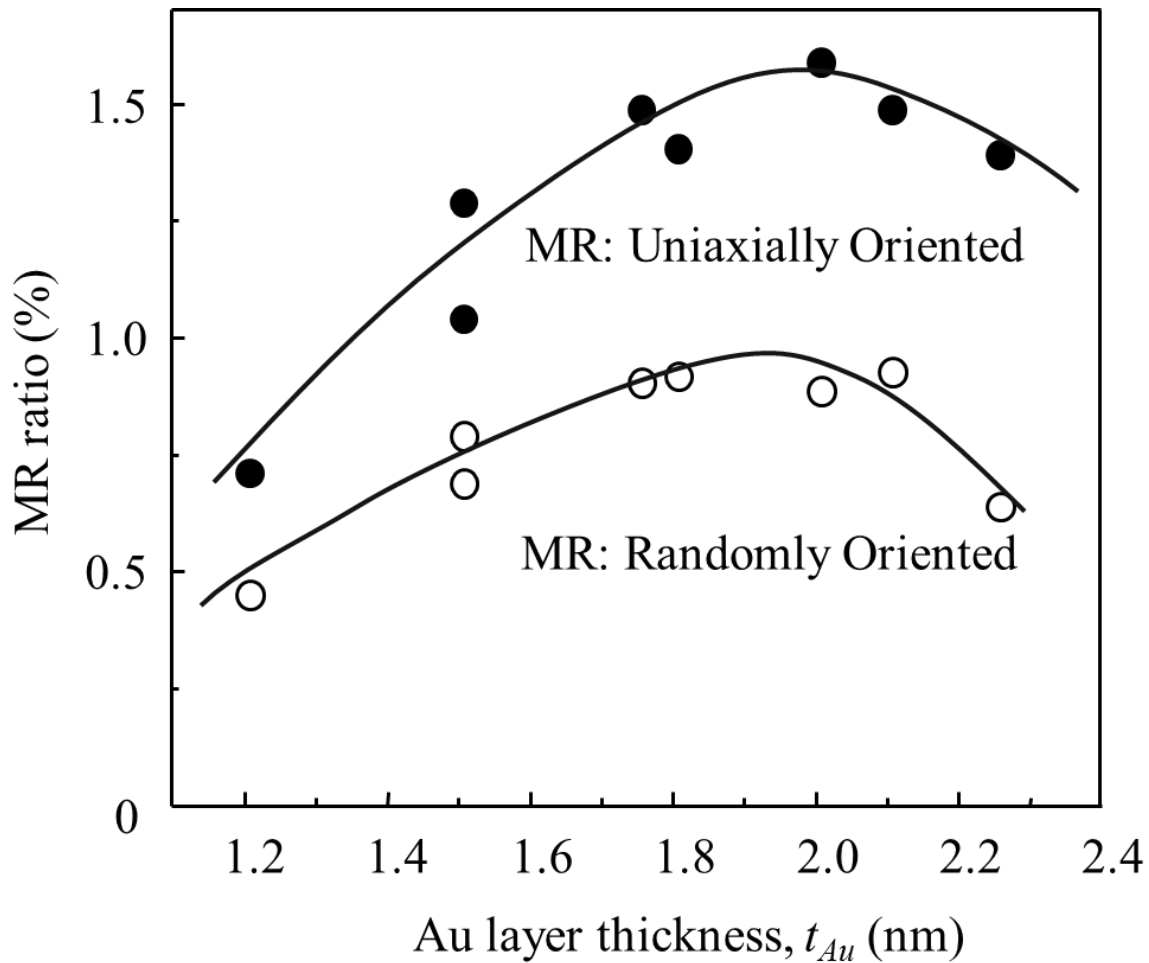


Figure 2-7 The MR ratio of the randomly oriented (isotropic) and uniaxially oriented (anisotropic) $[\text{Co } 1.0 \text{ nm}/\text{Au } (t_{\text{Au}}) \text{ nm}]_{20}$ multilayers at various Au layer thicknesses. Each point in the graph represents the average of two data.

2.3.5 Magnetic Layer Thickness Dependence of the MR Ratio

In Section 2.3.4, we studied the MR effect at various Au layer thicknesses. In this section, in addition to the various Au layer thicknesses, the same will be studied at various Co layer thicknesses, in order to study the effect of ferromagnetic layer thickness on the MR ratio.

Figure 2-8 shows the plots of the MR ratio for the $[\text{Co}(t_{\text{Co}}) \text{ nm}/\text{Au}(t_{\text{Au}}) \text{ nm}]_N$ anisotropic multilayers as the thicknesses of Co and Au layers are changed. The subscript N outside the parenthesis denotes the stacking number. It shows the MR effect when the applied field, H is (a) parallel ($H // I$) and (b) perpendicular ($H \perp I$) to the current, I . Each point in Figure 2-8 represents an average of two measurements. The Co and Au layer thicknesses were changed from 0 to 2 nm and 0 to 4 nm, respectively.

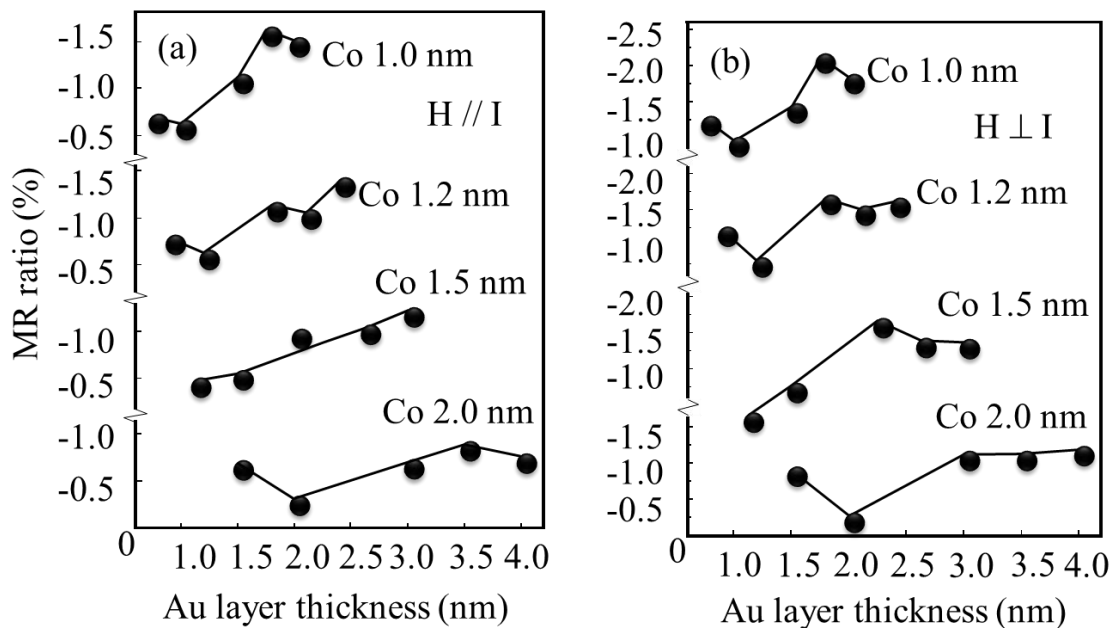


Figure 2-8 The MR ratio versus Au layer thickness at various Co layer thicknesses.

The MR ratio in Figure 2-8 (a) and (b) increases with the Au layer thickness and reaches peak at 2 nm for a Co layer thickness of 1 nm. This behavior is consistent with the results reported in Section 2.3.4. As the Co layer thickness is increased from 1 to 2 nm, the peaks of the MR ratios are shifted towards the higher Au layer thicknesses. However, the overall MR ratio is decreased with increasing Co layer thickness.

The decrease in the MR ratio with the increase in the Co layer thickness seems to be due to the increase in the ferromagnetic regions not showing optimum antiparallel alignment of the spins when the ferromagnetic layer thickness is increased over 1 nm. Similarly, the decrease in the MR ratio with the increase in the Au layer thickness seems to be due to the reduction in the magnetic coupling strength between the adjacent magnetic moments [116]. The MR ratio of the $[\text{Co}(t_{\text{Co}}) \text{ nm}/\text{Au}(t_{\text{Au}}) \text{ nm}]_N$ multilayer when the field was applied

perpendicular to the current ($H \perp I$) was always larger than when the field was applied parallel to the current ($H \parallel I$).

2.3.6 Magnetic Anisotropy and the MR Ratio

In Sections 2.3.3 through 2.3.5, we reported MR effects of the isotropic and anisotropic $[\text{Co} (t_{\text{Co}}) \text{ nm}/\text{Au} (t_{\text{Au}}) \text{ nm}]_N$ multilayers. The MR ratio of anisotropic $[\text{Co} (t_{\text{Co}}) \text{ nm}/\text{Au} (t_{\text{Au}}) \text{ nm}]_{20}$ multilayer was always found to be larger than the MR ratio of the isotropic $[\text{Co} (t_{\text{Co}}) \text{ nm}/\text{Au} (t_{\text{Au}}) \text{ nm}]_{20}$ multilayers. In this section, we describe the relationship between the MR ratio and the anisotropy constant for the magnetically annealed $[\text{Co} 1.0 \text{ nm}/\text{Au} 2.0 \text{ nm}]_{20}$ multilayers.

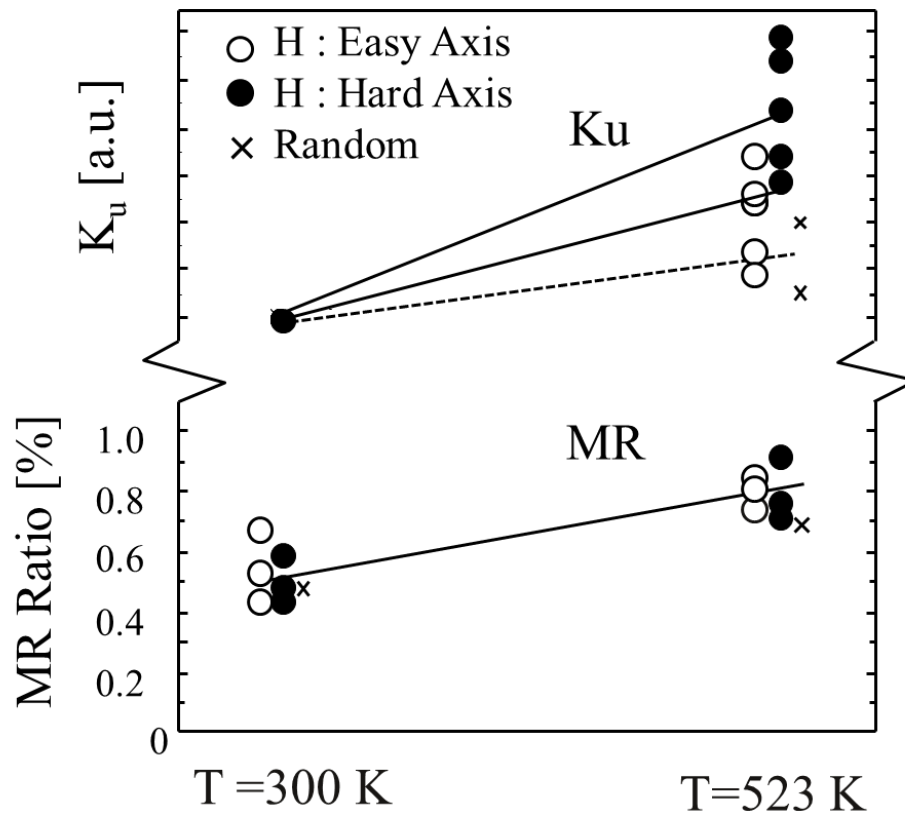


Figure 2-9 The MR ratio and K_u versus annealing temperature: open circles (o): $H \parallel I$ and closed circles: (●) $H \perp I$ for uniaxially oriented multilayers, and cross (x): $H \parallel I$ or $H \perp I$ for randomly oriented multilayers.

Figure 2-9 shows the MR ratio and the magnetic anisotropy constant, K_u , at two different temperatures: (1) room temperature (i.e., 300 K) and (2) elevated temperature (i.e., 523 K). The lower part shows the MR ratio and the upper part shows K_u as the temperature was changed from 300 to 523 K. The MR ratio increases owing to the increase in magnetic annealing [119]. Similarly, K_u increases with the increase of temperature. Therefore,

the increase of MR for [Co 1.0 nm/Au 2.0 nm]₂₀ multilayer is directly related to K_u . The overall MR of the uniaxially oriented multilayers {indicted by (●,o) signs} is larger than the overall MR of the randomly oriented multilayers {indicated by cross (×) signs}. This result explains why in Sections 2.3.3 through 2.3.5, the MR effect of the uniaxially oriented [Co 1.0 nm/Au 2.0 nm]₂₀ multilayers was larger than the MR effect of the randomly oriented [Co 1.0 nm/Au 2.0 nm]₂₀ multilayers.

2.4 Summary

Magnetic anisotropy was induced using oblique angle deposition. The MR ratio was studied by changing both the non-magnetic and magnetic layer thicknesses. The study of non-magnetic layer thickness dependence of the MR ratio showed a maximum MR ratio of 1.6 % at room temperature. The maximum MR ratio of the multilayer shifted towards the higher ferromagnetic layer thicknesses. The result suggested a decrease in the antiferromagnetically aligned moments on either side of the nonmagnetic layers as the ferromagnetic layer thickness was increased. Interestingly, the MR effect of the uniaxially oriented multilayers was found to be larger than that of the randomly oriented multilayers for all layer thicknesses. A low angle diffraction analysis revealed a well-defined periodicity of the Co/Au multilayers prepared in this thesis.

The effect of magnetic annealing on the MR ratio and magnetic anisotropy was also studied. The magnetic annealing enhanced both magnetic anisotropy and the MR ratio meaning that the increase in the MR ratio was directly related to the orientation characteristics of magnetic moments in these multilayers. The observed value of the coercive force was in a very small range (< 50 Oe) at ambient conditions, indicating that these multilayers are possible candidates for the sensor applications.

Chapter 3: Magnetoresistance Effect and Magnetic Properties of Co/Ag Multilayers⁶

3.1 Introduction

In Chapter 2, we presented structural, MR, and magnetic anisotropy properties of the isotropic and anisotropic Co/Au multilayers, specially grown using oblique incidence evaporation for various Co and Au layer thicknesses. Similar to the lattice mismatch between Co and Au, the lattice mismatch between Co and Ag is also 15 %. Therefore, it will be interesting to study Co/Ag multilayers for a better understanding of the growth method on GMR and magnetic anisotropy [68], [120]. In this chapter, we present MR and magnetic properties of the isotropic and anisotropic Co/Ag multilayers, prepared using pulsed-current deposition, for various Co layer thicknesses and strains.

Pulsed-current deposition is one of the useful methods for growing materials on the atomic levels using a single electrolyte at room temperature. Although finding a suitable deposition condition is difficult, it is proved to be a promising method for producing magnetic multilayers and alloys by controlling the deposition parameters. In this work, Co/Ag multilayers are grown using pulsed-current deposition method.

Figure 3-1 shows a typical pulsed-current waveform where, J is the current density (A/m^2), t is the deposition time (ms), T_A is the *on* time, during which the current is applied, and T_B is the *off* time, during which no current is applied. Similarly, J_A is the *on* time current density, J_B is the *off* time current density, and J_{avg} is the average current density. By controlling the deposition time and the amplitude of the current density multilayers of two or more elements with various compositions and thicknesses can be prepared.

⁶ A version of this chapter has been published. Sections 3.3.1 through 3.3.5 are reprinted from [4] with permission. © 2009 IEEE. Rizal, C. and Ueda, Y. Magnetoresistance and magnetic anisotropy properties of strain-induced Co/Ag multilayers. *IEEE Transactions on Magnetics*. 6/2009. Sections 3.3.6 through 3.3.11 are reprinted from [68] with permission. © 2011, IEEE. Rizal, C., Gyawali, P., Kshatry, I. B., and Pokharel, R. K. Effect of strain on magnetoresistance and magnetic properties of Co(t_c)/Ag nanostructures. *IEEE Nanotechnology Materials and Devices Conference*. 10/2011.

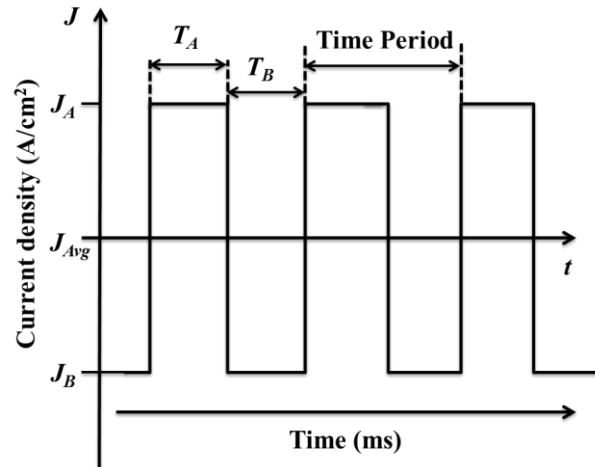


Figure 3-1 Typical pulsed-current waveform.

Figure 3-2(a) shows a schematic of the pulsed-current deposition where the x -axis is the electrode potential (corresponding to the current density) and the y -axis is the deposition time, and corresponds to the amount of deposited material in the film. The principle of pulsed-current deposition is as follows: at potential V_A , metal A deposits whereas at potential V_{A+B} , an alloy of metal A and metal B deposits. By changing the current (potential) alternately between these values, any combinations of multilayers, composition modulated alloys, and nanoparticles can be developed [121]. Further details on the pulsed-current deposition of magnetic nanostructures are available in [46]⁷.

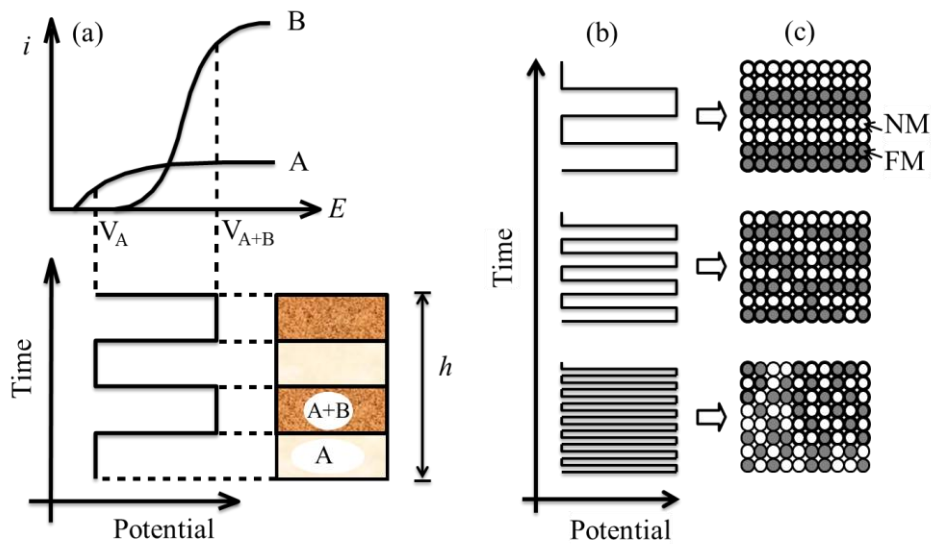


Figure 3-2(a) Diagram showing the principle of pulsed-current deposition, (b) deposition time versus potential corresponding to the pulsed-current, and (c) film structures corresponding to (b).

⁷ This paper reports author's previous work, not included in this thesis.

Figure 3-2(b) shows a pulsed-current wave form with different width and interval time and (c) shows the corresponding multilayer structures. The composition of each layer of ferromagnetic (*FM*) and nonmagnetic (*NM*) materials in (c) corresponds to the pulse height whereas the thickness corresponds to the pulse width, which is also a deposition time. The beauty of this process is that by controlling the pulse amplitude and the pulsed width one can produce various combinations of multilayers and alloys on an atomic scale from a single electrolyte. The possibility of simultaneously co-depositing different materials, which are normally immiscible, from an aqueous solution is the main characteristic of the pulsed-current deposition.

It is believed that the magnetic anisotropy of the ferromagnetic layers depends on the values of strain and lattice mismatches between the adjacent layers. In this chapter, experimental results of the GMR effect and magnetic anisotropy properties of the as-deposited and the strained ferromagnetic Co layers in the Co/Ag multilayer are presented.

3.2 Experimental Procedure

Co/Ag multilayer films were grown by means of pulsed-current deposition. Figure 3-3 shows a schematic for the generation of pulsed-current used in this study. It consists of four major parts: (a) a microcomputer, (b) a *D-A* converter, (c) a regulator, and (d) an electrolyte. A digital signal is fed through the programmable microcomputer to *D-A* converter. The outgoing analog signal is then fed to the regulator (a constant-current circuit). The output from the regulator is fed to the electrochemical cell, which consists of a single electrolyte containing two or more elements.

The electrolyte was prepared with 99.9 % pure chemicals in doubly distilled water and pH was adjusted to 3.0. The electrolyte consisted of $\text{CoSO}_4 \cdot 7\text{H}_2\text{O}$, AgI, and KI with a silver anode. In the plating bath, the Co concentration was changed while keeping the Ag concentration constant, whereas the ratio between Co and Ag was varied. The substrates consisted of 15-nm thin copper buffer layer vapor deposited on the polyimide film. The pulsed-current density was switched from 0.1 to 10 mA/cm². The deposition time was changed from 0.1 milliseconds to several seconds.

The nominal thickness of the deposited film was obtained using Faraday's laws as:

$$h = \frac{A_w}{n \times F \times \delta \times S} \int i \times \partial t = \frac{A_w \times I \times t}{n \times F \times \delta \times S}, \quad (3.1)$$

where h is the film thickness, t is the deposition time, A_w is the atomic weight of the material, δ is the density of the deposited material, S is the surface area of the deposit, n is the valency of the material, and F is the Faraday's constant, which is 96500 *C*. The composition of the deposited film was determined using flame emission and atomic absorption spectroscopy and energy dispersive X-ray analysis. The composition of the single ferromagnetic layer was 92 *at. %* Co 8 *at. %* Ag. The layer thickness was determined from the mass of the deposited film assuming the density of the film same as the density of the bulk material. Magnetization curves were measured using vibrating sample magnetometer (*VSM*) and torque magnetometer.

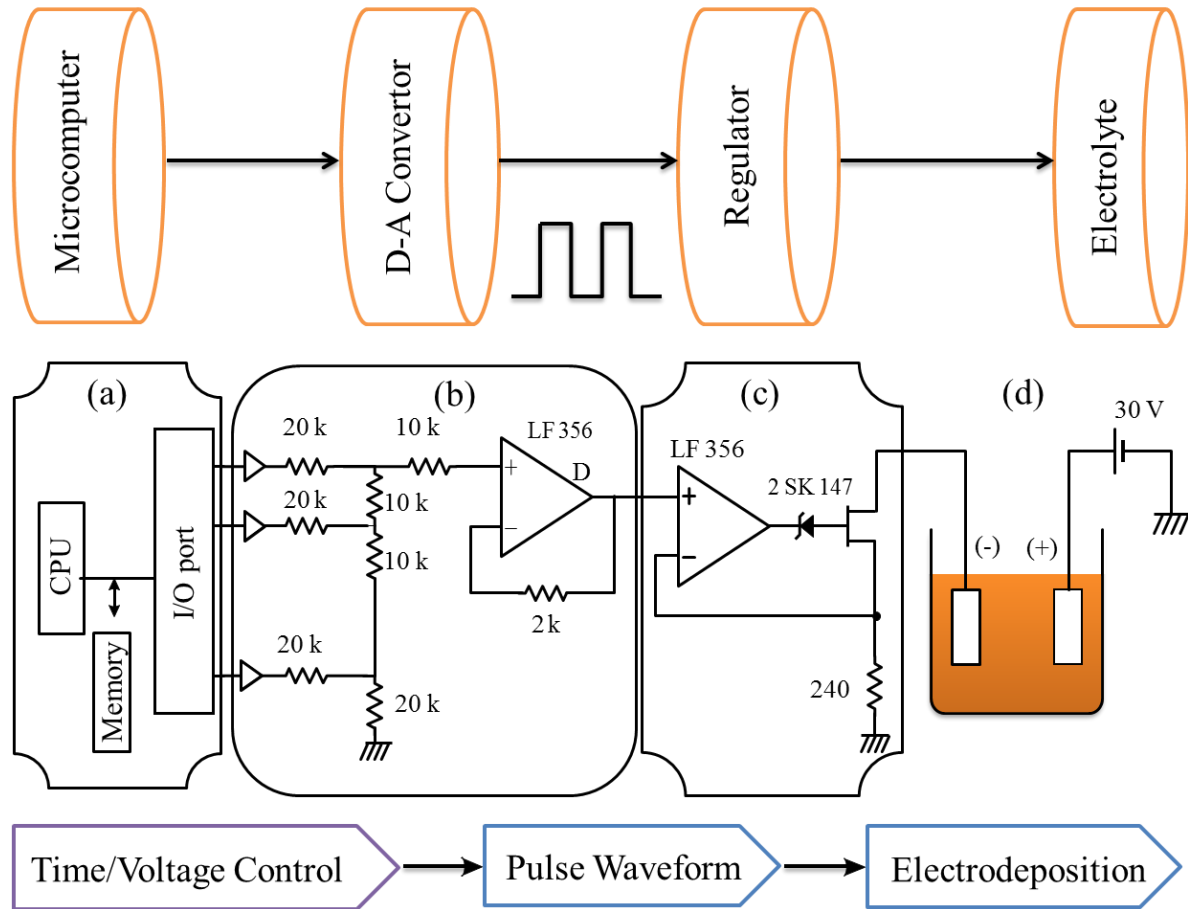


Figure 3-3 Schematic of pulsed-current deposition [122].

The strain was induced mechanically by stretching the polyimide and its value was measured using a strain gauge. The electrical resistance of the multilayers was measured using the four-point probe method at room temperature with the applied magnetic field always in plane of the multilayers. In order to determine the anisotropic and isotropic components of the MR effect, the resistance was measured in all six configurations. The details of these measurement methods are given in page 36, Section 1.8.2.4. The magnetic field dependence of the MR ratio was examined by varying the relative direction between the magnetic field, H and the current, I .

3.3 Results and Discussions

In this section, magnetic anisotropy and the MR effects are studied extensively using magnetization curves for the randomly oriented, i.e., as-deposited ($\varepsilon = 0$) and strain-induced ($\varepsilon \neq 0$) $[\text{Co} (t_{\text{Co}}) \text{ nm}/\text{Ag} 1.5 \text{ nm}]_N$ multilayer films at low magnetic fields (< 1 kOe). The notations t_{Co} and N indicate the Co layer thickness and number of bilayers in the film, respectively. Magnetic anisotropy is also studied using torque curves. The effect of strain on the magnetization at various Co layer thicknesses is studied. The MR effect is studied by changing the ferromagnetic Co layer thickness at a constant Ag layer thickness of 1.5 nm. The field dependence of the MR ratio is studied at both low (< 1 kOe) and high (< 21 kOe) magnetic fields.

3.3.1 Magnetic Anisotropy from Magnetization Curves

In this section, magnetic anisotropy is studied using magnetization curves for the randomly oriented (i.e., $\varepsilon = 0$) and the uniaxially oriented (i.e., $\varepsilon \neq 0$) [Co 1.5 nm/Ag 1.5 nm]₂₀ multilayer films at the applied field, H , of ± 1 kOe.

3.3.1.1 Randomly Oriented Multilayers

Figure 3-4 shows the $M - H$ curves for the as-deposited [Co 1.5 nm/Ag 1.5 nm]₂₀ multilayer. Magnetization curves were measured in two directions, along the parallel (in plane) and perpendicular (in plane) to the multilayer, at room temperature. The result shows that the magnetism of the as-deposited [Co 1.5 nm/Ag 1.5 nm]₂₀ multilayer is magnetically isotropic.

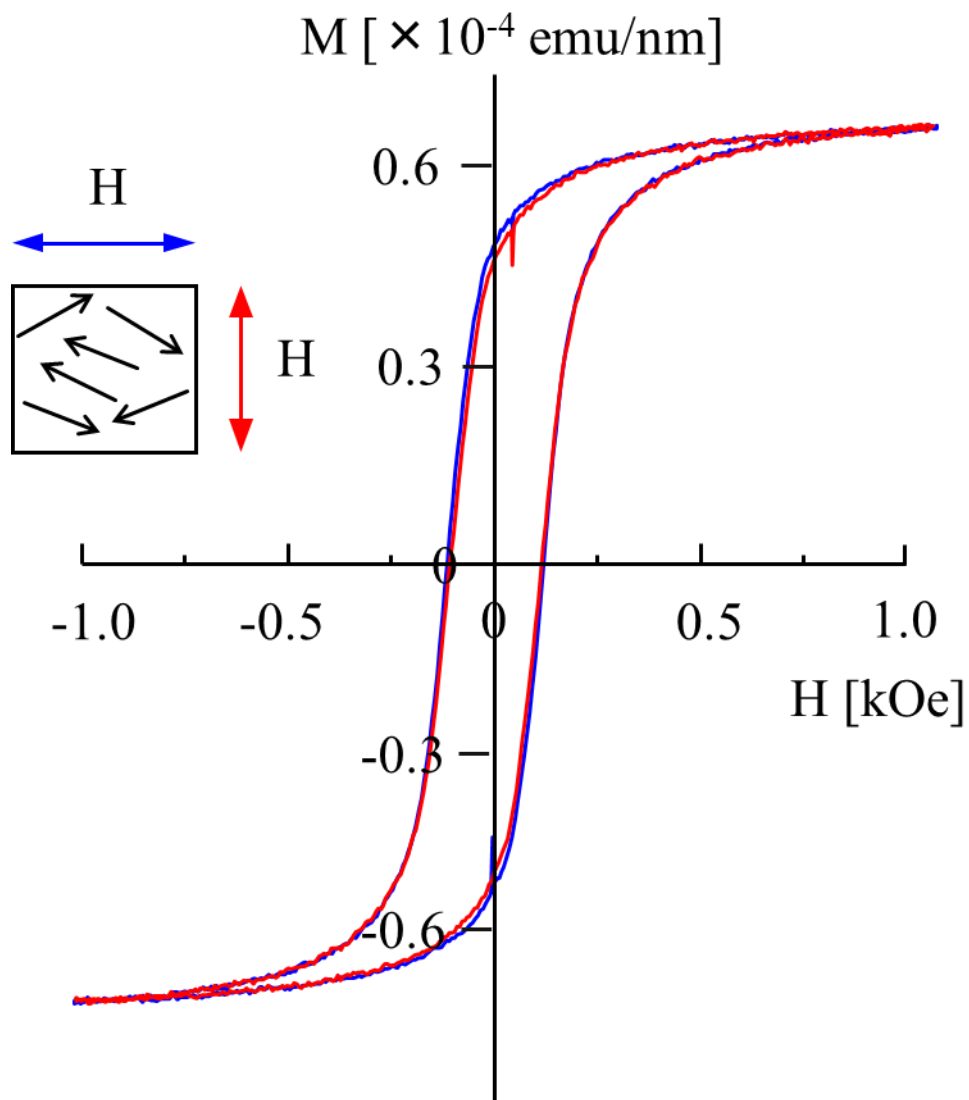


Figure 3-4 $M - H$ hysteresis loops for the randomly oriented, i.e., as-deposited ($\varepsilon = 0$) [Co 1.5 nm / Ag 1.5 nm]₂₀ multilayer.

3.3.1.2 Uniaxially Oriented Multilayers

Figure 3-5 shows the $M - H$ curves for the strain-induced $[\text{Co } 1.5 \text{ nm}/\text{Ag } 1.5 \text{ nm}]_{20}$ multilayer. Magnetization curves were measured parallel (hard axis) and perpendicular (easy axis) to the direction of strain at room temperature. The result shows that the magnetism of the strain-induced $[\text{Co } 1.5 \text{ nm}/\text{Ag } 1.5 \text{ nm}]_{20}$ multilayer is magnetically anisotropic, i.e., multilayers show uniaxial magnetic anisotropy. The orientation of the induced easy axis is found to be perpendicular to the direction of strain.

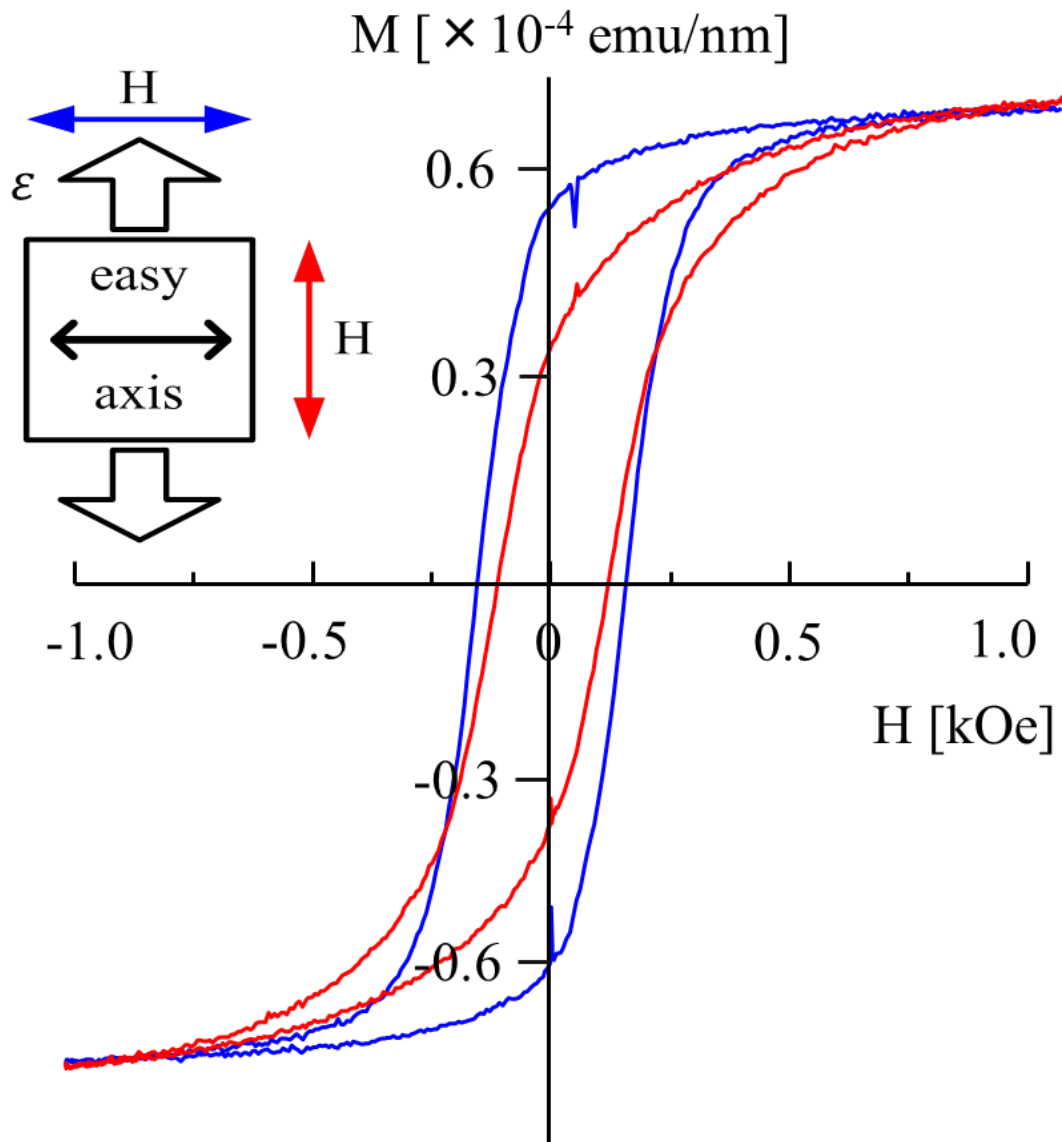


Figure 3-5 $M - H$ hysteresis loops for the uniaxially oriented, i.e., strain-induced ($\epsilon = 1.5 \%$) $[\text{Co } 1.5 \text{ nm} / \text{Ag } 1.5 \text{ nm}]_{20}$ multilayer.

3.3.2 Field Dependence of the MR Ratio in Low Fields

In this section, the relationships between the field dependence of the MR ratio and the magnetization curves for the randomly oriented (isotropic) and uniaxially oriented (anisotropic) [Co 1.5 nm/Ag 1.5 nm]₂₀ multilayer films are discussed. At low magnetic fields, the field dependence of the MR ratio does not significantly depend on the direction of the measuring current, but it only has a tendency to depend on the direction of the applied field.

3.3.2.1 Randomly Oriented Multilayers

Figure 3-6 shows the field dependence of the MR ratio and the corresponding magnetization curve for the isotropic [Co 1.5 nm/Ag 1.5 nm]₂₀ multilayer films. In the weak magnetic fields ($-1 \text{ kOe} < H < 1 \text{ kOe}$), the difference for the field dependence of the MR ratio is clearly observed depending on the orientation of the magnetization curve, i.e., the field dependence of the MR ratio is corresponding to the shape of the magnetization curve⁸.

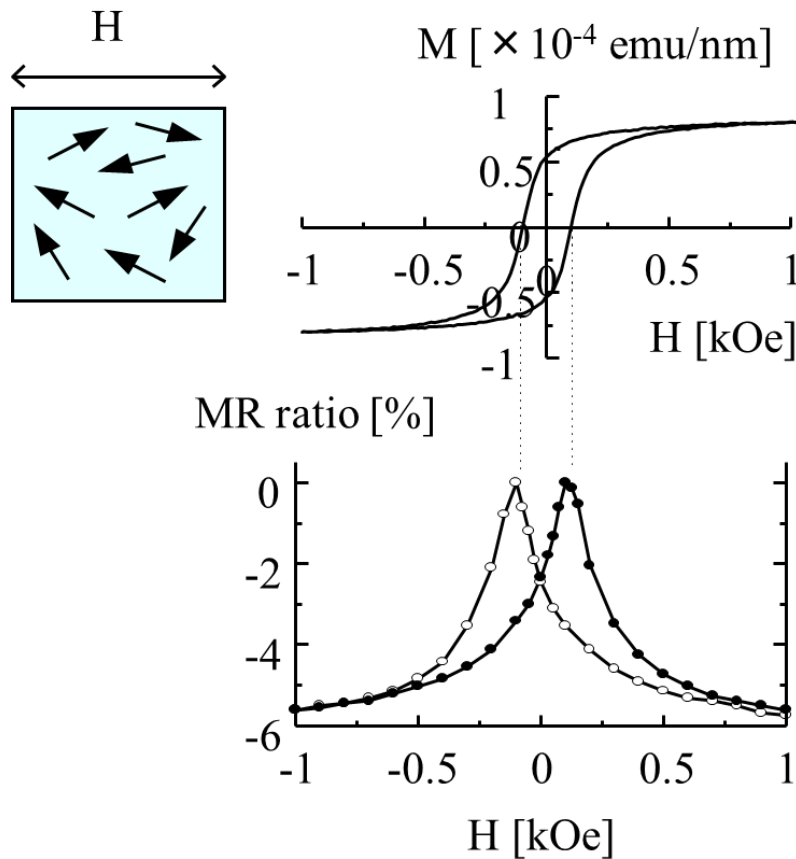


Figure 3-6 Field dependence of the MR ratio and the corresponding magnetization curve for the randomly oriented ($\epsilon = 0 \%$) [Co 1.5 nm /Ag 1.5 nm]₂₀ multilayer.

⁸ How the data were taken and analysed in this thesis is described in Appendix B.

3.3.2.2 Uniaxially Oriented Multilayers: Current Parallel to Easy Axis

Figure 3-7 shows the magnetic field dependence of the MR ratio and the corresponding magnetization curve for the anisotropic [Co 1.5 nm/Ag 1.5 nm]₂₀ multilayer films when the magnetic field was applied parallel to the easy axis. Similar to the characteristics shown by the isotropic multilayer in Section 3.3.2.1, in the weak magnetic fields ($-1 \text{ kOe} < H < 1 \text{ kOe}$), the difference for the magnetic field dependence of the MR ratio is clearly observed, and it depends on the orientation of magnetization, i.e., the field dependence of the MR ratio is corresponding to the shape of the magnetization curve. However, the magnitude of the MR effect of the anisotropic multilayer is smaller than the magnitude of the MR effect of the isotropic multilayer.

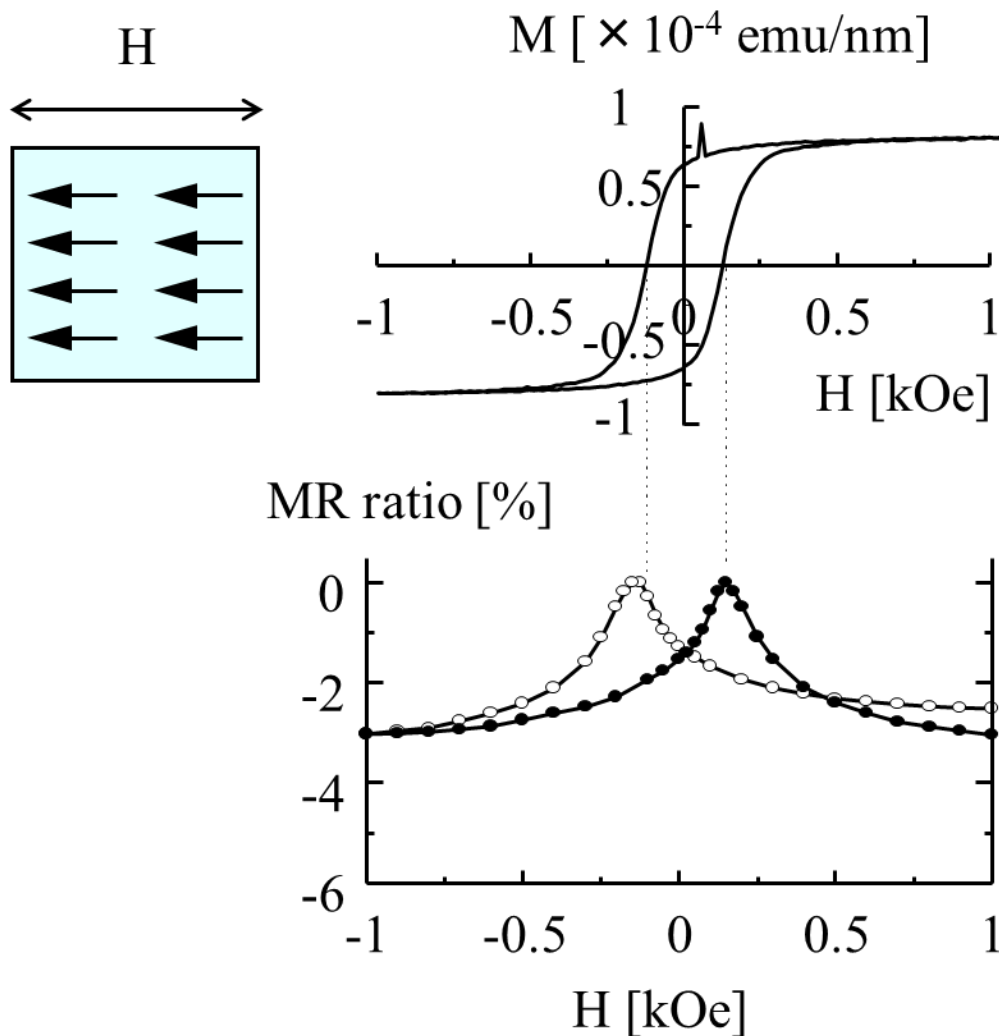


Figure 3-7 Field dependence of the MR ratio and the corresponding magnetization curve for the uniaxially oriented ($\epsilon = 1.5 \%$) [Co 1.5 nm/Ag 1.5 nm]₂₀ multilayer, when the magnetic field was applied parallel to the easy axis.

3.3.2.3 Uniaxially Oriented Multilayers: Current Parallel to Hard Axis

Figure 3-8 shows the magnetic field dependence of the MR ratio and the corresponding magnetization curve for the uniaxially oriented (anisotropic) $[\text{Co } 1.5 \text{ nm}/\text{Ag } 1.5 \text{ nm}]_{20}$ multilayer film when the magnetic field was applied perpendicular to the easy axis. Similar to the characteristics shown by the isotropic (in Section 3.3.2.1) and anisotropic (in Section 3.3.2.2) multilayers, the difference for the field dependence of the MR ratio in Figure 3-8 is clearly observed, i.e., the field dependence of the MR ratio is corresponding to the shape of the magnetization curve at low magnetic fields ($-1 \text{ kOe} < H < 1 \text{ kOe}$). Although the MR ratio for the anisotropic multilayer is smaller than the MR ratio for the isotropic multilayer presented in Section 3.3.2.1, the MR ratio when the current is parallel to the hard axis (see Figure 3-8) is always larger than the MR ratio when the current is parallel to the easy axis (see Figure 3-7).

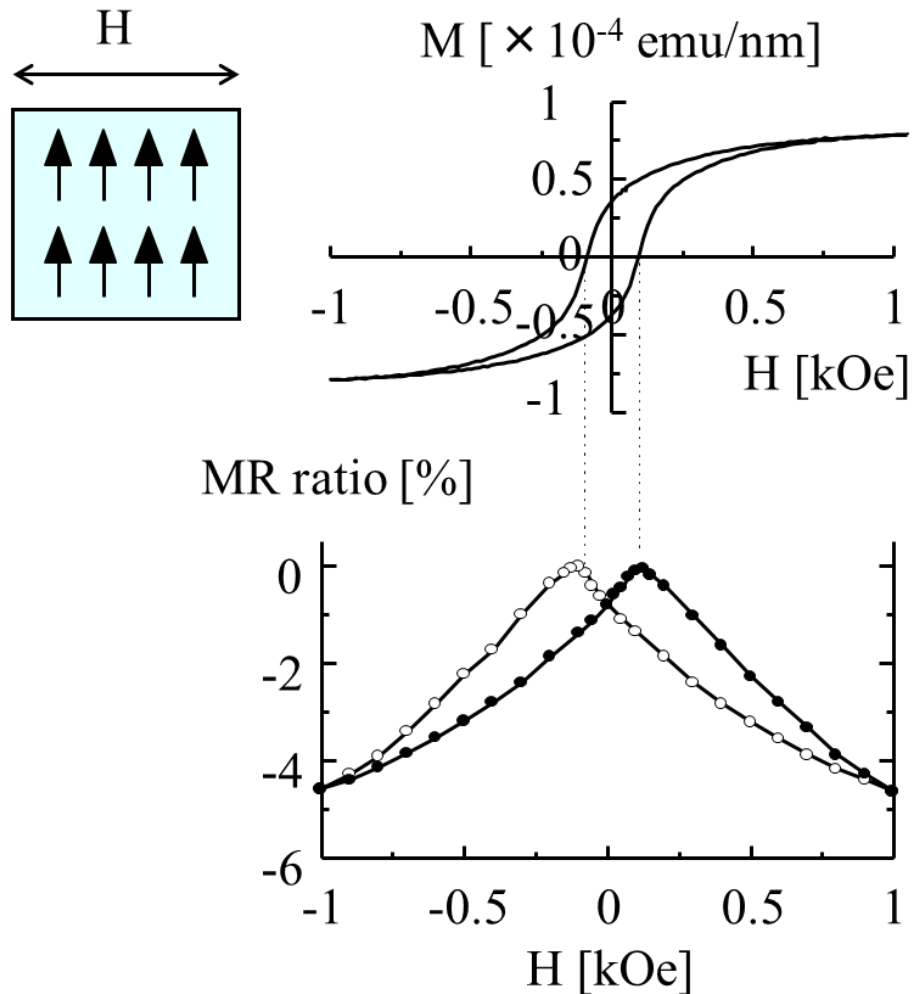


Figure 3-8 Field dependence of the MR ratio and the corresponding magnetization curve for the uniaxially oriented ($\epsilon = 1.5 \%$) $[\text{Co } 1.5 \text{ nm}/\text{Ag } 1.5 \text{ nm}]_{20}$ multilayer, when the magnetic field was applied perpendicular to the easy axis.

3.3.3 Cobalt Layer Thickness and the GMR Effect

Figure 3-9 shows the Co layer thickness dependence of the MR ratio for both the isotropic and anisotropic $[\text{Co}(t_{\text{Co}}) \text{ nm}/\text{Ag} 1.5 \text{ nm}]_N$ multilayers. The notations t_{Co} and N indicate the Co layer thickness and the number of bilayers in the film, respectively. The thickness of the Ag layer was fixed at 1.5 nm. The MR ratio increases continuously with the increase of the Co layer thickness and reaches maximum at a Co layer thickness, $t_{\text{Co}} = 1.5$ nm. The MR ratio starts to decrease with further increase of the Co layer thickness. The MR ratio for both the isotropic and anisotropic $[\text{Co}(t_{\text{Co}}) \text{ nm}/\text{Ag} 1.5 \text{ nm}]_N$ multilayers shows a maximum at the same Ag layer thickness of 1.5 nm.

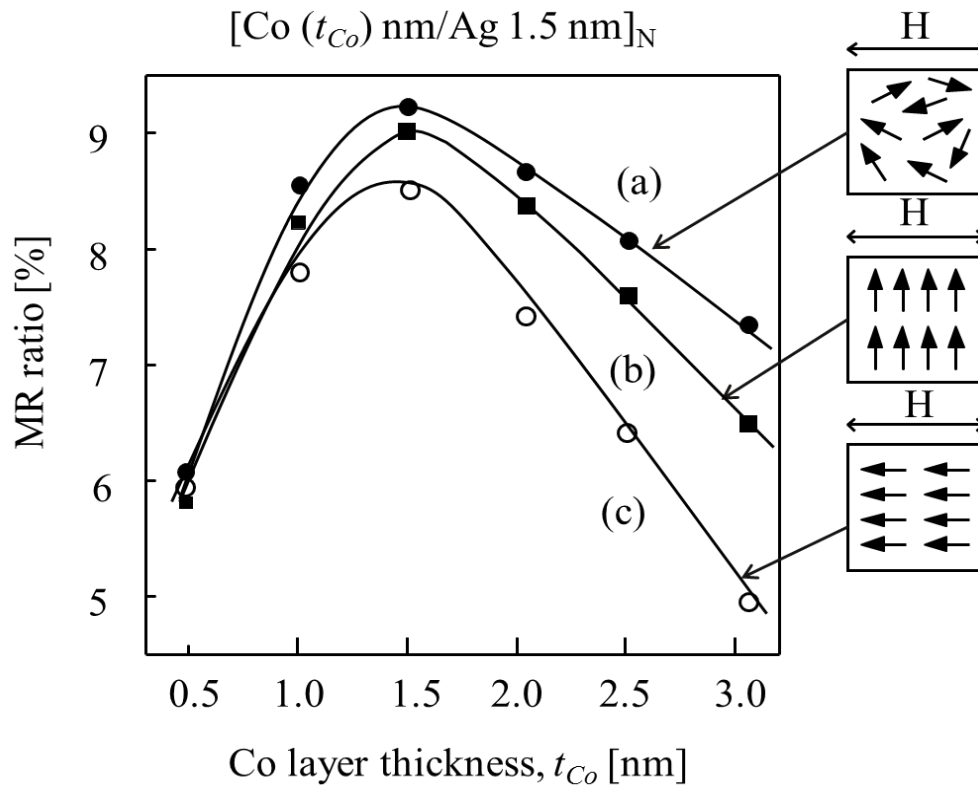


Figure 3-9 Co layer thickness dependence of the MR ratio for Ag layer thickness of 1.5 nm: (a) randomly oriented $[\text{Co}(t_{\text{Co}}) \text{ nm}/\text{Ag} 1.5 \text{ nm}]_N$ film and (b) and (c) uniaxially oriented $[\text{Co}(t_{\text{Co}}) \text{ nm}/\text{Ag} 1.5 \text{ nm}]_N$ films: field // hard axis and field // easy axis, respectively, at 21 kOe.

The reasons for this increase and decrease of the MR ratio with the Co layer thickness can be explained as:

- (a) As the Co layer adjacent to the nonmagnetic Ag layer becomes to be discontinuous for the multilayers having thin Co layer (i.e., $t_{\text{Co}} < 1.5$ nm), the MR ratio is small due to the decrease in the regions of antiparallel alignment of spins.

- (b) On the other hand, when the Co layer adjacent to the Ag layer becomes to be continuous (i.e., $t_{Co} > 1.5$ nm), the MR ratio decreases due to the increase in the ferromagnetic regions not showing the optimum antiparallel alignment of the spins [75], [33].

Although the MR ratio of the isotropic $[Co(t_{Co})\text{ nm}/Ag\ 1.5\text{ nm}]_N$ multilayer is larger than the MR ratio of the anisotropic $[Co(t_{Co})\text{ nm}/Ag\ 1.5\text{ nm}]_N$ multilayer, the MR ratio with the applied field parallel to the hard axis shows the value larger than the MR ratio with the applied field parallel to the easy axis.

3.3.4 Cobalt Layer Thickness and Magnetic Anisotropy

The anisotropy constant, K_u , was determined from the measured magnetization curves. Figure 3-10 shows the anisotropy constant, K_u , at various Co layer thicknesses for the $[Co(t_{Co})\text{ nm}/Ag\ 1.5\text{ nm}]_N$ multilayers at room temperature. The notations t_{Co} and N indicate the Co layer thickness and the number of bilayers in the film, respectively. K_u is small for small Co layer thicknesses and it increases with the increase of Co layer thicknesses. The reason for showing the smaller anisotropy constant for the thinner Co layers at room temperature seems to be due to the formation of discontinuous layers [33].

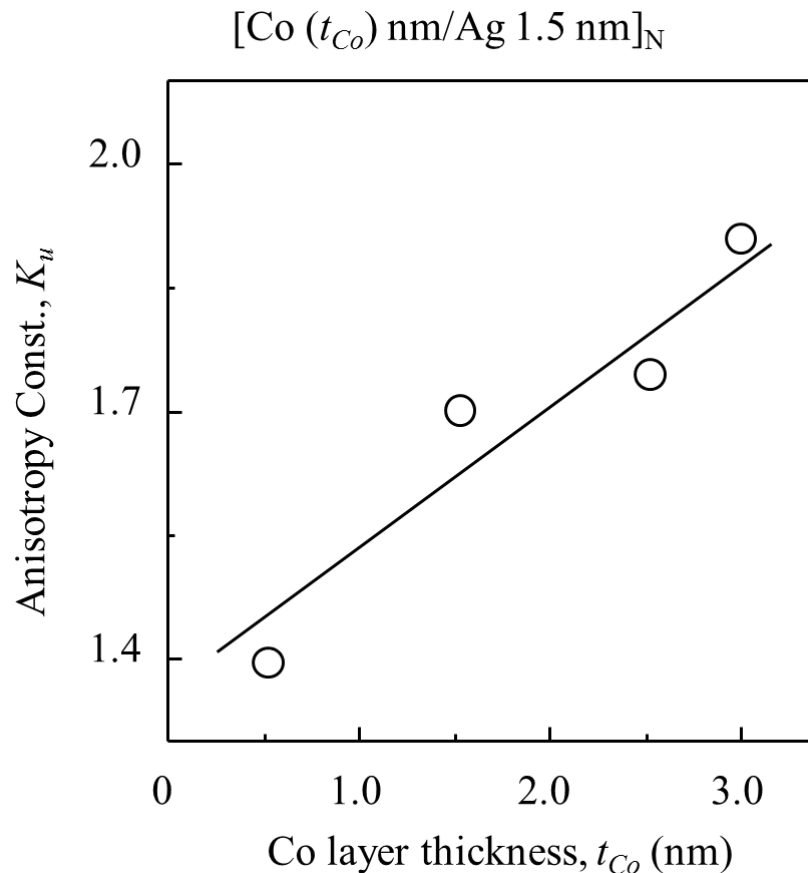


Figure 3-10 Relationship between the anisotropy constant, K_u , and the Co layer thickness, t_{Co} , for the $[Co\ 1.5\text{ nm}/Ag\ 1.5\text{ nm}]_N$ multilayer.

3.3.5 Magnetic Anisotropy and the MR Ratio

Figure 3-11 shows the correlation between the MR ratio and the anisotropy constant, K_u , for (a) magnetic field, H , applied parallel to the hard axis and (b) magnetic field, H , applied parallel to the easy axis. The MR ratio of the [Co 1.5 nm/Ag 1.5 nm]_N multilayer film when the H field was applied parallel to the hard axis is about 9.1 %, which is larger than the MR ratio for the H field applied parallel to the easy axis. The overall MR ratio with the H field applied parallel to the magnetic hard axis (i.e., parallel to the direction of strain) is more significant than the H field applied parallel to the magnetic easy axis (i.e., perpendicular to the direction of strain) for all the films. As the orientation characteristic of the multilayer becomes strong, depending on the direction of the applied magnetic field (and the current), the difference in the slopes of the MR ratio increases.

The smaller difference between the number of parallel and anti-parallel alignments of the magnetic spins in the ferromagnetic layers seemed to be the major factor for showing the smaller MR ratio for the anisotropic (oriented) multilayer films [33].

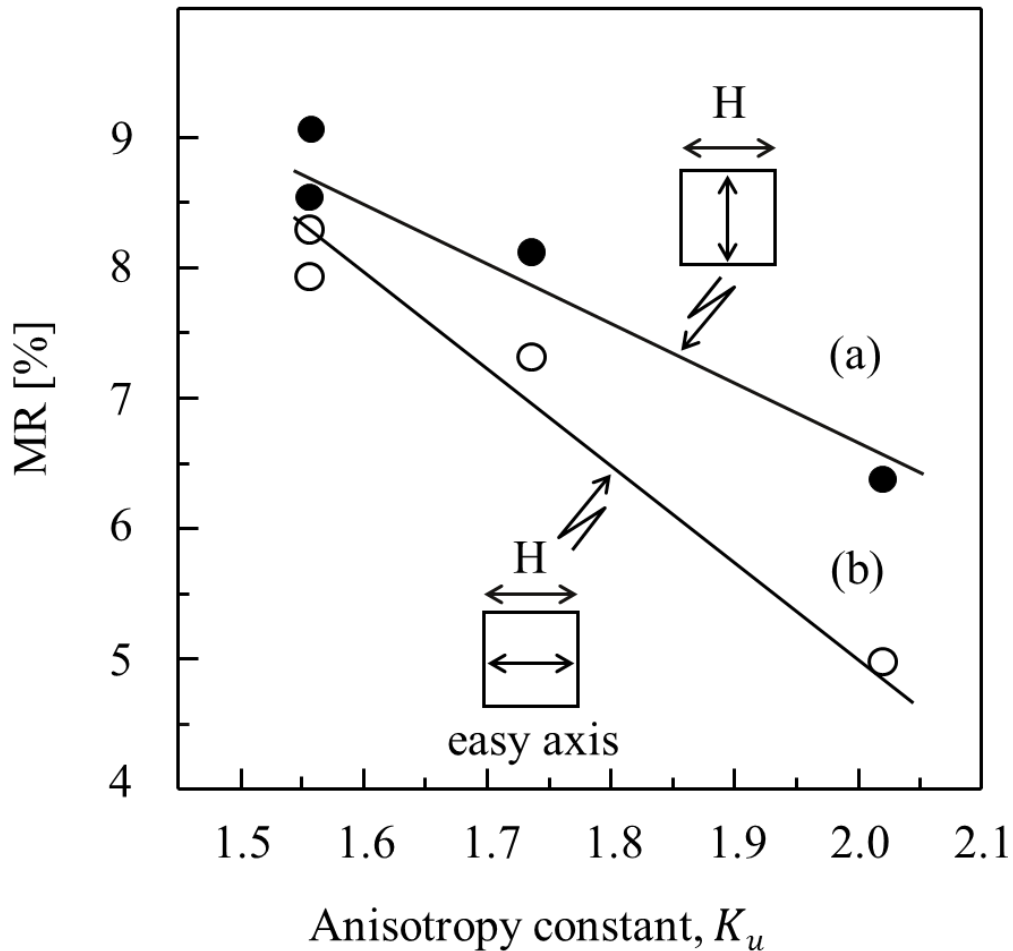


Figure 3-11 The MR ratio versus anisotropy constant, K_u , for the [Co 1.5 nm/Ag 1.5 nm]_N multilayer for (a) magnetic field, $H // \text{hard axis}$ and (b) magnetic field, $H // \text{easy axis}$.

3.3.6 Magnetic Anisotropy and Torque Curves

Figure 3-12(a) is a normal view of a [Co 1.5 nm/Ag 1.5 nm]₂₀ multilayer. It shows the direction of induced strain, the direction of induced magnetization, and the direction of applied magnetic field. The easy axis of magnetization lies in a plane perpendicular to the direction of strain. Fig. 1(b) illustrates the anisotropic energy measurement scheme. It shows the position of a circular Co/Ag multilayer, which is placed between two electromagnets. Fig. 1(c) shows a torque curve, K_u (the amplitude of the torque curve) versus θ (the angle between the saturation magnetization and the easy axis). The slope of the curve at $\theta = 0$ and 180° is negative (for the stable position) and the slope of the curve at $\theta = 90$ is positive (for the unstable position). Similar trends were also observed for Co/Cu [5], Co/Au [123], [26], Ni/Cu [83], and Fe/Cu [65] multilayers.

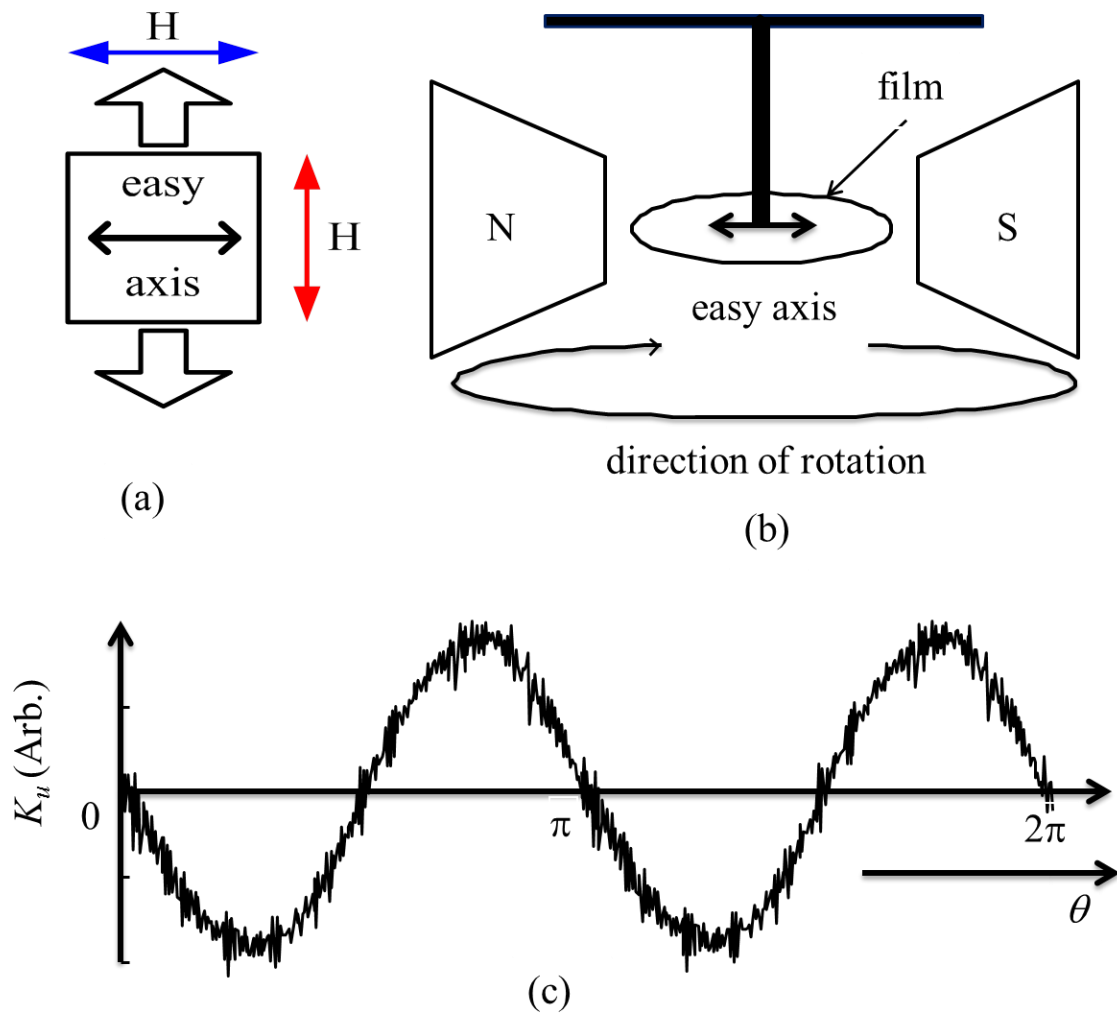


Figure 3-12 (a) Co/Ag multilayer showing the direction of strain, the direction of magnetic field, and the direction of induced easy axis due to strain, (b) schematic of a torque meter, and (c) torque curve.

3.3.7 Field Dependence of the MR Ratio in High Fields

Figure 3-13 shows the field dependence of the MR ratio for the isotropic and anisotropic $[\text{Co } 3.0 \text{ nm}/\text{Ag } 1.5 \text{ nm}]_{20}$ multilayers at the magnetic field, H , of 0 to ± 21 kOe. The multilayers exhibited the GMR effect. The maximum MR ratio observed is 7.2 % for the $[\text{Co } 3.0 \text{ nm}/\text{Ag } 1.5 \text{ nm}]_{20}$ multilayer. It shows a sharp drop in the MR ratio at low applied fields, i.e., near the zero magnetic field. This means higher sensitivity to resistance change at low fields.

The decreasing tendency of the field dependence of the MR ratio for both the isotropic and anisotropic multilayers is similar. However, for the isotropic $[\text{Co } 3.0 \text{ nm}/\text{Ag } 1.5 \text{ nm}]_{20}$ multilayer films, the field dependence of the MR ratio does not depend on the direction of the applied field or the direction of the current. As for the anisotropic $[\text{Co } 3.0 \text{ nm}/\text{Ag } 1.5 \text{ nm}]_{20}$ multilayer films, a distinct difference between the field dependence of the MR ratios measured against the easy and hard axes is observed. The difference of the MR ratio widens as the field is increased. This is attributed to an AMR effect [33].

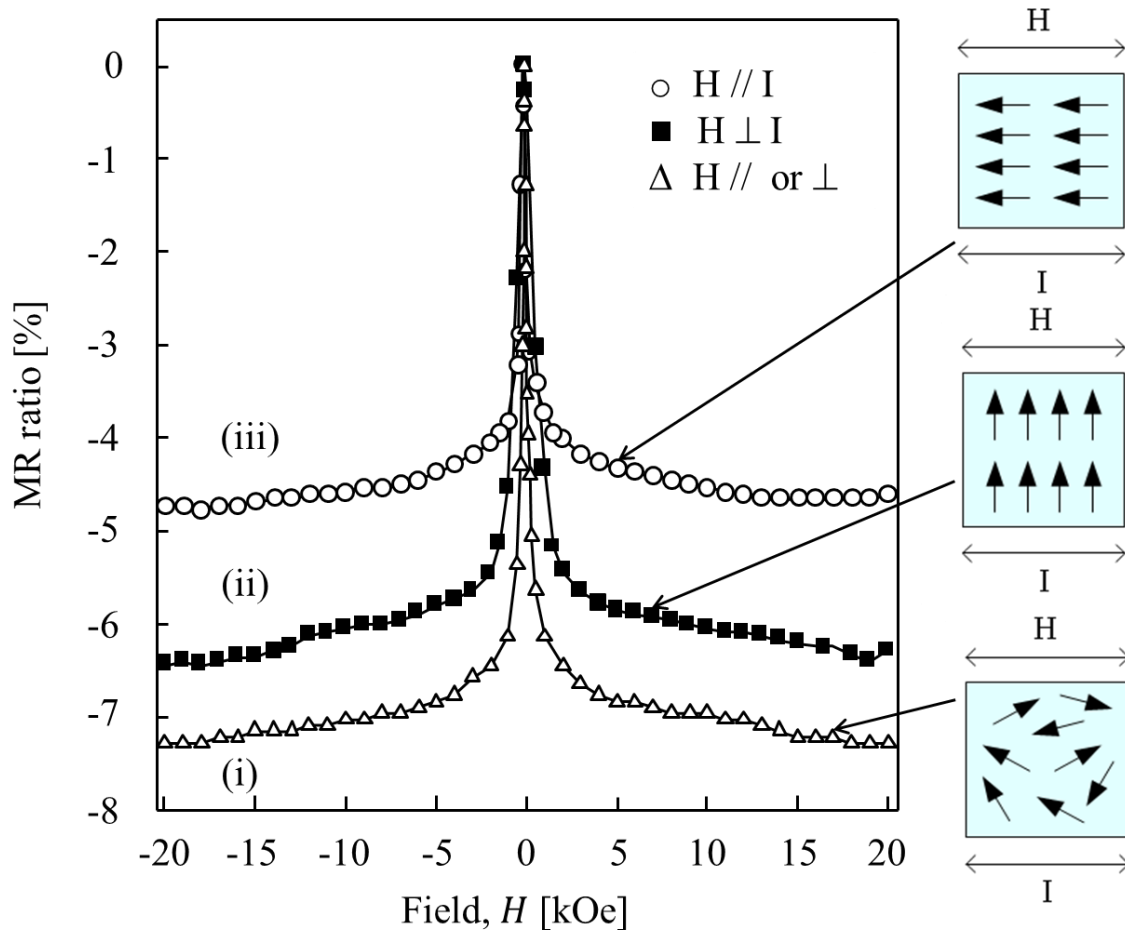


Figure 3-13 Field dependence of the MR ratio for $[\text{Co } 3.0 \text{ nm} / \text{Ag } 1.5 \text{ nm}]_{20}$ multilayer at $H = \pm 21$ kOe: open triangle, Δ , is for the isotropic multilayers, and open circles, \circ , $H \parallel$ easy axis and closed squares, \blacksquare , $H \perp$ hard axis are for the anisotropic multilayers. Solid lines are guides for the eyes.

3.3.8 Degree of Magnetic Anisotropy and the MR Ratio

Figure 3-14 shows the MR ratio of the $[\text{Co}(t_{\text{Co}}) \text{ nm} / \text{Ag} 1.5 \text{ nm}]_N$ multilayer as the degree of anisotropy, β , a ratio of $M_{r//}$ (magnetization measured when the applied magnetic field was parallel to the easy axis) and $M_{r\perp}$ (magnetization measured when the applied magnetic field was perpendicular to the easy axis), is increased. A clear difference in the MR ratio is observed between the applied field parallel and perpendicular to the easy and hard axes. The MR ratio is larger when the field is applied perpendicular to the hard axis and the current than when it is applied parallel to the easy axis and the current for the entire range of Co thicknesses. These results are consistent with the field dependence of the MR ratio of the Co/Cu [5] and the Co/Au [4] multilayers.

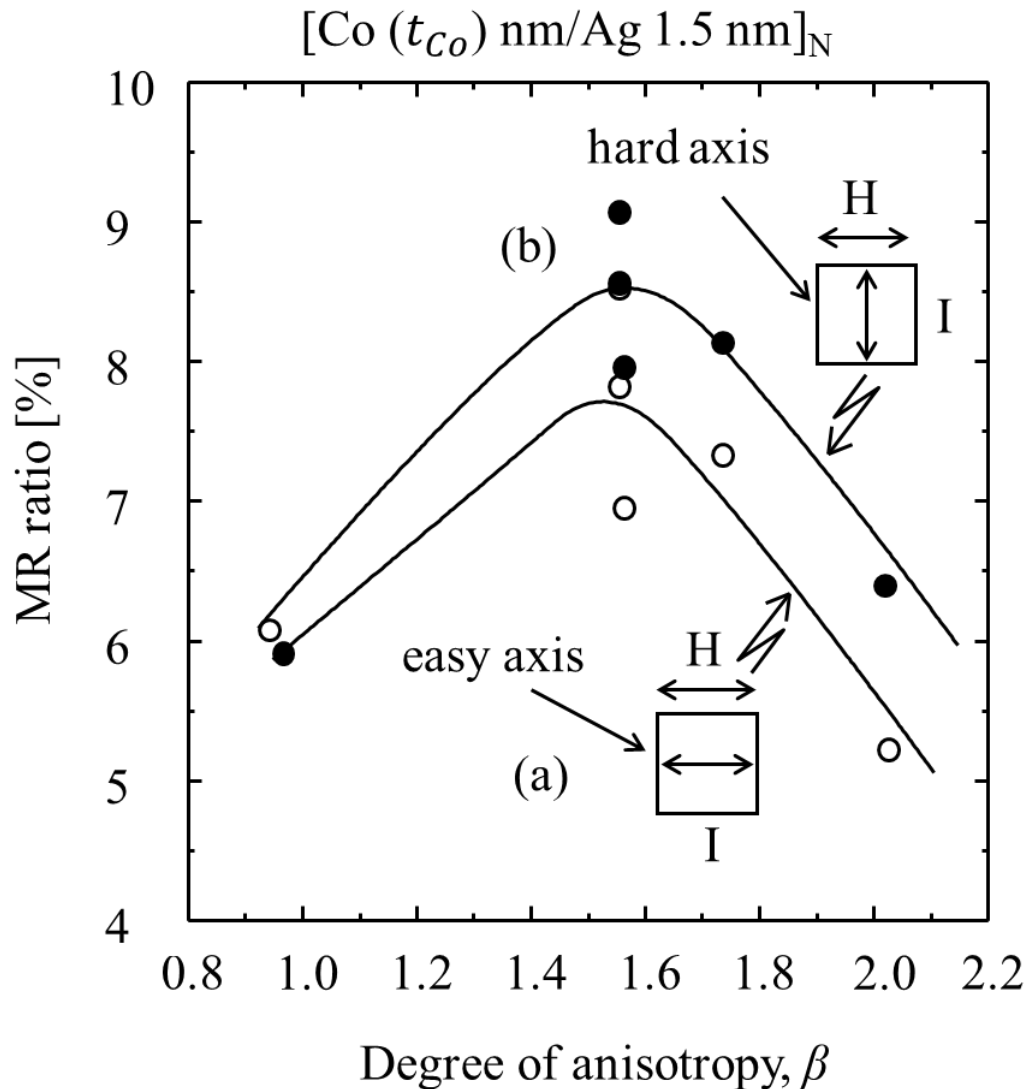


Figure 3-14 The MR ratio versus degree of anisotropy, β , for the anisotropic $[\text{Co}(t_{\text{Co}}) \text{ nm} / \text{Ag} 1.5 \text{ nm}]_N$ multilayers: (a) $H // \text{easy axis}$ and (b) $H // \text{hard axis}$, measured at 21 kOe.

3.3.9 Cobalt Layer Thickness and Electrical Characteristics

3.3.9.1 Randomly Oriented Multilayers

Figure 3-15 shows (a) an randomly oriented (isotropic) multilayer and two different measurement configurations, and b(i) electrical resistance, R , at the zero applied field, b(ii) a change in resistance, ΔR , due to the applied magnetic field, H , and b(iii) the MR ratio at various Co layer thicknesses (0 to 3 nm). The value of R for the $[\text{Co}(t_{\text{Co}}) \text{ nm} / \text{Ag } 1.5 \text{ nm}]_N$ multilayer remains almost constant at the small Co layer thicknesses. It increases slightly as the Co layer thickness is increased. In contrast, both the values of ΔR and the MR ratio reach a maximum and a minimum at the same time. This implies that the increase of R does not mean the increase or decrease of MR or vice versa, because the mechanism of conductivity in ferromagnetic multilayers is different at zero and applied magnetic fields. The maximum MR ratio of 9.1 % is observed at a Co layer thickness of 1.5 nm.

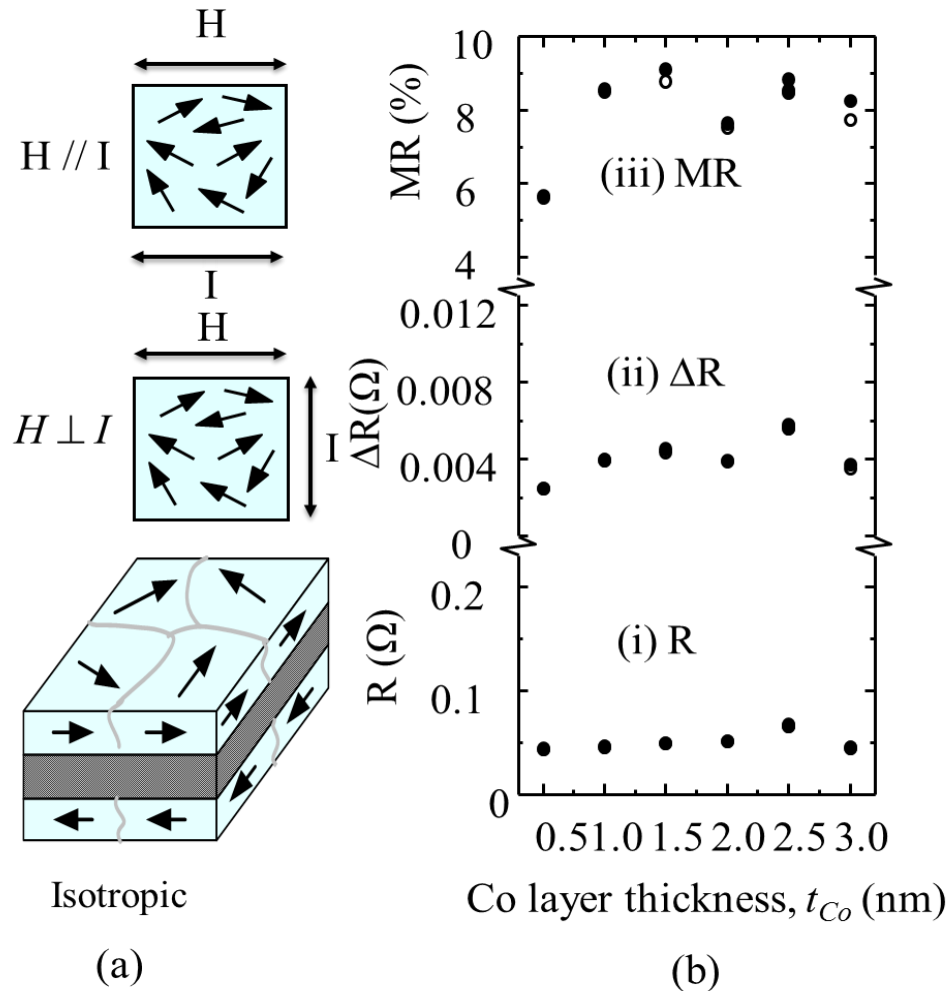


Figure 3-15 (a) Isotropic multilayer and two different measurement configurations and (b) (i) R vs. t_{Co} , (ii) ΔR vs. t_{Co} , and (iii) MR ratio vs. t_{Co} , for the $[\text{Co}(t_{\text{Co}}) \text{ nm} / \text{Ag } 1.5 \text{ nm}]_N$ multilayer.

3.3.9.2 Uniaxially Oriented Multilayers

Figure 3-16 shows (a) an uniaxially oriented (anisotropic) multilayer and four different measurement configurations, and b(i) electrical resistance, R , at zero applied field, b(ii) change in resistance, ΔR , due to the applied magnetic field, and b(iii) the MR ratio at various Co layer thicknesses (0 to 3 nm). The measurement methods were similar to those given in Figure 3-15, except that the measurement of the MR ratio was carried out in four different configurations instead of two. The MR ratio measured along the easy and hard axes with the field parallel and perpendicular to the direction of the current are found to differ in magnitude but the increasing and decreasing behaviours are similar. The difference between the MR ratio increases with the increase of Co layer thickness. The overall MR ratio with $H // \text{hard axis}$ and $H \perp I$ is again larger than the MR ratio with $H // \text{easy axis}$ and $H // I$. This result is consistent with the results of Co/Cu multilayers [5].

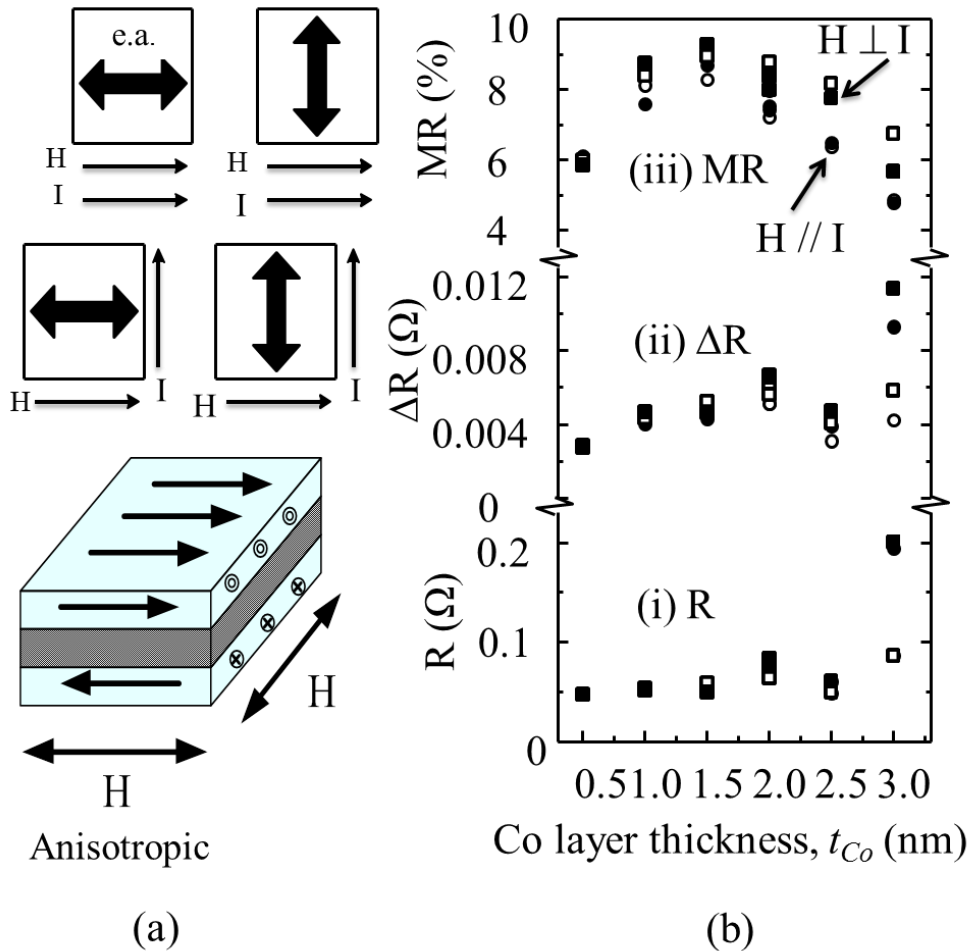


Figure 3-16 (a) Anisotropic multilayer showing various measurement configurations, circles (●, ○) indicate $H // \text{easy axis}$ and squares (■, □) indicate $H // \text{hard axis}$, with the direction of the current in parallel and perpendicular to the applied field, b(i) R vs. t_{Co} , (ii) ΔR vs. t_{Co} , and (iii) MR vs. t_{Co} for the [Co (t_{Co}) nm/Ag 1.5 nm]_N multilayer.

3.3.10 Strain and the Field Dependence of Magnetization

Figure 3-17 shows the room temperature magnetization curves for the $[\text{Co } 1.5 \text{ nm} / \text{Ag } 1.5 \text{ nm}]_{20}$ multilayers. The magnetization curves were measured when the magnetic field was applied parallel and perpendicular to the direction of the easy and hard axes at various strains (ϵ is changed from 0 to 1.5 %). At $\epsilon = 0$, the magnetization of the multilayer shows magnetically isotropic behavior. However, when the value of ϵ is increased to 1.5 %, in the increment of 0.5 %, it shows anisotropic character, i.e., there exists a clear difference between the magnetization curves for magnetic fields applied parallel and perpendicular to the direction of the easy axis. Note that the easy axis lies along the perpendicular to strain.

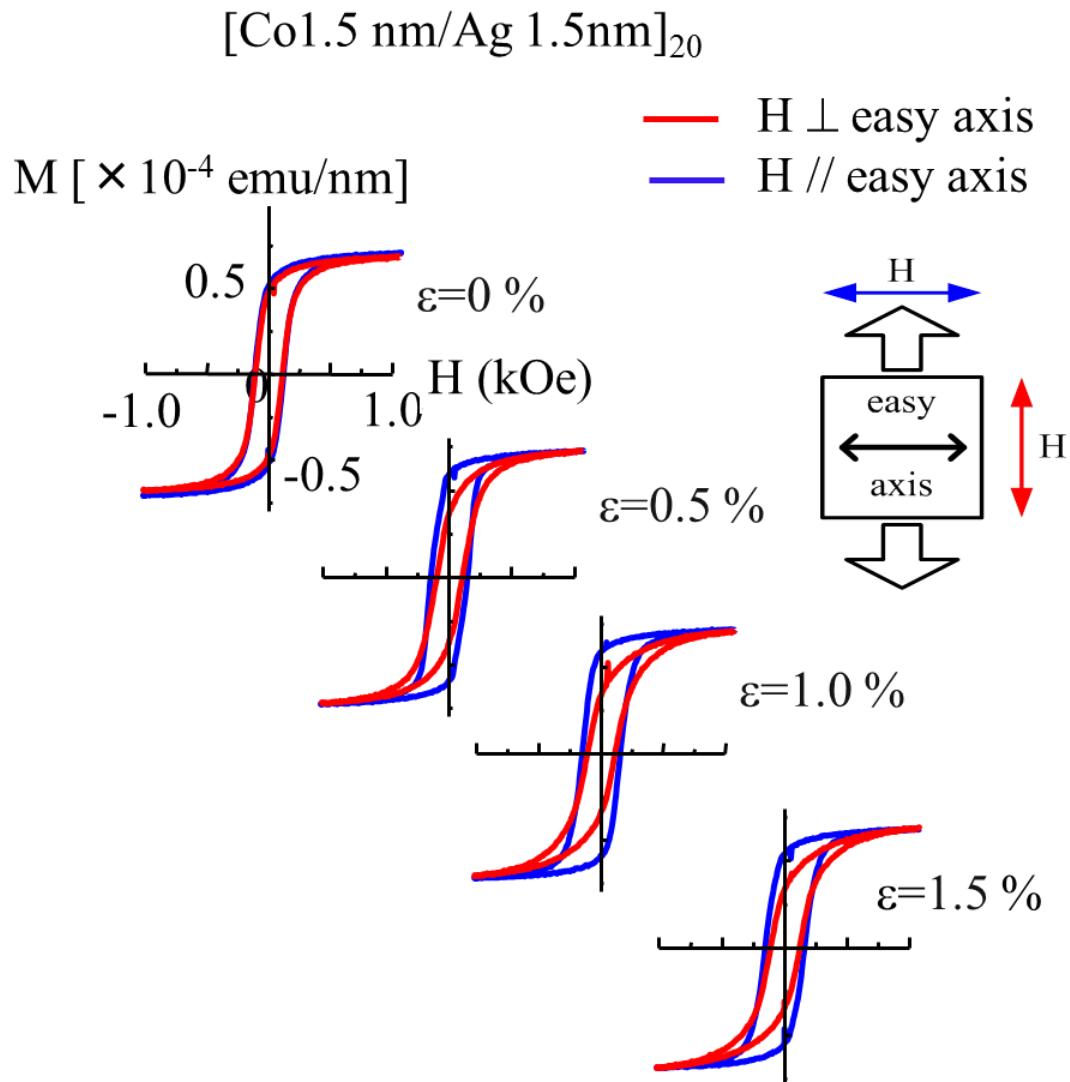


Figure 3-17 Field dependence of magnetizations for various values of ϵ (0 to 1.5 %). The magnetic field was applied along the parallel and perpendicular to the easy axis.

3.3.11 Strain and Degree of Anisotropy

Figure 3-18 shows the relationship between the remnant magnetization ratio and the strain for the [Co 1.5 nm /Ag 1.5 nm]₂₀ multilayers. The remnant magnetization ratio fits linearly with ϵ for the coefficient of determination, $r^2 = 0.90$. The result suggests that antiferromagnetically coupled magnetic moments between the Co layers are systematically changed because of the induced strain [124], [125].

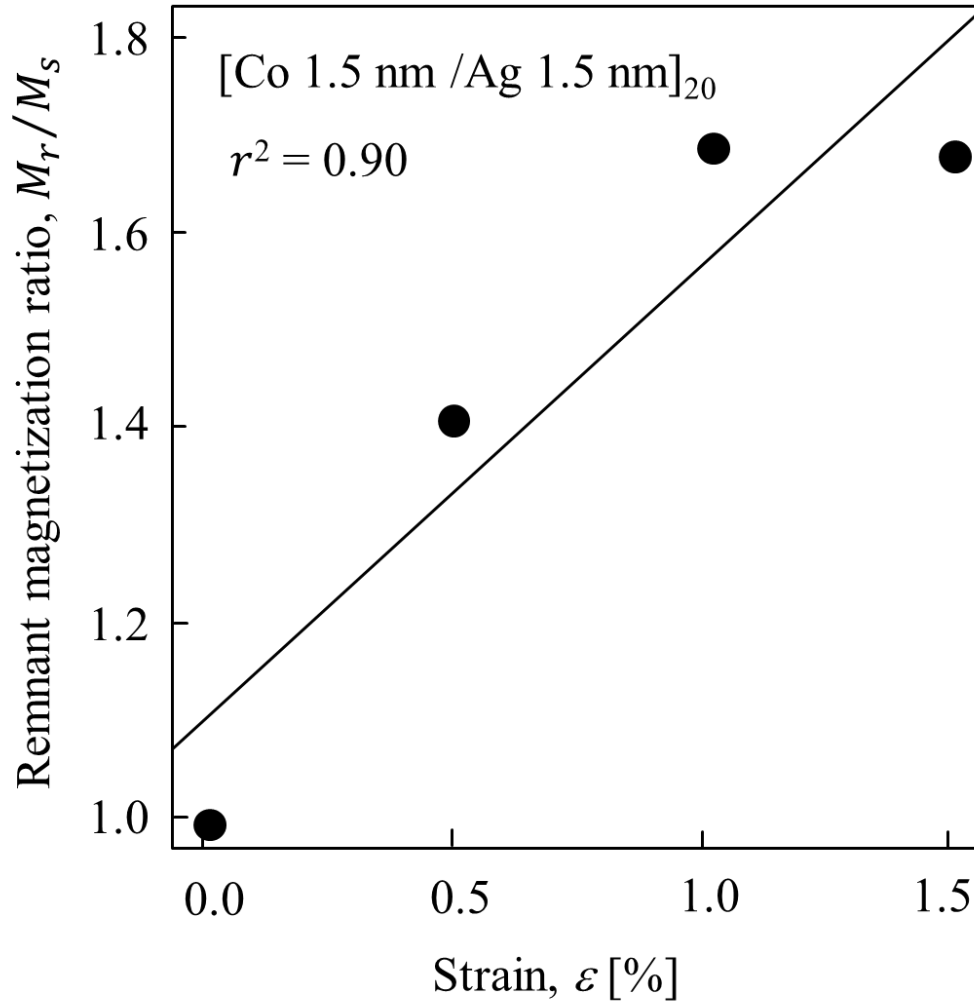


Figure 3-18 Relationship between the remnant magnetization ratio (M_r/M_s) and strain, ϵ . ϵ is increased from 0 to 1.5 %, superimposed with a 90 % best linear fit.

3.4 Summary

A series of Co/Ag multilayers was grown on polyimide substrates using pulsed-current deposition. Magnetic anisotropy was induced, at low magnetic fields, via strain. The multilayers produced interesting MR and magnetic characteristics. All of the multilayers exhibited magnetic anisotropy when the strain was increased

from 0 to 1.5 %. In particular, the magnetism of the multilayers produced at the strain value of 1.5 % showed a remarkable magnetic anisotropy. The orientation of the easy axis is found to be perpendicular to the direction of strain.

The field dependence of the MR ratio studied at both high and low magnetic fields showed interesting MR characteristics. The MR ratio consisted of the GMR and AMR components. For the isotropic Co/Ag multilayers, the field dependence of the MR ratio did not depend on the direction of the applied magnetic field or the current. However, for the multilayers produced at the strain value of 1.5 %, a clear difference between the field dependence of the MR ratio was observed when the MR ratio was measured along the parallel and the perpendicular to the direction of the easy axis or the current. In weak magnetic fields, the field dependence of the MR ratio clearly corresponded to the shape of the magnetization curve, depending on the orientation of the magnetization curves.

The MR ratio of the Co/Ag multilayer was also studied at various Co layer thicknesses for both the isotropic and anisotropic multilayers. A maximum MR ratio of 9.1 % was observed for a Co layer thickness of 1.5 nm. The overall MR ratio when the magnetic field was applied parallel to the hard axis was found to be more significant than when the magnetic field was applied parallel to the easy axis.

Due to the high sensitivity to resistance change at low magnetic fields, Co/Ag multilayers have a number of potential applications such as in computers, electronic devices (as a memory or sensors), magnetic field measurements, and in the automotive sectors. The potential application of Co/Ag nanostructures has also been foreseen in the biomedical sectors [126].

Chapter 4: Magnetoresistance Effect and Magnetic Properties of Co/Cu Multilayers⁹

4.1 Introduction

Co-based multilayers prepared by special means continue to dominate fundamental research [127] and applications in electronic engineering [63], [59], [67]. The physical properties of these multilayers vary depending on their growth conditions [16], [123]. For example, both the GMR effect and the magnetic anisotropy properties of the Co/Cu multilayers are found to be strongly influenced by the interfacial states between the Co and Cu layers [6], [23], [128].

In Chapter 2, experimental results of the GMR effect and magnetic properties of the specially grown Co/Au multilayers were presented and in Chapter 3, the same properties were studied for the Co/Ag multilayers. While both fcc-Au and fcc-Ag have almost 15 % lattice mismatch with Co, the lattice mismatch between fcc-Cu and Co is only 1.5 %. Therefore, it is interesting to compare the results of the Co/Cu multilayers with the results of the Co/Au and Co/Ag multilayers. In this work, $[\text{Co}(t_{\text{Co}}) \text{ nm}/\text{Cu} 1.5 \text{ nm}]_N$ multilayers are grown using pulsed-current deposition on polyimide substrates, as this method offers precision in the growth on an atomic scale [47]. The notations t_{Co} and N indicate the Co layer thickness and the number of Co/Cu bilayers, respectively.

Under normal deposition conditions, Co/Cu multilayers seldom exhibit any magnetic anisotropy. We learned from Chapter 3 that the magnetic anisotropy can be induced via strain. This chapter begins with the study of the relationship between the stress, σ , and the strain, ε , for the Co/Cu multilayers, deposited on, the

⁹ A version of this chapter has been published. Sections 4.3.2 through 4.3.5 are reprinted from [5] with permission. © 2010 IEEE. Rizal, C. Magnetoresistance and magnetic properties of Co(t_{Co})/Cu multilayer films. *IEEE Transactions on Magnetics*. 6/2010. Sections 4.4.6 through 4.4.8 are reprinted from [6] with permission. © 2011 American Institute of Physics. Rizal, C., Gyawali, P., Kshattray, I., and Pokharel, R. K. Strain-induced magnetoresistance and magnetic anisotropy properties of Co/Cu multilayers. *Journal of Applied Physics*. 2/2012.

polyimide substrates. The magnetization measurement revealed that $[\text{Co} (t_{\text{Co}}) \text{ nm/Cu } 1.5 \text{ nm}]_{20}$ multilayers developed strong magnetic anisotropy at small applied fields (< 0.5 kOe) due to strain.

The maximum GMR for the $[\text{Co} (t_{\text{Co}}) \text{ nm/Cu } 1.5 \text{ nm}]_{20}$ multilayers was found near a Co layer thickness of 1 nm at $\varepsilon = 1.5 \%$ for both the isotropic and anisotropic multilayers. The field dependence of the magnetization was studied by changing the Co layer thickness and strain. All of the multilayers developed magnetic anisotropy due to strain. The $[\text{Co } 1.0 \text{ nm/Cu } 1.5 \text{ nm}]_{20}$ multilayer exhibited strong magnetic anisotropy at $\varepsilon = 1.5 \%$. The correlation between the remnant magnetization ratio and the Co layer thickness was also studied. In addition, the nature of the MR ratio and the magnetic anisotropy of the Co/Cu anisotropic multilayers were investigated. The extent to which the MR ratio varies with the direction of the applied magnetic field and the current in the film plane was also investigated as the magnitude of strain was changed.

4.2 Experimental Procedure

The $[\text{Co} (t_{\text{Co}}) \text{ nm/Cu } 1.5 \text{ nm}]_{20}$ multilayer films were deposited at a constant current density using a programmable dc source controlled by a microcomputer with the precise control of the current density and time. The distance between the cathode and the anode was kept at 2 cm. The solution was prepared using the double distilled water and pH was adjusted in the range of 3.0 to 5.0.

The electrolyte consisted of $\text{CoSO}_4 \cdot 7\text{H}_2\text{O}$ (28-39 g/l), $\text{CuSO}_4 \cdot 5\text{H}_2\text{O}$ (15-25 g/l), $\text{Na}_3\text{C}_6\text{H}_5\text{O}_7 \cdot 2\text{H}_2\text{O}$ (76 g/l), NaCl (2 g/l). The substrates consisted of 15-nm thin copper layer vapor deposited on the polyimide film. Earlier work used glass [129]. Annealing of the substrates was carried out at a temperature of 150 °C for 90 minutes in a vacuum below 1×10^{-7} Torr. In the electrolyte, the Co concentration was changed while keeping the Cu concentration constant, whereas the ratio between the concentrations of Co and Cu was varied.

The composition of the deposited multilayer films was determined using an energy dispersive X-ray analysis. The thickness of the thin film was obtained from the deposited mass and the density of the film, assuming the density of the thin film same as that of the density of the bulk film.

The electrical resistivity of the isotropic and anisotropic multilayer films was measured at room temperature by varying the relative direction of the magnetic field, H , and the current, I . The measurement configurations for these multilayers are shown in page 36, Figure 1-24. The MR ratio along the transverse and longitudinal directions of the measuring current was observed by measuring in two different configurations for the magneto-isotropic (randomly oriented) multilayer films. For the magneto-anisotropic (uniaxially oriented) multilayers, the MR ratio was measured in four different configurations by varying the relative direction of H and I . The values of both the MRs were negative. The magnetic field was varied in the range of ± 21 kOe. The induced strain was measured using a strain gauge.

The magnetic properties were investigated using a VSM. The anisotropy constant, K_u , and the degree of anisotropy, β , were calculated from the measured magnetization curves. The easy axis of magnetization was found along the perpendicular direction (in-plane) of strain.

4.3 Results and Discussions

This section begins with the stress-strain profile for the Co/Cu multilayers deposited on the polyimide substrates¹⁰. Magnetic anisotropy and the MR effects are studied extensively using magnetization curves for the as-deposited ($\varepsilon = 0$) and the strain-induced ($\varepsilon \neq 0$) [Co (t_{Co}) nm/Cu 1.5 nm]₂₀ multilayer films at low magnetic fields (< 1 kOe). The MR effect is studied by changing the ferromagnetic Co layer thickness at the constant Cu layer thickness of 1.5 nm. The field dependence of the MR ratio is studied at low applied fields ($H < 1$ kOe).

4.3.1 Stress versus Strain Profile

Figure 4-1 shows stress, σ , versus strain, ε profile for the [Co 1.0 nm/Cu 1.5 nm]₂₀ multilayers deposited onto the polyimide substrate. For easy observation, different strain limits and regions are labeled in the diagram. In the elastic region, σ is proportional to ε . At this limit, the slope of the tangent gives rise to Young's modulus, E . In the experiment, ε was changed from the elastic region to a plastic region of up to 1.5 % as this is the allowable strain that could be introduced into the multilayer without breaking up its crystalline structure. It is the region where the microstructural changes take place and, thus, the rearrangement of the magnetic spins in the Co layers [5], [94]. This process is irreversible [124].

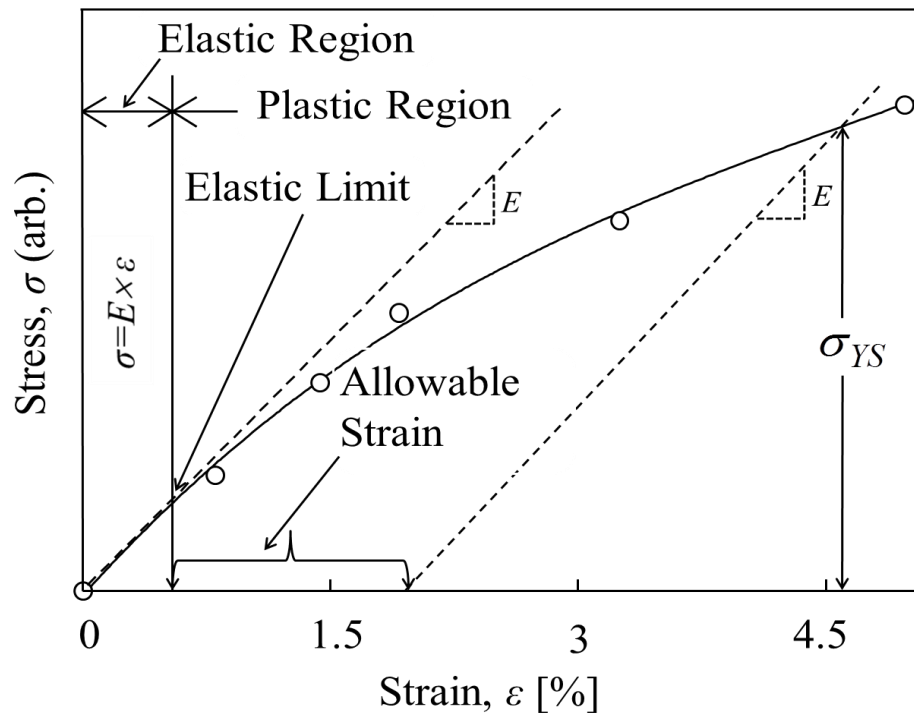


Figure 4-1 Schematic of stress, σ , versus strain, ε . The slope of the tangent gives rise to Young's modulus, E , and, σ_{YS} , is the yield strength. Elastic and plastic regions and allowable strain limits are labeled in the diagram. Reprinted from [6] with permission. © 2012 American Institute of Physics.

¹⁰ How the data were taken and analysed in this thesis is described in Appendix B.

4.3.2 Magnetic Anisotropy and the MR Ratio in Low Fields

Figure 4-2 illustrates the magnetic field dependence of the MR ratio and the corresponding magnetization curves, measured at the magnetic field, H , of ± 1 kOe for the strained-induced [Co 1.0 nm /Cu 1.5 nm]₂₀ multilayers (i.e., $\varepsilon = 1.5\%$). Figure 4-2 (a) shows the magnetic field dependence of magnetization, M , at 1 kOe. The measured magnetization curves show that the magnetism of the [Co 1.0 nm /Cu 1.5 nm]₂₀ multilayer is magnetically anisotropic. Figure 4-2 (b) shows the field dependence of the MR ratio for low applied fields (i.e., $H < 1$ kOe) at room temperature. Notice the high sensitivity at low magnetic fields. H_c is the coercive force that coincides with the peak of the MR at room temperature.

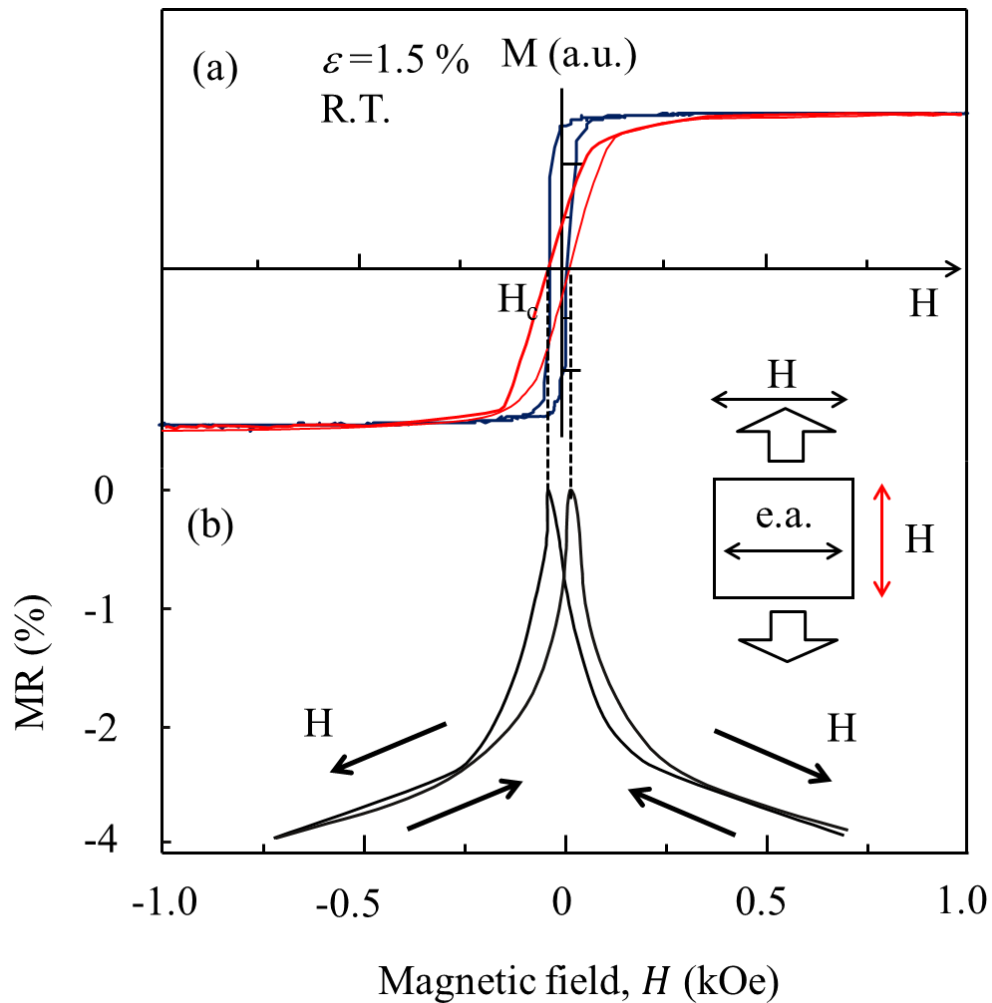


Figure 4-2 (a) Magnetization ($M - H$) curves and (b) field dependence of the MR ratio at low fields. Magnetization curves were measured along the field parallel and the perpendicular to the direction of the easy axis at room temperature (R.T.).

4.3.3 Cobalt Layer Thickness and MR

The magnetic field dependence of the MR ratio has been found to be very sensitive to both the Co and Cu layer thicknesses [130]. Figure 4-3 shows the Co layer thickness dependence of the MR ratio for the randomly and uniaxially oriented $[\text{Co } (t_{\text{Co}}) \text{ nm}/\text{Cu } 1.5 \text{ nm}]_N$ multilayer films. The MR ratio increases strongly until the Co layer thickness reaches 1.0 nm for all three types of multilayer films. Beyond this value, the MR ratio starts to decrease. This mechanism is similar to that reported for Co/Ag multilayers in Section 3.3.3 except that the Co layer thickness showing a maximum MR ratio is different.

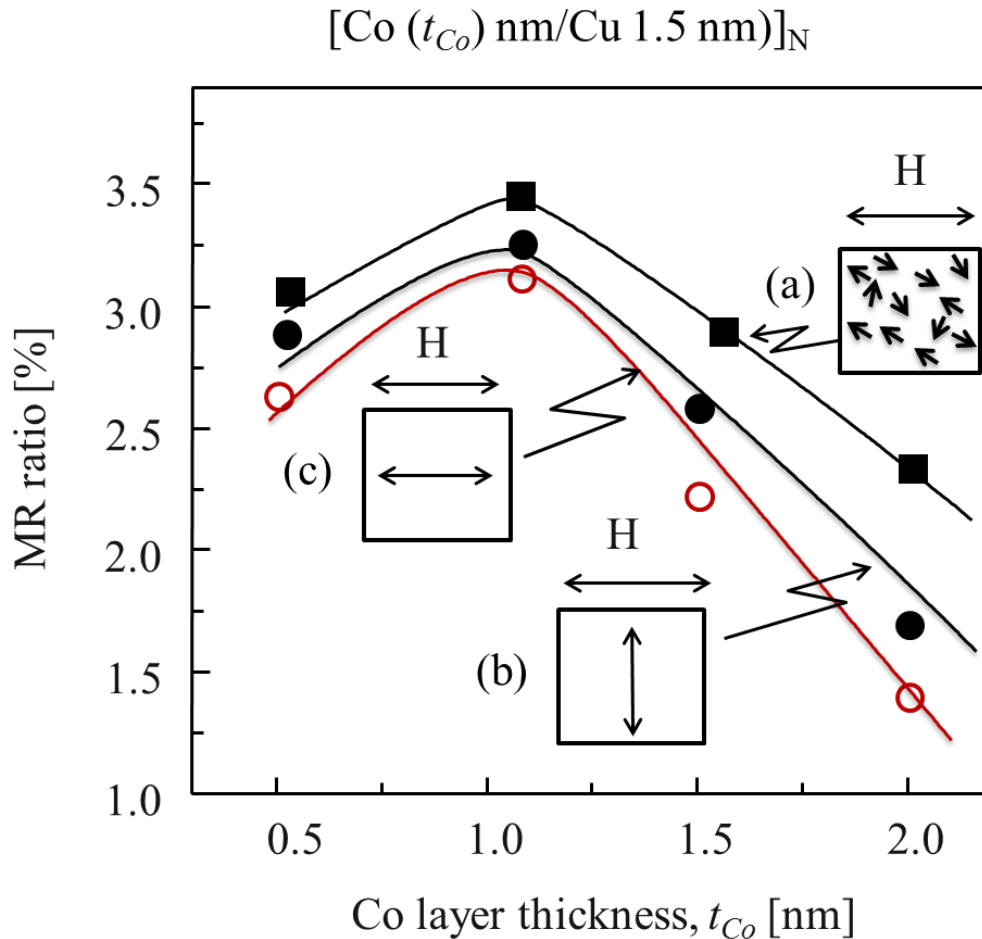


Figure 4-3 Co layer thickness dependence of the MR ratio for $[\text{Co } (t_{\text{Co}}) \text{ nm}/\text{Cu } 1.5 \text{ nm}]_N$: (a) randomly oriented film, (b) and (c) uniaxially oriented films: field // hard axis and field // easy axis, respectively.

The MR ratio for both the randomly and uniaxially oriented multilayers shows a maximum value at the Co layer thickness of 1.0 nm. The MR ratio of the randomly oriented film is larger than the MR ratio of the uniaxially oriented film for all Co layer thicknesses. For the uniaxially oriented films, the MR shows the larger value when the field is perpendicular to the easy axis than when it is parallel to the easy axis. The Cu layer thickness of 1.5 nm showing the maximum MR ratio is different from the Cu layer thickness showing the

maximum MR ratio for the multilayer films grown using sputtering or molecular beam epitaxy [63]. This is attributed to the composition of the ferromagnetic layer in the multilayer films.

4.3.4 Field Dependence of Magnetization

Figure 4-4 illustrates the field dependence of magnetization for the $[\text{Co} (t_{\text{Co}}) \text{ nm} / \text{Cu} 1.5 \text{ nm}]_N$ multilayers at a constant strain ($\varepsilon = 1.5 \%$) for various Co layer thicknesses (i.e., $t_{\text{Co}} = 0.5$ to 2.0 nm). The subscript N outside the parenthesis denotes the stacking number. The multilayers exhibited a clear magnetic anisotropy with the increase of Co layer thickness. The field dependence of magnetization at $t_{\text{Co}} = 1.0$ nm in Figure 4-4 corresponds to the Co layer thickness showing a maximum MR ratio in Figure 4-3.

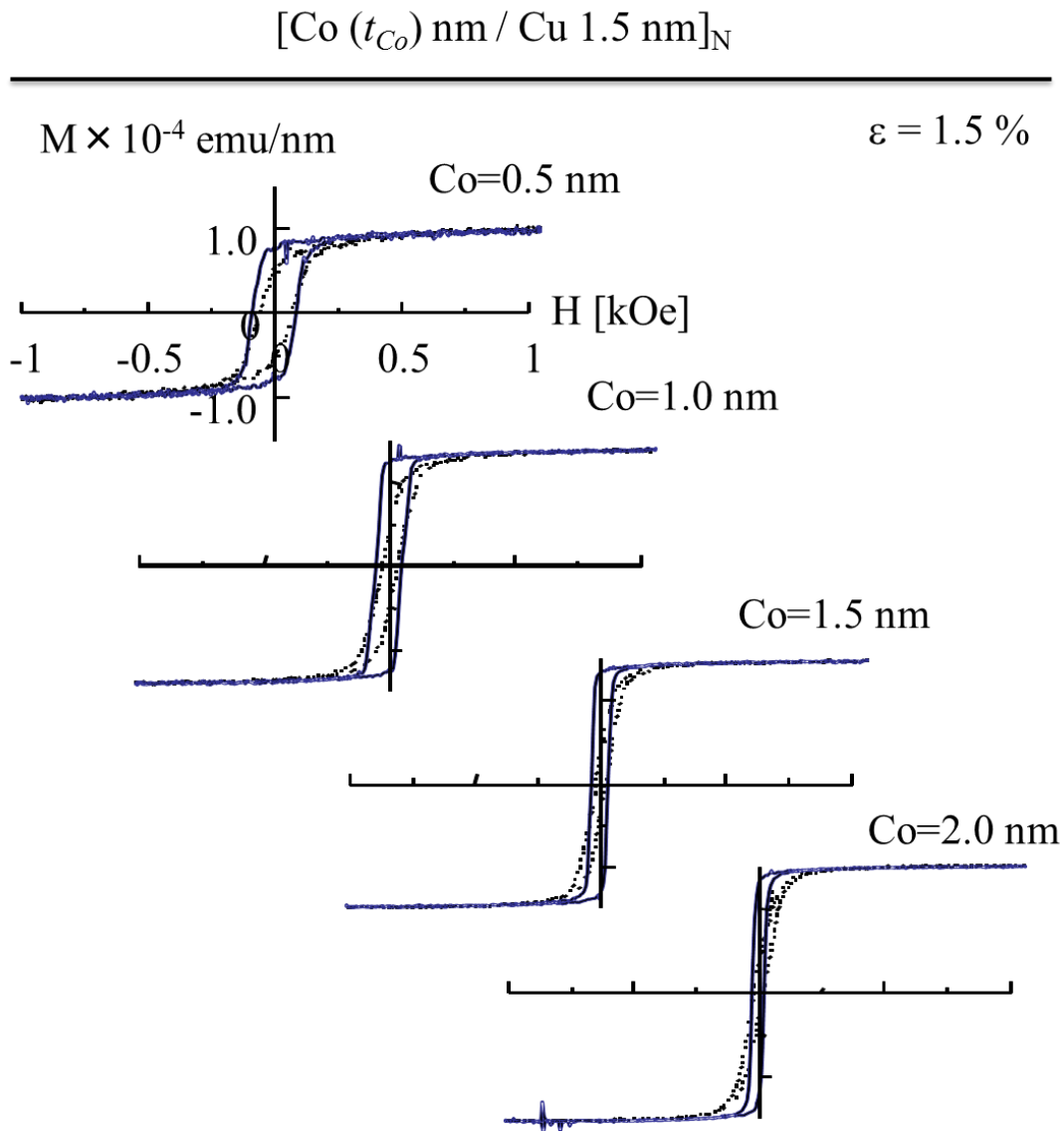


Figure 4-4 Experimental room temperature magnetization for the $[\text{Co} (t_{\text{Co}}) \text{ nm} / \text{Cu} 1.5 \text{ nm}]_N$ multilayers for various Co layer thicknesses at $\varepsilon = 1.5 \%$.

4.3.5 Cobalt Layer Thickness and Degree of Anisotropy

The correlation between the remnant magnetization ratio, β , (a ratio of the magnetization when the magnetic field was applied parallel and perpendicular to the easy axis) and the Co layer thickness is shown in Figure 4-5. This relationship was obtained using the experimental values of the parallel and perpendicular remnant fields of the magnetization curves from Section 4.3.4. There is a linear relationship between the remnant magnetization ratio and the Co layer thickness. This result suggests that both the net antiferromagnetically (AF) coupled magnetic moments and their coupling strengths in the multilayer are systematically varied as the Co layer thickness is increased from 0.5 nm.

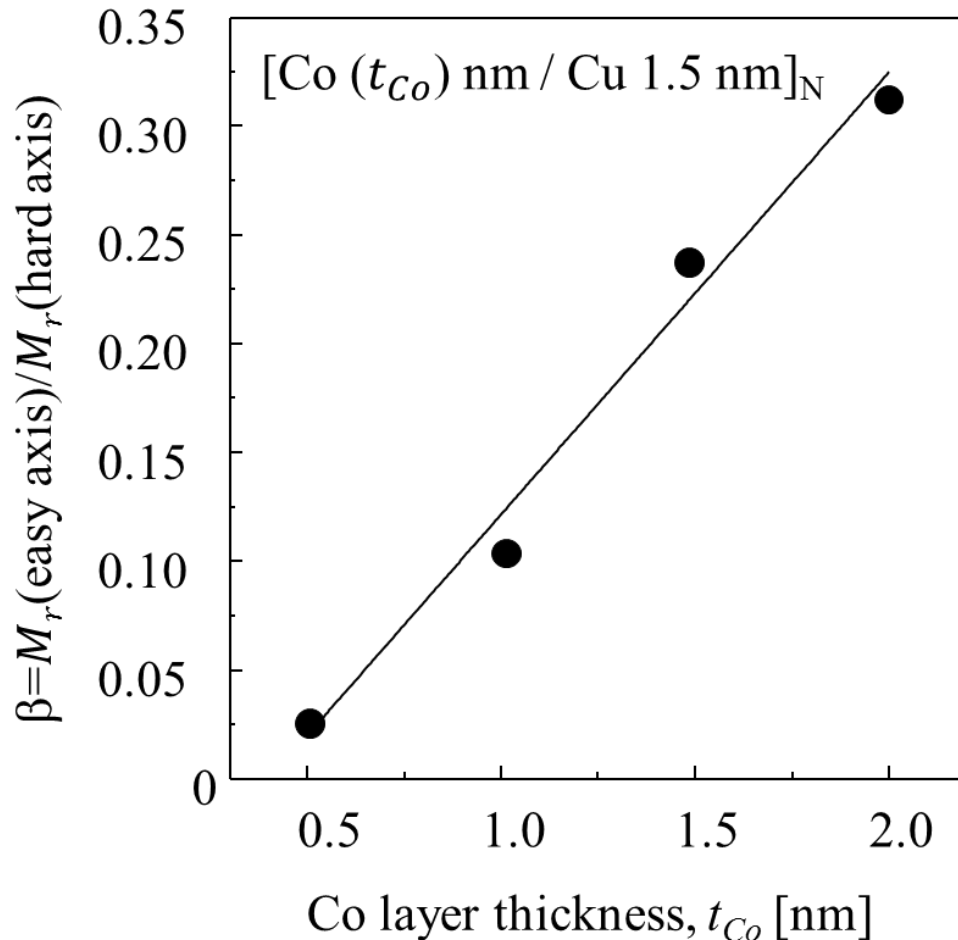


Figure 4-5 Remnant magnetization ratio, β , versus Co layer thickness.

4.3.6 Degree of Anisotropy and the MR Ratio

Figure 4-6 illustrates the MR ratio of the anisotropic $[\text{Co } 1.0 \text{ nm}/\text{Cu } 1.5 \text{ nm}]_N$ multilayers against the degree of anisotropy, β , when the magnetic field was applied parallel and perpendicular to, ϵ . The subscript N outside the parenthesis denotes the stacking number. The MR ratio increases with β and peaks at around $\beta = 0.1$

followed by a decrease, which is consistent with the Co layer thickness dependence of the MR ratio [5]. The maximum MR ratio of 3.2 % observed at $\beta = 0.1$ corresponds to $\varepsilon = 1.5$ % in Figure 4-1. The increasing and decreasing behaviors of the MR ratio with β when $H \parallel \varepsilon$ and $H \perp \varepsilon$ are different, and the gap between these two curves widens as β increases.

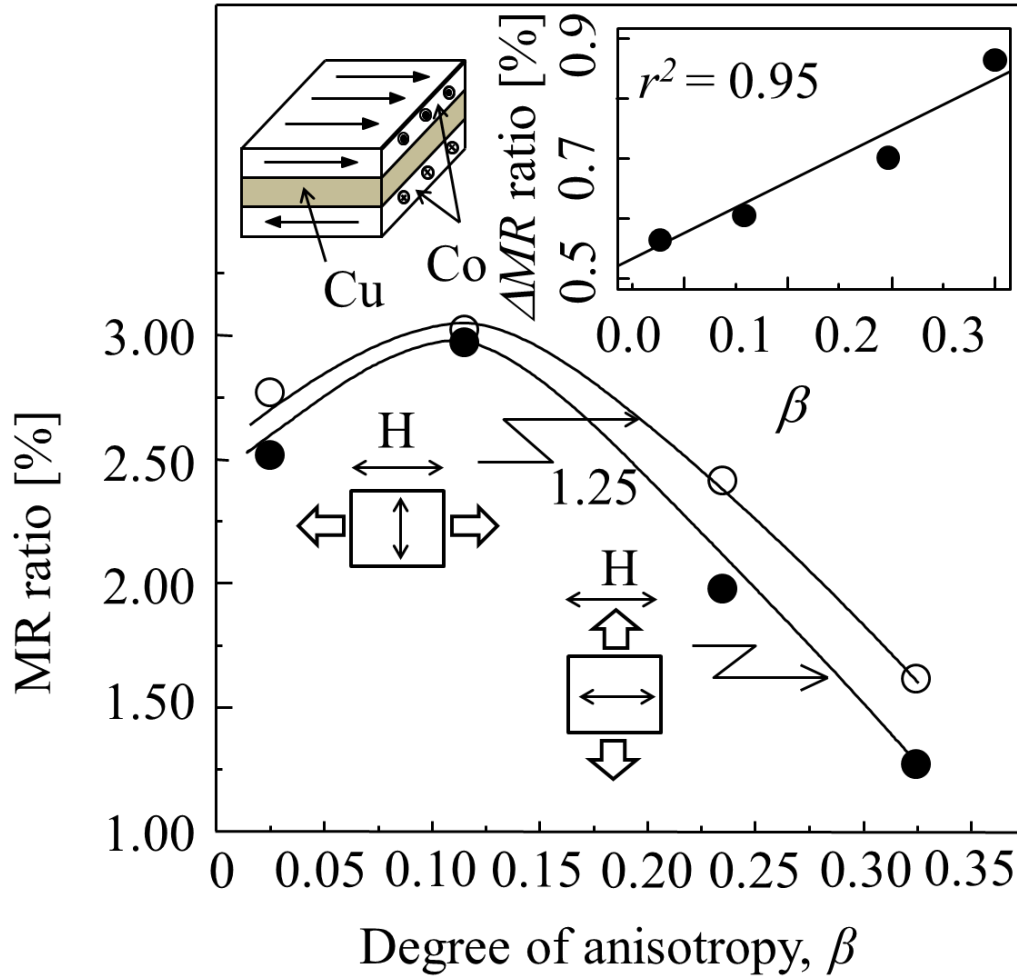


Figure 4-6 The MR ratio versus the degree of anisotropy, β , a ratio of $M_{r//}$ (magnetization measured when the applied magnetic field was perpendicular to strain, i.e., parallel to the easy axis) and $M_{r\perp}$ (magnetization measured when the applied field was parallel to strain, i.e., perpendicular to the easy axis). The inset shows % ΔMR versus β , being superimposed with a 95 % best linear fit.

The MR result suggests that MR with $H \parallel \varepsilon$ is always larger than when $H \perp \varepsilon$. The inset shows a difference between the MR ratio measured when $H \parallel e.a.$ (easy axis) and $H \perp e.a.$ (easy axis) as β is increased from 0 to 0.35. The value of ΔMR increases from 0.54 to 0.85 owing to the increase in β . The position of the MR ratio peak at $\beta = 0.1$ in Figure 4-6 corresponds to the Co layer thickness of 1.0 nm in Figure 4-3. The ΔMR ratio fits linearly with β for the coefficient of determination, $r^2 = 0.95$.

4.3.7 Strain and Magnetic Anisotropy

Figure 4-7 shows a relationship between the magnetic anisotropy constant, K_u , and strain, ε , for the [Co 1.0 nm/Cu 1.5 nm]₂₀ multilayer film. The inset in it shows the magnetization curves measured when the magnetic field was applied parallel and perpendicular to the direction of the current. It shows the extent to which K_u changes when ε is changed from 0 to 1.5 %. K_u sharply increases with ε up to 1, followed by a slow increase.

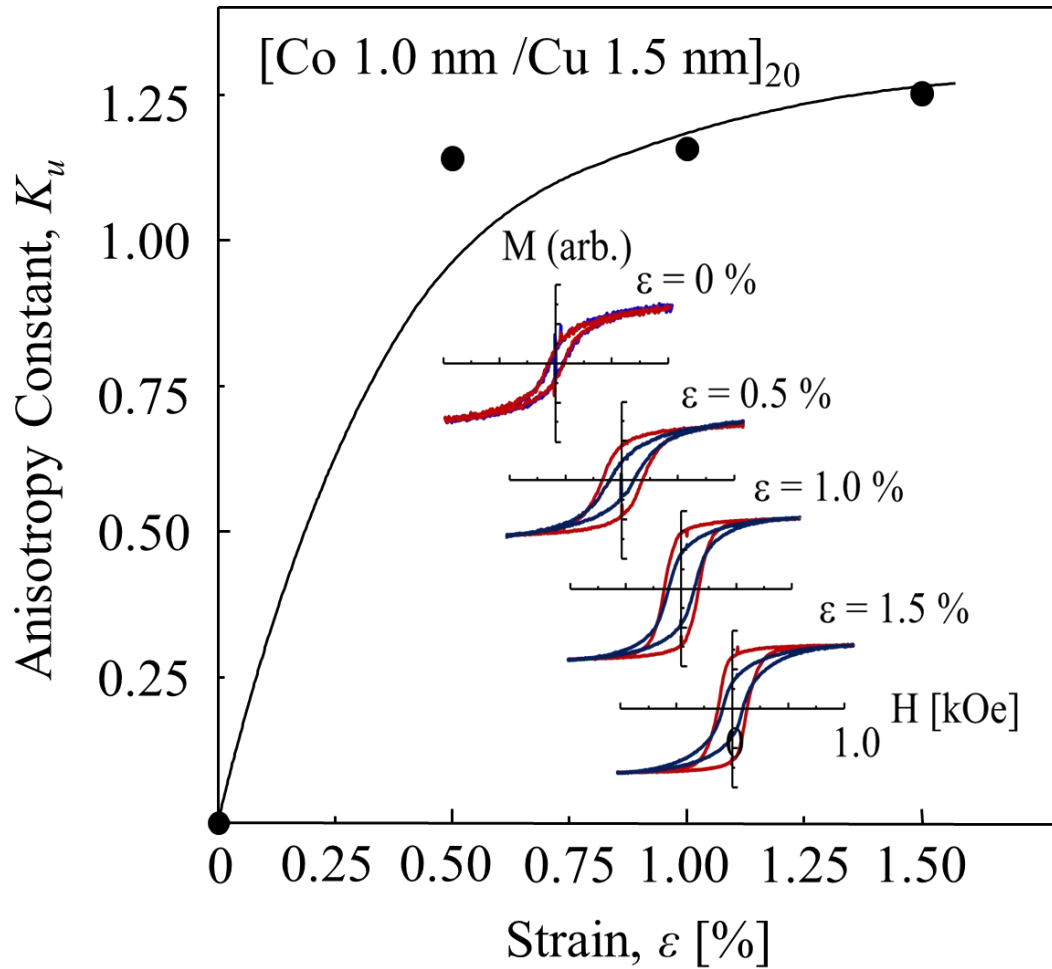


Figure 4-7 Relationship between the magnetic anisotropy constant, K_u , and the induced strain, ε . The inset in it shows magnetization curves at various strain values ($\varepsilon = 0$ to 1.5 %).

4.3.8 Strain and the MR Ratio

Figure 4-8 shows the effect of ε on the MR ratio for the [Co 1.0 nm/Cu 1.5 nm]₂₀ multilayers when (a) $H // \varepsilon$ and $H \perp I$ and (b) $H \perp \varepsilon$ and $H // I$. The result suggests that the MR ratio decreases with increasing ε and the difference in the MR ratio increases with ε for $H \perp I_{e.a.}$ and $H // I_{e.a.}$ ($I_{e.a.}$ refers to the current along the easy axis). Although the MR ratio decreases with the increase in ε , the MR ratio with $H \perp I_{e.a.}$ is always larger than

when $H \parallel I_{e.a.}$, i.e., the MR ratio with $H \parallel \varepsilon$ is more significant than when $H \perp \varepsilon$, and the gap between the two widens as ε increases.

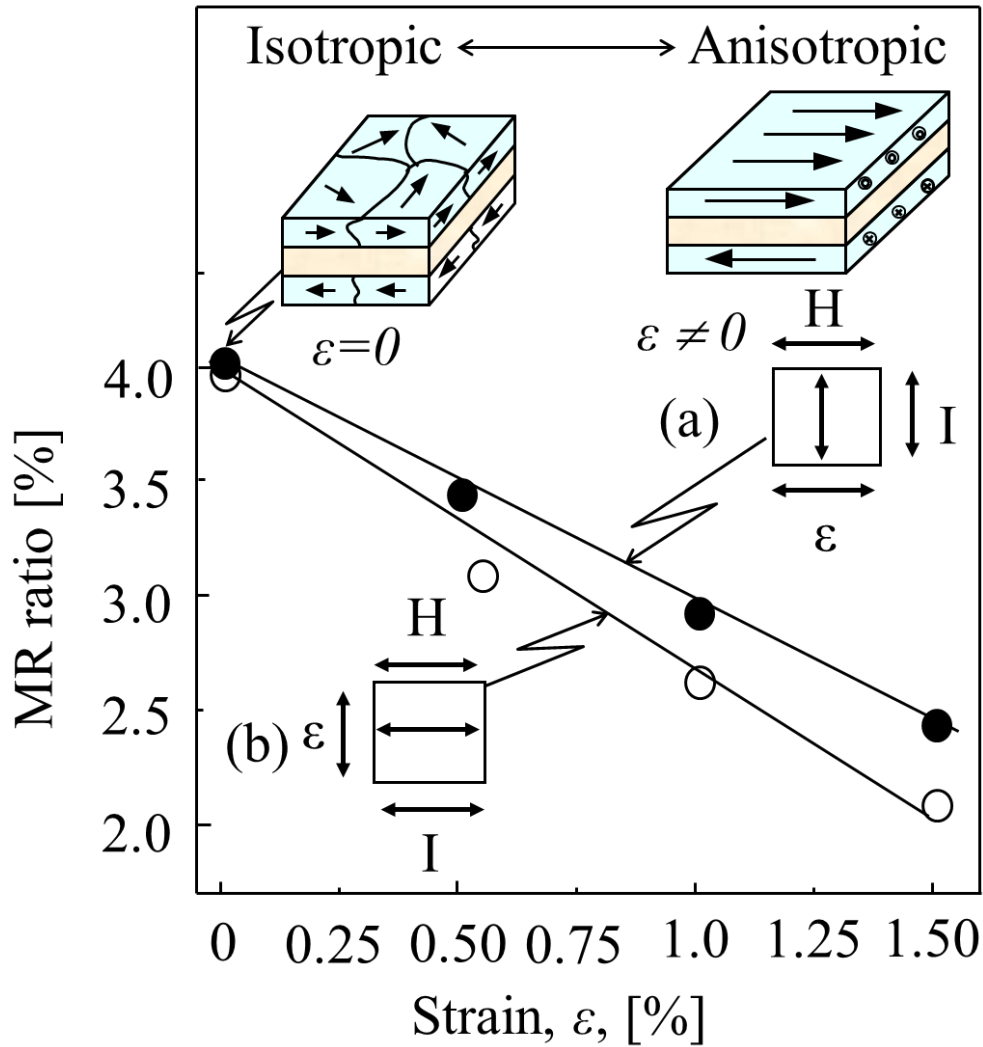


Figure 4-8 Correlation between the MR ratio and strain, ε , (a) closed circles (•): $H \perp I_{e.a.}$ and (b) open circles (o): $H \parallel I_{e.a.}$. Directions of applied magnetic fields, current, and strain are indicated with the corresponding arrows.

The decrease in the MR ratio is in good agreement with the change in strain, as it changes the interfacial states of the layers between the Co and Cu layers, independent of the direction of the current and the applied field. The difference in the MR ratio with the field parallel and perpendicular to strain is considered to be due to the modification of the magnetic states owing to the induced strain at the interface between the layers of Co and Cu. This assumption holds well with our results of K_u versus ε given in Figure 4-7. Similar tendencies were also observed for the electrodeposited Co/Ag multilayers [4].

4.4 Summary

Co/Cu multilayers were grown on polyimide substrates and magnetic anisotropy was induced via strain (similar to Co/Ag multilayers in Chapter 3). The easy axis of magnetization was found to align in a plane perpendicular to the direction of the strain. The field dependence of the MR ratio at low magnetic fields clearly corresponded to the coercive force of the magnetization curves. The MR ratio was studied for various Co layer thicknesses. The increasing and decreasing trends of the MR ratio are found to be similar to that of the Co/Ag multilayers reported earlier, except that the peak of the MR ratio shifted towards the lower Co layer thicknesses.

The effect of strain was then studied on the MR ratio and magnetic properties. The magnitude of the MR ratio was found to be proportional to the induced strain, showing more enhancements for the field perpendicular to the strain than for the parallel case. The MR ratio was found to decrease with increasing strain. However, the MR ratio when the field applied parallel to the hard axis showed larger value than when the field applied parallel to the easy axis. A maximum MR ratio of 4.1 % was observed. These multilayers with their remarkable magnetic anisotropy properties have been considered to have potential for use as magnetic sensors in the automotive [11] and magnetronic industries [131].

Chapter 5: Magnetoresistance Properties of Co-Au Granular Alloy Films¹¹

5.1 Introduction

Co-based granular alloys prepared by special means have been the subject of intense research due to interest in the search for new magnetic materials with novel magnetic properties for potential applications in electronics [110], [131], [132] and in the biomedical industries [133], [134]. Co-Au is an ideal granular alloy system to investigate the effect of nanoparticles on the GMR and saturation magnetization because of the interesting crystalline structures of Co and Au. The equilibrium phase diagram shows that Co and Au are immiscible up to 693 K [114] (the maximum solubility of Co in Au is only 23 *at %* at the eutectic temperature of 1296.5 K). Thus, a mixture of Co and Au phases can exist in equilibrium at room temperature. The experimental evidence has shown that metastable Co-Au alloys can be grown below 673 K [31].

Previous studies have shown GMR values of up to 4.0 % for the as-deposited Co/Au multilayers prepared using pulsed-current deposition [33]. However, for the Co-Au granular alloys, it is not yet fully clear to what extent preparation methods, annealing, and composition have an effect on the ferromagnetic grain sizes, the saturation magnetization, and the MR effect.

In this chapter, we have investigated the composition relationship between the electrolyte and the deposited Co-Au alloys. As the MR and magnetic properties of the Co-Au alloys are influenced by the size of the Co particles and their separation from Au particles, a relationship between the spin-dependent resistivity, the saturation magnetization, and the microstructure of the Co-Au granular alloys has also been investigated as the current density is changed. The maximum MR ratio of the Co-Au alloy deposited at a current density of 5 mA/cm² is 4.5 % at 35 *at %* Co. The magnitude of the GMR was found to be associated with the Co grain sizes. The relationship between the deposition current density and ferromagnetic grain sizes was studied using the X-ray diffraction analysis and the low temperature magnetization measurements.

¹¹ A version of this chapter is published. Reprinted from [7] with permission. © *IJAPM* 2011. Rizal, C., Ueda, Y., and Pokharel, R.K. (2011). Magnetotransport properties of Co-Au granular alloys. *International Journal of Applied Physics and Mathematics*. 3:161-166.

5.2 Experimental Procedure

The films were prepared using computer-controlled pulsed-current deposition on the 15-nm Cu (111) buffer layers, e-beam evaporated on the polyimide substrates. Pulsed-current deposition provides the possibility of simultaneously co-depositing Co and Au, which are normally immiscible, from a single electrolyte. The electrolyte consisted of cobalt sulphate [$\text{CoSO}_4 \cdot 7\text{H}_2\text{O}$], potassium gold cyanide [$\text{KAu}(\text{CN})_2$], sodium citrate [$\text{Na}_3\text{C}_6\text{H}_5\text{O}_7 \cdot 2\text{H}_2\text{O}$], and sodium chloride [NaCl].

In the electrolyte, the composition of Co was changed while keeping the composition of Au constant. In this way, the Co:Au ratio could be varied. The total composition of the electrolyte was varied from 10 to 98 *at %* Co, while keeping the composition of $\text{KAu}(\text{CN})_2$, $\text{Na}_3\text{C}_6\text{H}_5\text{O}_7 \cdot 2\text{H}_2\text{O}$, and NaCl constant. The amount of NaCl and $\text{Na}_3\text{C}_6\text{H}_5\text{O}_7$ was each kept constant to 5 *g/l*. The purpose of adding NaCl was to enhance the conductivity of the electrolyte whereas $\text{Na}_3\text{C}_6\text{H}_5\text{O}_7 \cdot 2\text{H}_2\text{O}$ was added to improve processing conditions and material properties [135].

The temperature of the electrolyte was maintained at 50 ± 1 °C using the temperature-controlled water bath. A pure Co plate was used as the anode with the film as the cathode maintained at a distance of 2 cm. After deposition, films were cleaned using double distilled water and dried, and immediately wrapped up in a paraffin wax paper to avoid from getting oxidized. The composition of Co and Au was determined using the atomic flame emission spectroscopy and verified by energy dispersive X-ray analysis. MR measurements were carried out using the standard four-point probe dc method with an excitation current of 3.0 mA. The probes consisted of alloys of Ni and P (5 – 15 % of phosphorus). The details of the measurement scheme are given in [136], [67]. All of the measured MR values were negative and the absolute values of the transverse MR are presented here.

The pulsed-current was supplied and controlled by a programmable microcomputer. The current density was changed from 0.1 to 5 mA/cm². Only the results of alloy films deposited at the current densities of 1, 3, and 5 mA/cm² are presented here.

X-ray diffraction spectra were obtained from $\theta - 2\theta$ scan using a Rigaku (CuK_α) X-ray diffractometer (the X-ray source, operated at 60 kV and 200 mA, was Cu with a Ni filter). Peak positions with accuracy of ± 0.001 in 2θ scan were thus obtained. Magnetization measurements were carried out using a VSM at room temperature. The saturation magnetization was studied as the composition of Co was changed in the alloy.

Low temperature magnetization measurements on the as-deposited Co-Au alloys were carried out using an rf-SQUID magnetometer. The films were first cooled to 5 K at the applied magnetic field of 50 Oe and then temperature was increased from 5 K to 300 K at a zero magnetic field. The temperature dependence of zero-field-cooled and field-cooled magnetizations for the annealed film was also studied.

5.3 Results and Discussions

In this section, we discuss the effect of current density on the alloy composition, MR, saturation magnetization, and grain sizes of Co and Au in the alloy. We observe that both the deposition current density and annealing have appreciable effect on the GMR, the saturation magnetization, and the grain sizes of Co in the Au matrix.

5.3.1 Compositional Analysis

Figure 5-1 shows a correlation between the Co composition (Co at %) in the electrodeposited film and the Co composition (Co at %) in the electrolyte at the current densities, J , of 1 and 5 mA/cm². The composition relationship between the deposited film and the electrolyte is not linear. Hence, it can be concluded that the deposition is of regular type [137]¹². The less noble element Co is less readily deposited as compared to the more noble element Au. The Co concentration in the deposited film is lower at the lesser concentration of Co in the electrolyte. However, the concentration of Co in the film increases abruptly for electrolyte compositions in excess of 50 at % Co.

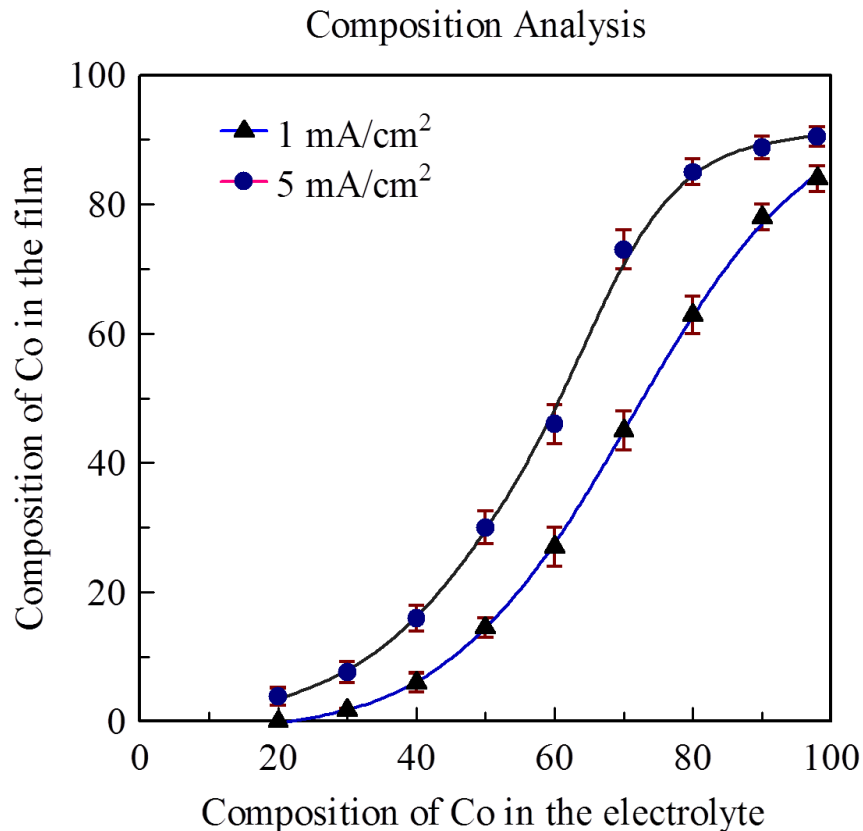


Figure 5-1 Co at % in the alloy vs. Co at % in the electrolyte as the composition of Co in the electrolyte is changed from 10 to 98 at %. Closed triangles (\blacktriangle): $J = 1 \text{ mA/cm}^2$ and closed circles (\bullet): $J = 5 \text{ mA/cm}^2$.

¹² How the data were taken and analysed in this thesis is described in Appendix B.

At the current density of 1 mA/cm^2 , the curve does not saturate even with the increasing Co concentration in the electrolyte. However, at the current density of 5 mA/cm^2 , the concentration of Co in the electrolyte approaches to the concentration of Co in the alloy. As the concentration of the Au atoms was very small in the electrolyte as compared to the concentration of Co atoms, the deposition of the Au atoms seems to be under diffusion control [137]. The inset in Figure 5-1 shows a correlation between the composition of Co in the film and the deposition current density. The composition of Co in the alloy drastically increases with the increase in the current density.

5.3.2 Composition Dependence of the MR Ratio

Figure 5-2 shows the composition (Co at %) dependence of the MR ratio for the Co-Au alloys deposited at the current densities of 1 and 5 mA/cm^2 and measured at room temperature. The maximum MR ratios of the films deposited at 1 and 5 mA/cm^2 are 2 % and 4.5 %, respectively. The peak of the maximum MR ratio shifts slightly towards the lower Co concentrations for the alloy deposited at 5 mA/cm^2 . The maximum MR ratio appears within a narrow concentration range of ferromagnetic atoms (i.e., between 35 and 45 at % Co) for all films.

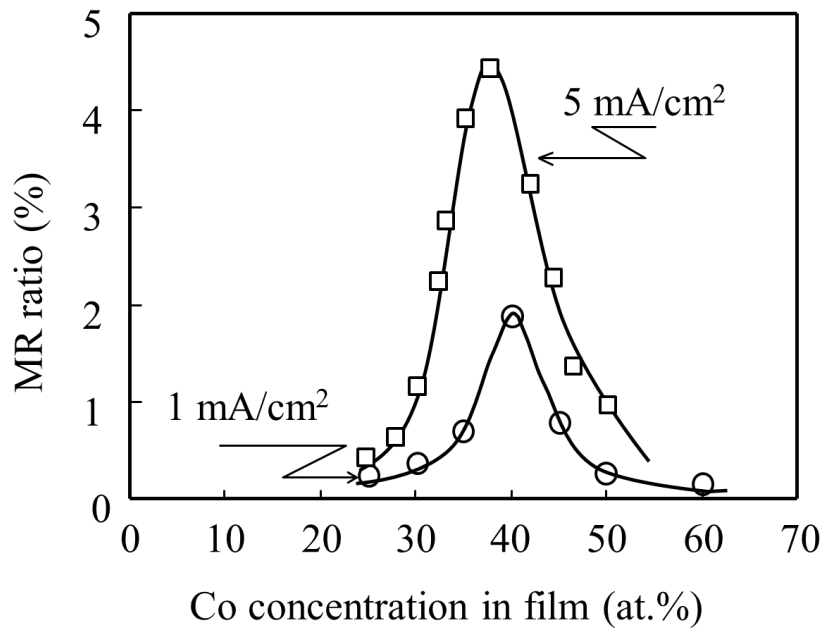


Figure 5-2 The MR ratio versus Co (at %) in the alloy. Open circles (o) and open squares (□) represent MR values at the current densities of 1 and 5 mA/cm^2 , respectively.

The increase in the MR ratio near 30 at % Co seems to be due to the optimum size and distribution of Co grains and inter-granular separation [138], [33]. The low MR values below 30 at % Co can be ascribed to a relatively low concentration of ferromagnetic components leading to fewer magnetic and non-magnetic interfacial scattering sites. The decrease in MR above 45 at % Co seems to be due to the decrease in spin-

dependent scattering of the conduction electrons, which is mainly responsible for the GMR effect [54], [94], [127]. The increase in the MR ratio with the increase in the deposition current density is because of changes in the microstructure of the film [94], [34].

5.3.3 Composition Dependence of the Saturation Magnetization

Figure 5-3 illustrates the dependence of the saturation magnetization, M_s , on the Co concentration in the Co-Au alloy electrodeposited at the current densities of 1 and 5 mA/cm² and annealed. M_s decreases abruptly with decreasing Co concentration for both types of alloys, deviating from the simple dilution law, and vanishing below 30 at % Co. The decrease in M_s with increasing Au concentration is considered to be due to the interaction of the 4-*s* electrons of Au with the 3-*d* electrons of Co as the composition of Au in the alloy is increased. This explanation holds well with the explanation given in [127]. The decreasing trend of M_s with the increasing composition of Au is consistent with the results observed for Ni-Cu and Ni-Zn alloys [127]. Moreover, there is a sharp decrease in M_s with the increase in current density and annealing.

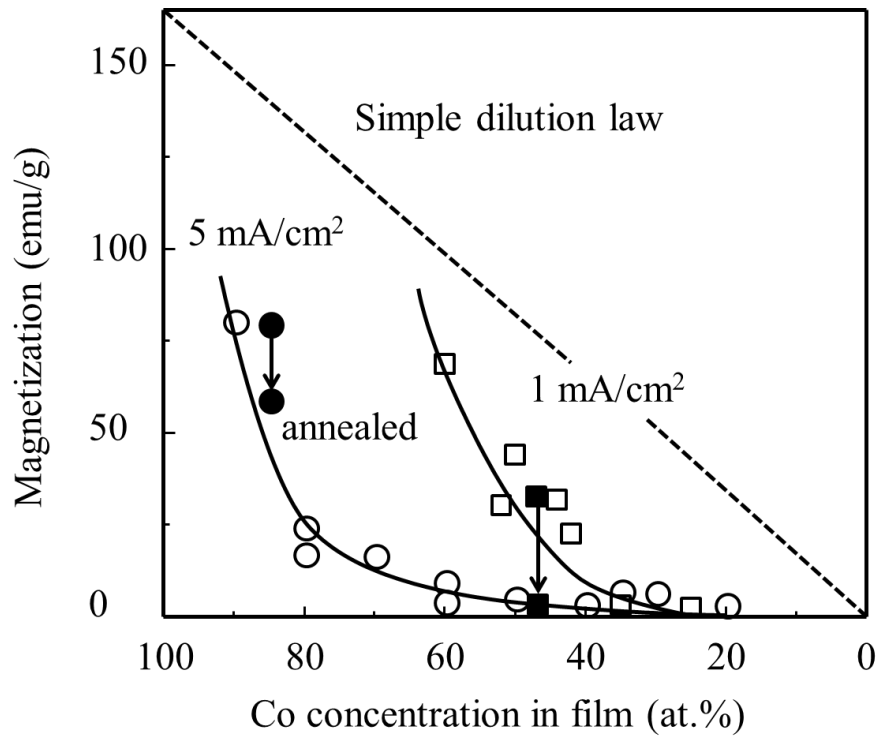


Figure 5-3 Composition dependence of saturation magnetization for the as-deposited and annealed Co-Au alloys. Open squares (□) and open circles (o) represent magnetization for the as-deposited alloy at the current densities of 1 and 5 mA/cm², respectively. Closed squares (■) and closed circles (●) represent magnetization for the annealed alloy.

It seems that the Co-Au alloys electrodeposited at higher current densities either formed smaller grain sizes or solid solution. Similar results have been reported for other ferromagnetic films as well [111], [80]. The

saturation magnetization of Co-Au alloys further decreases with the increase of annealing temperature due to the decrease in Co grain size, the increase in Au grain size, and the change in the separation between the Co grains. The effect of annealing on grain sizes is further discussed in Section 5.3.5.3. The saturation magnetization decreases sharply with increasing Au concentration and vanishes below 30 at % Co. However, the decrease is more abrupt for the alloys deposited at 5 mA/cm² than the alloys deposited at 1 mA/cm².

5.3.4 Microstructural Analysis

X-ray diffraction spectra obtained for Co₃₅Au₆₅ alloy films deposited at the current densities of 1, 3, and 5 mA/cm² are illustrated in Figure 5-4. In this, the prominent broad peak at $2\theta = 44.25^\circ$ corresponds to the (111) fcc-Co crystallites and is less intense compared to the peak due to (111) Au: pure Au (111) and Au (200) peaks are located at $2\theta = 38.2^\circ$ and $2\theta = 44.37^\circ$, respectively. The peak height of Au (111) reduces significantly when the deposition current density is increased to 5 mA/cm² from the applied current density of 1 mA/cm². The peak at $2\theta = 43.25^\circ$ corresponds to the Cu substrate.

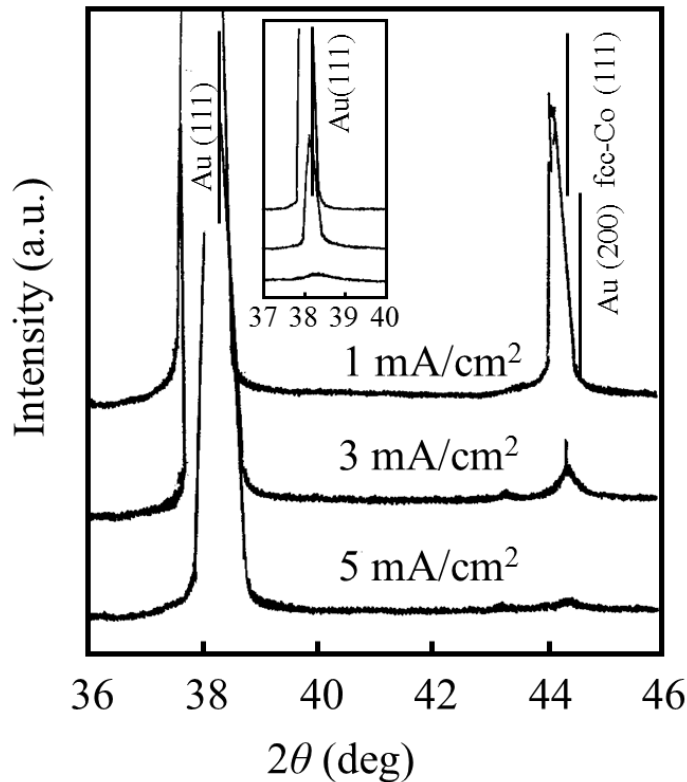


Figure 5-4 X-ray diffraction patterns for the as-deposited Co₃₅Au₆₅ alloys at various current densities (1, 3, and 5 mA/cm²) as the diffraction angle, 2θ is changed from 36 to 46°.

The presence of strong peaks of Au indicates that Au here serves as the film matrix whereas Co grains are dispersed as small clusters throughout the film (the grain size of the Co was determined using a low temperature rf-SQUID magnetization measurement, and is described in Section 5.3.5). This result is consistent with the

recently reported result of Co-Au nanocomposites that shows a clear formation of Co grains, with the diameter in the range of 1- 3.3 nm, dispersed in the Au matrix [31]. The present results are also analogous to the recently reported results of X-ray diffraction analysis, which shows the formation of Au grains in $\text{Co}_{68}\text{Au}_{32}$ granular alloys [132].

5.3.5 Estimation of Cobalt Grain Size

A low temperature magnetization was carried out to investigate the relationship between Co grain sizes and the GMR effect presented in Section 5.3.2. The zero-field-cooled (ZFC) and field-cooled (FC) magnetizations were measured both for the as-deposited and annealed Co-Au alloys.

5.3.5.1 Grain Size Estimation at 3 mA/cm^2 (As-deposited)

Figure 5-5 shows the temperature dependence of the zero-field-cooled (ZFC) and field-cooled (FC) magnetizations for the as-deposited Co-Au alloy at the current density of 3 mA/cm^2 . The as-deposited film shows a broad peak near the temperature of 65 K.

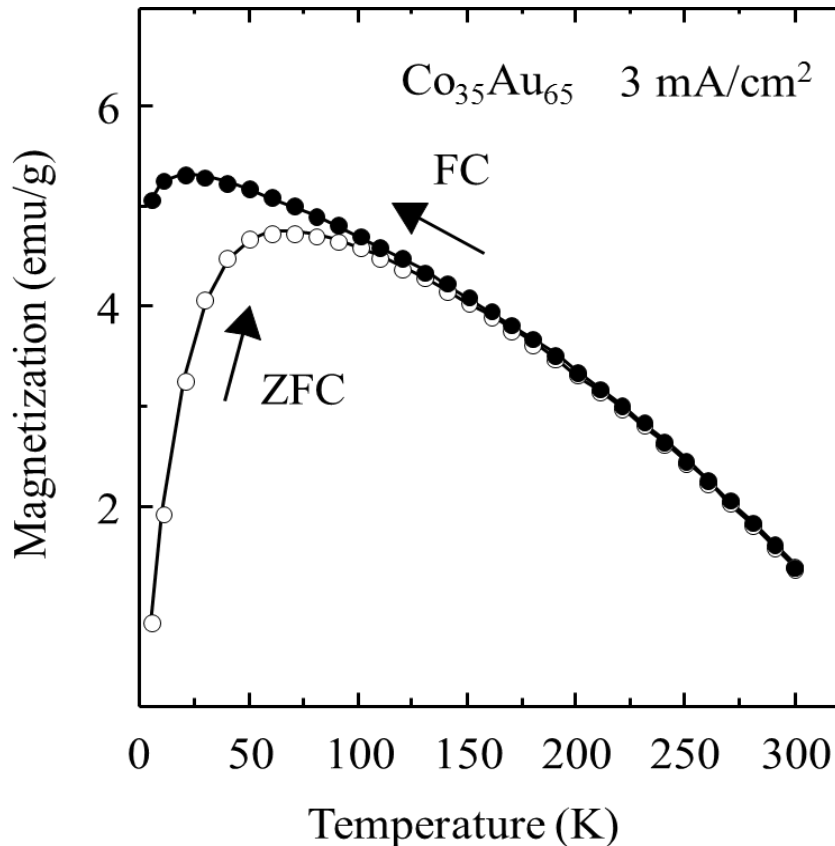


Figure 5-5 Saturation magnetization for the as-deposited $\text{Co}_{35}\text{Au}_{65}$ alloys deposited at 3 mA/cm^2 : closed circles (●) indicate field-cooled (298 K to 5 K at 50 Oe) and open circles (○) indicate zero-field-cooled (5 K to 298 K). ZFC and FC in the diagram represent zero-field-cooled and field-cooled, respectively.

5.3.5.2 Grain Size Estimation at 5 mA/cm² (As-deposited)

Figure 5-6 shows the temperature dependence of the zero-field-cooled (ZFC) and field-cooled (FC) magnetizations for the Co-Au alloy deposited at the current density of 5 mA/cm². The as-deposited film shows a broad peak near the temperature of 45 K. The existence of the peak at the lower temperature suggests the formation of fine ferromagnetic grains.

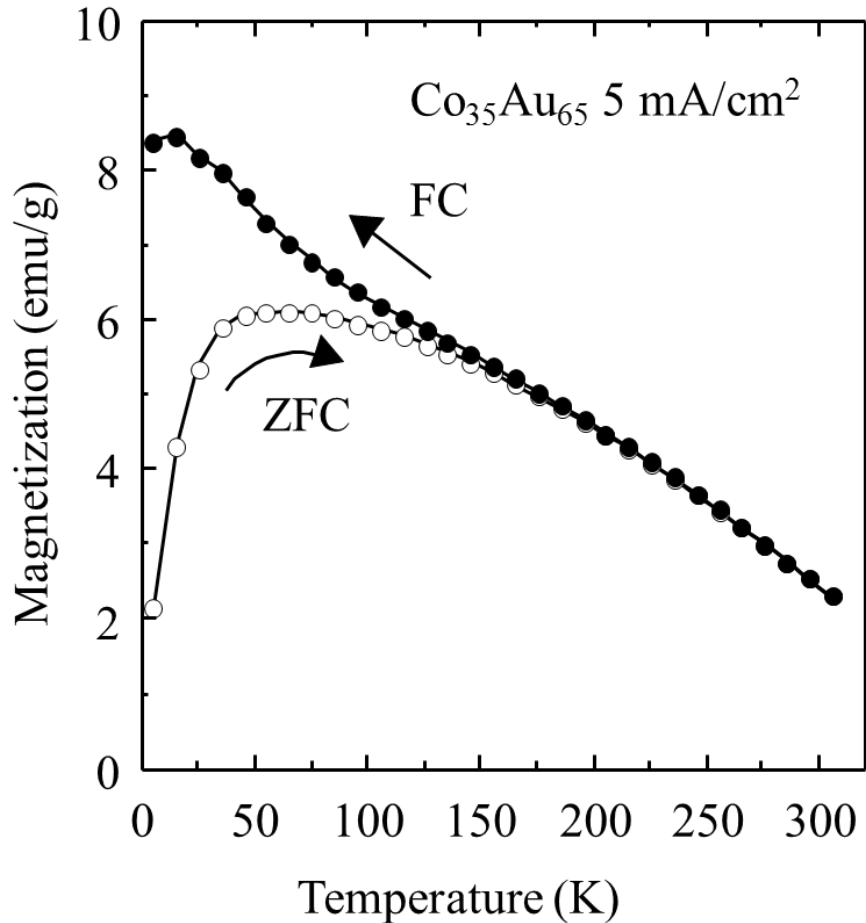


Figure 5-6 Saturation magnetization for the as-deposited Co₃₅Au₆₅ alloy deposited at 5 mA/cm²: closed circles (●) field-cooled (298 K to 5 K at 50 Oe) and open circles (○) zero-field-cooled (5 K to 298 K). ZFC and FC in the diagram represent zero-field-cooled and field-cooled, respectively.

If the peak temperature is the mean blocking temperature observed for super-paramagnetic behavior, the volume of the Co grains in each film can be calculated using (1.41). Given that the Co-rich magnetic grains are present in the matrix as an fcc-phase, and taking K_A for bulk Co equal to 5.5×10^{17} eV/cm³, the grain diameters are 4 nm and 6 nm for the films deposited at the current density of 5 and 3 mA/cm², respectively. It is possible that small Co grains present in the Co-Au films deposited at the higher current density contributed to the larger MR values [138], [31].

5.3.5.3 Grain Size Estimation at 5 mA/cm² (Annealed)

Figure 5-7 shows the temperature dependence of the zero-field-cooled (ZFC) and field-cooled (FC) magnetizations for the Co-Au alloy deposited at the current density of 5 mA/cm² and annealed. Unlike the broad peak observed at 65 K (see Figure 5-5) and 45 K (see Figure 5-6) for the as-deposited films deposited at the current density of 3 and 5 mA/cm², respectively, the peak for the annealed Co-Au alloy deposited at the current density of 5 mA/cm² is not clear. This suggests that the grain sizes of Co in the alloy had a range of blocking temperatures that extended all the way to room temperature. These results are consistent with the results of the low temperature magnetization measured for Co-Cu [44] and Co-Ag [80] films.

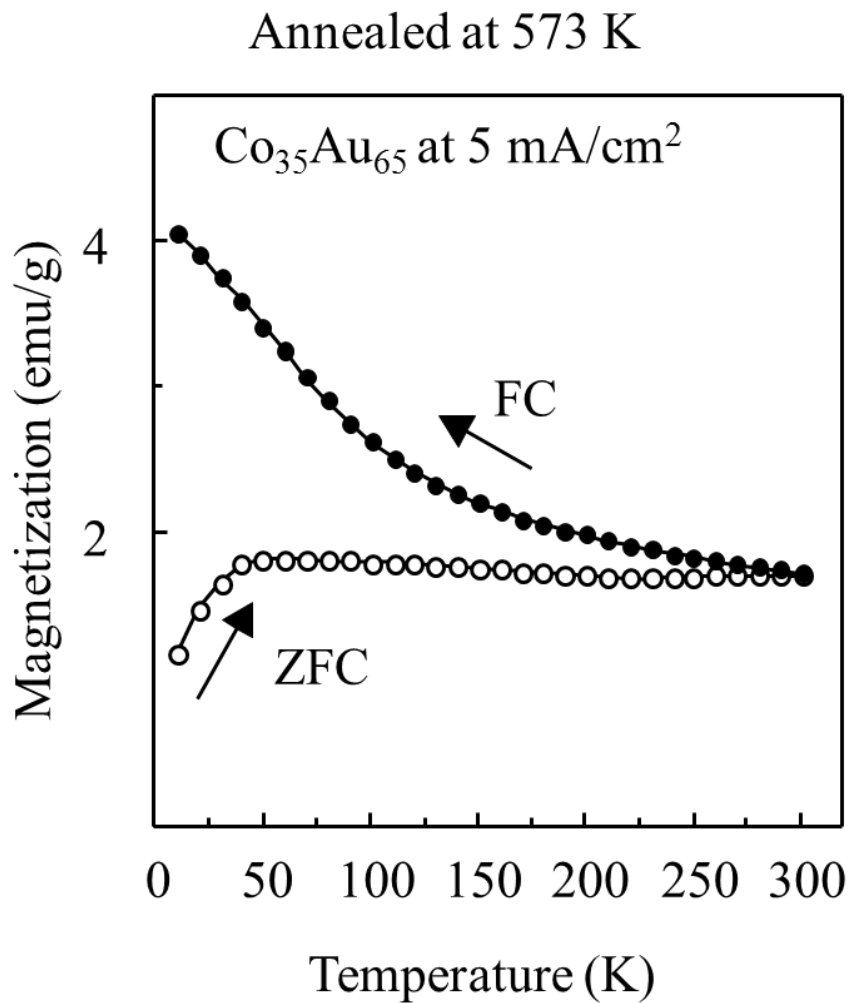


Figure 5-7 Saturation magnetization for the annealed Co₃₅Au₆₅ alloys deposited at 5 mA/cm² and annealed: closed circles (●) indicate field-cooled (298 K to 5 K at 50 Oe) and open circles (○) indicate zero-field-cooled (5 K to 298 K). ZFC and FC in the diagram represent zero-field-cooled and field-cooled, respectively.

5.4 Summary

Co-Au granular alloy films were prepared using computer-controlled pulsed-current deposition. The relationship between the Co composition in the film and the Co composition in the electrolyte, for the alloys deposited at various current densities, was established. The increase in current density resulted in the drastic increase in the composition of Co in the Co-Au alloy. The alloys deposited at higher current densities showed larger MR values. Similarly, the composition dependence of the saturation magnetization was also studied at room and elevated temperatures for various current densities. The maximum MR ratio was observed when the composition of Co was in between 35 and 45 *at %*.

In order to investigate the cause of the increase of MR values with the increase of current density and composition, X-ray diffraction analysis and low temperature magnetization measurements were carried out. X-ray diffraction analysis revealed the presence of strong $\langle 111 \rangle$ Au structures in the alloy. The temperature dependence of zero-field-cooled (ZFC) and field-cooled (FC) magnetizations for both the as-deposited and annealed samples revealed smaller Co particles present in the alloys deposited at higher current densities. Based on the X-ray diffraction and low temperature measurements, it can be concluded that the increase in the MR values was due to the formation of smaller grain sizes in the alloy. These Co-Au alloys are potentially useful for fundamental research in neutron scattering and atom-probe field ion microscopy and also for applications in the automobile sector and the medical field [81].

Chapter 6: Magnetic Properties of FeCo Nanostructures¹³

6.1 Introduction

High-moment nanostructures have been considered to have potential for many technological applications in the electronics and the biomedical sectors [9], [139]. One such example is the use of FeCo nanostructures in the enhancement of the quantum efficiency of organic LEDs [140]. Recent examples of the use of FeCo nanostructures in biomagnetic sensing are available in [9] and [13]. So far, the maximum room temperature saturation magnetization, M_s , reported for Fe₆₀Co₄₀ and Fe₇₅Co₂₅ nanostructures, is 212 emu/g with a coercivity of 200 Oe [38], [39]. However, the information on the actual internal state of the nanostructure, that contributes to the magnetization, has not yet been fully explained, and the question as to how M_s of these nanostructures can be enhanced, remains unanswered.

Usually, FeCo nanostructures have been produced using melt-spun or sputtering methods [139] or polyol process [38]. Pulse electrodeposition method as compared to physical deposition methods is advantageous in the growth of magnetic nanostructures. It is not restricted by the shape of the substrates. By adjusting the width and interval time of a pulsed-current wave, it is possible to produce ferromagnetic nanostructures in various compositions and ratios. The pulsed-current deposition favors the initiation of grain nuclei and greatly increase the number of grains per unit area resulting in finer grained deposits with better physical properties than the nanostructures prepared using constant-current deposition techniques [121].

In this study, Fe/FeCo nanostructures have been produced using pulsed-current deposition by alternately stacking Fe and FeCo in various ratios and compositions. The nanostructures exhibited dramatically high M_s of up to 240 emu/g at room temperature as both the composition of Co in the FeCo layer and the stacking number increased. We have correlated this enhanced saturation magnetization with the lattice constant using magnetization and microstructural studies.

¹³ A version of this chapter is accepted as a conference paper. Reprinted from [8] with permission. © 2012 IEEE. Rizal C., Gyawali, P.R., and Pokharel, R.K. Magnetic and microstructural characterizations of Fe/FeCo nanostructures. *IEEE International Magnetic Conference (Intermag-2012)*, 5/2012.

6.2 Experimental Procedure

In this study, FeCo nanostructures have been prepared in sulphate electrolyte using pulsed-current deposition by reducing the width of the pulsed current. The electrolyte consisted of $\text{FeSO}_4 \cdot 7\text{H}_2\text{O}$, $\text{CoSO}_4 \cdot 7\text{H}_2\text{O}$, $\text{Na}_3\text{C}_6\text{H}_5\text{O}_7 \cdot 2\text{H}_2\text{O}$, and NaCl , with a pH of 6.0. The deposition was carried out on a 15-nm Cu buffer layer grown on a 1.69 cm^2 glass substrate. The current density of the multilayer was varied from 1 to 10 mA/cm^2 . The composition analysis was done using an energy dispersive X-ray analysis. Magnetic properties were studied using a vibrating sample magnetometer and structural analysis was done using X-ray diffraction measurements.

Figure 6-1 (a) (i) shows the cross-sectional view of the pulsed-current (potential) wave used in the experiment and (ii) shows the corresponding FeCo nanostructure. Figure 6-1 (b) shows the same but with the higher stacking number, n . All of the deposited nanostructures have a constant thickness of 300 nm. The total composition of Co and Fe was kept constant by keeping the ratio of Fe and FeCo layers constant. The composition of Fe and Co in the nanostructure was controlled via electrolyte and pulsed-current.

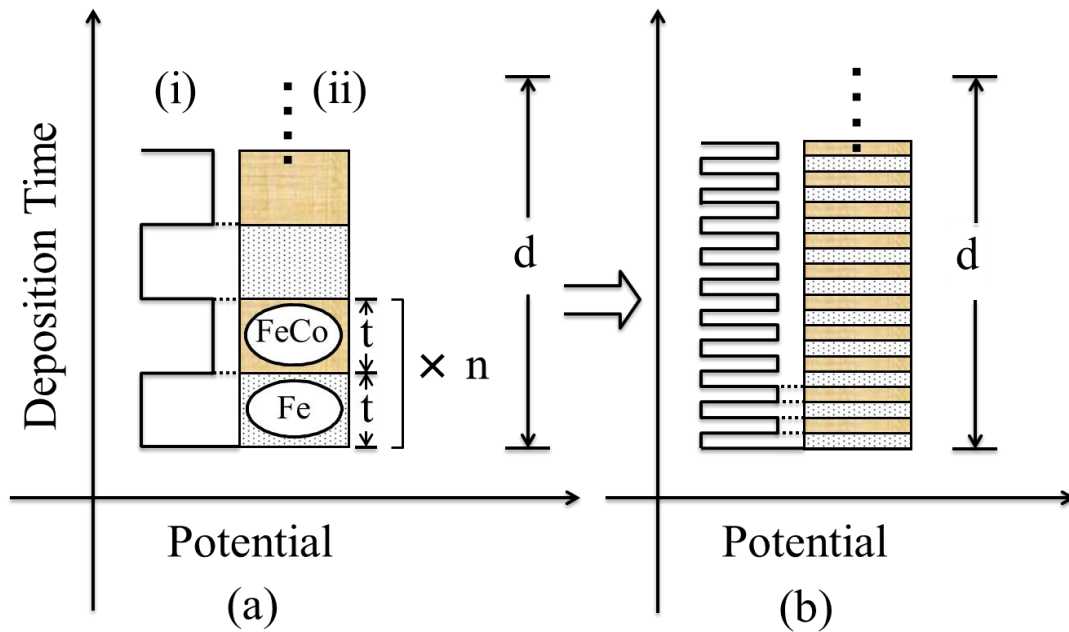


Figure 6-1(a) (i) Deposition time versus potential (corresponding to the pulsed-current) and (ii) cross-section of the nanostructure with the total thickness, d , and (b) shows the same but with a higher stacking number, n .

6.3 Results and Discussions

In Section 6.2, a brief discussion of the preparation of FeCo nanostructures using pulsed-current was discussed. In this section, results of the saturation magnetization and the microstructure of the electrodeposited nanostructures are discussed.

6.3.1 Saturation Magnetization

Figure 6-2 shows the extent to which an atomic composition of Co in the nanostructure has an effect on the saturation magnetization, M_s , when n is changed¹⁴. With increasing n , M_s increases well above the bulk value of both Co and Fe at all compositions. At Co at % 25 and $n = 300$, the nanostructure showed a maximum M_s of 235 emu/g. This increase in M_s with n is considered to be due to the intermixing of atoms at the interface and the formation of a solid solution [136], [92]. The nanostructure exhibited bcc-phase crystal at room temperature. This is further discussed in Section 6.3.2.

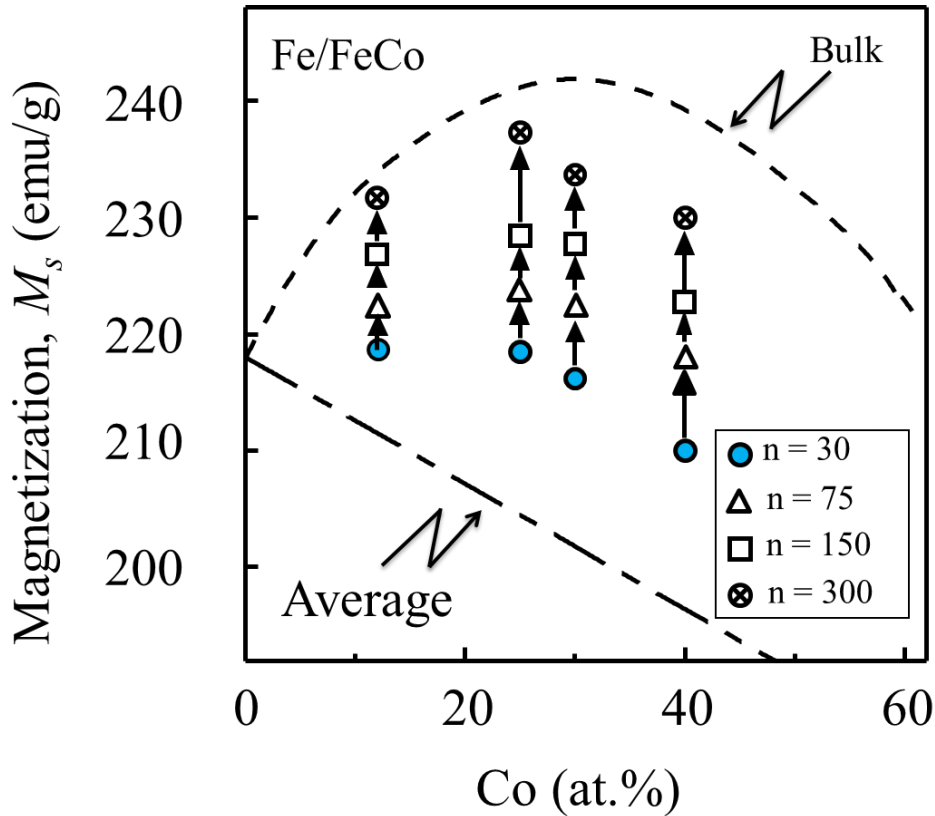


Figure 6-2 Magnetization, M_s , versus Co (at %) in the film as the stacking number, n , is increased from 30 to 300.

6.3.2 Microstructural Analysis

In Section 6.3.1, we reported M_s of the FeCo nanostructure as both the composition and the stacking number were changed. It revealed a maximum M_s of 235 emu/g at Co at % 25 when $n = 300$. In this section, we have investigated the relationship between the values of M_s and lattice constant, as n is increased up to 600, while the composition is fixed at Co at % 25.

¹⁴ How the data were taken and analysed in this thesis is described in Appendix B.

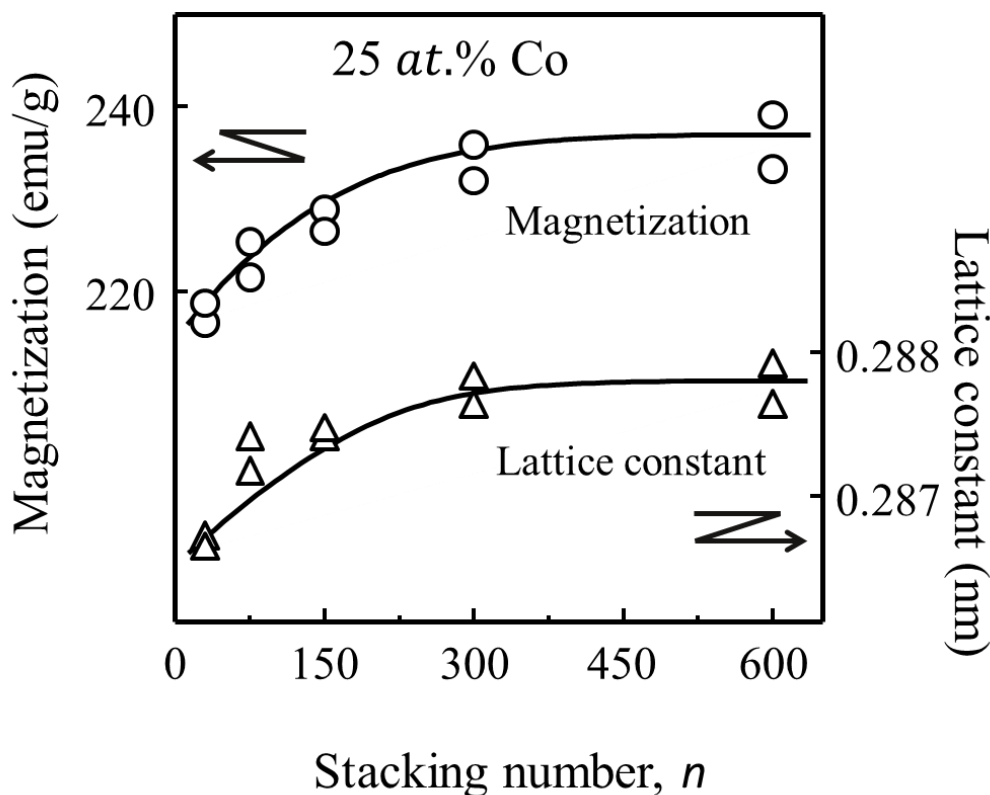


Figure 6-3 (a) Magnetization, M_s , versus stacking number, n : open triangles (Δ): lattice constant and open circles (o): saturation magnetization.

Figure 6-3 shows the values of M_s and lattice constant of the FeCo nanostructure as the stacking number, n , is changed from 0 to 600. With the increase of n , M_s increases to 240 emu/g. Likewise, the lattice constant of the nanostructure also increases. That means, the magnitude of M_s is related to the lattice constant. The increase in M_s with n suggests that Fe and Co likely mixed on the atomic level, giving rise to enhanced magnetic moments.

6.4 Summary

A series of FeCo nanostructures was produced at the atomic scale using pulsed-current deposition. The effect of stacking number on the saturation magnetization and microstructure was investigated. The saturation magnetization was found to be directly proportional to the stacking number. The microstructural analysis revealed that the increase in saturation magnetization is due to the formation of a solid solution, i.e., Fe and Co were mixed on the atomic level. A maximum saturation magnetization of 240 emu/g was observed at the composition of 25 at % Co. These bio-compatible magnetic nanostructures have been considered to have great potentials for use in biomagnetic sensing [9], [12].

Chapter 7: Summary, Conclusions, Potential Applications, and Future Prospects

7.1 Summary

The nanostructures developed in this thesis have been found to exhibit interesting electrical and magnetic properties. For example, the GMR effect in magnetic multilayers is found to be over 4 times larger than the AMR effect at room temperature. In addition, Co/Au multilayers, when deposited at an oblique angle and annealed in a magnetic field, developed strong magnetic anisotropy at low magnetic fields (< 0.5 kOe). Similarly, Co/Cu and Co/Ag isotropic multilayers developed strong magnetic anisotropy at low fields when strain was induced via stress. Similarly, the magnitude of the GMR effect in electrodeposited Co-Au granular alloys is found to be over 2 times larger than the AMR effect. In addition, the GMR effect in electrodeposited granular alloys is found to be larger than the GMR effect in vapor deposited Co/Au multilayers. Through this study, it was found that the GMR effect in Co-Au alloys is inversely related to ferromagnetic grain sizes. Another significant outcome of this thesis was the synthesis of biocompatible FeCo nanoparticles with high saturation magnetization. These GMR sensors and high saturation magnetic moment nanoparticles have significant potential for application in biomagnetic sensing if properly functionalised.

The thesis is presented in a chronological order aimed at improving the state-of-the-art magnetic technology using ferromagnetic hybrid multilayers, alloys, and nanostructures based on the *3-d* transition metals Co and Fe, and the group IB nonmagnetic metals Cu, Ag, and Au. The study begins with the GMR effect and magnetic anisotropy properties in Co/Au multilayers followed by Co/Ag and Co/Cu multilayers, Co-Au granular alloys, and high-moment FeCo nanoparticles.

Additionally, the effect of growth methods on the electrical and the magnetic characteristics has been studied. The influence of the ferromagnetic layer thickness and the embedded nanoparticle size on the GMR

effect and the saturation magnetization has been extensively investigated. The effect of strain on the GMR effect is also investigated.

In Chapter 2, Co/Au multilayers were developed using oblique incidence evaporation and magnetic annealing. The effect of deposition method on the MR behaviour was studied by changing both the nonmagnetic and ferromagnetic layers in the multilayers. Although the GMR effect was found to be low, the multilayers deposited at an oblique angle of 45° and magnetically annealed, exhibited strong magnetic anisotropy at room temperature.

In Chapters 3 and 4, Co/Ag and Co/Cu multilayers were developed using pulsed-current deposition. The effect of strain on magnetic anisotropy is studied. In Chapter 3, Co/Ag multilayers were grown using the pulsed-current deposition. The GMR effect was studied as the ferromagnetic Co layer thickness was changed. The electrodeposited Co/Ag multilayers showed an MR ratio of over 9.1 %. It was found that the overall MR ratio with the field applied parallel to the hard axis (i.e., parallel to strain) is more significant than when the field applied parallel to the easy axis (i.e., perpendicular to strain) for all samples. An investigation of the effect of strain on GMR and magnetic properties revealed that these nanostructures developed magnetic anisotropy for small magnetic fields (< 0.5 kOe) at room temperature. In Chapter 4, Co/Cu multilayers were grown using pulsed-current deposition. The multilayers exhibited GMR effects of up to 4.1 %. The magnitude of the GMR effect was found to be proportional to the induced strain and that the enhancement is higher when the applied magnetic field is perpendicular to the strain. These findings corroborate the results of the Co/Ag multilayers presented in Chapter 3.

In Chapter 5, Co-Au granular alloys were grown to study the relationship between the MR effect, the saturation magnetization, and the grain sizes. The alloys exhibited a maximum MR ratio of 4.5 %. The magnitude of the GMR effect was found to be associated with the Co grain sizes. The relationship between the deposition current density and ferromagnetic grain sizes was studied using the X-ray diffraction analysis and the low temperature magnetization measurement using rf-SQUIDS. The results of this study suggested that a smaller grain size correlates with the larger MR values for these alloys.

In Chapter 6, FeCo nanostructures have been developed with the goal of (a) incorporating the GMR sensors developed in Chapter 2 through 5 and (b) improving the magnetic biosensing scheme.

7.2 Conclusions

As stated in Section 7.1, ferromagnetic nanostructures have the potential to provide the GMR effect in miniaturized sized devices. In addition, unlike the ferromagnetic metals and their alloys which exhibit the AMR effect, the GMR effect exhibited by the multilayers and the alloys is independent of the direction of the applied field and the current. The work presented in this thesis reveals several important properties of ferromagnetic multilayers, granular alloys, and nanoparticles based on ferromagnetic Co and Fe and nonmagnetic Cu, Ag, and Au metals, that will be very important when designing future magnetic devices because of the following facts:

- (1) Ferromagnetic multilayers exhibited the GMR effect of up to 2.1 % (Co/Au), 4.1 % (Co/Cu), and 9.1% (Co/Ag) and developed strong magnetic anisotropy for small applied magnetic fields (< 0.5 kOe) at room temperature when deposited at an oblique angle (Co/Au) for vapor deposited multilayers and when strain was induced (Co/Ag, Cu) for electrodeposited multilayers.
- (2) The ferromagnetic Co-Au granular alloys have been prepared using pulsed-current deposition. The MR ratio and the grain size in the film are largely dependent on the current density. The maximum MR ratio of the Co-Au alloy deposited at a current density of 5 mA/cm^2 is 4.5 % at 35 at % Co. A low temperature measurement suggested the formation of fine grains exhibiting super-paramagnetic behavior. The presence of small Co grains contributed to the larger MR values for these films. The temperature dependence of the magnetization suggested that a decrease in magnetization correlates with the size and distribution of the Co grains in the Au matrix.
- (3) Square shaped and high magnetic-moment FeCo nanostructures developed in this thesis have been considered to have potential as bimolecular labels due to their comparable size to biomolecules [9].

These physical properties have further opened up a wide range of applications in magnetic industry.

7.3 Potential Applications

The GMR sensing principle has been used as a read head sensor in computers. It has significantly improved the storage density of the hard disk drives. Upcoming application of the GMR sensing is extending to the high speed high density MRAM memory.

The use of GMR sensors is growing in automotive applications such as robotics, automation control, and detection of incremental increase of speed and position due to their high sensitivity and small size. Due to the strong magnetic anisotropy and small coercivity at room temperature, in many ways, multilayers prepared in this thesis make them strong candidates for the sensor application that can replace AMR sensors, currently in use in the automotive sector.

Another promising use of the ferromagnetic nanostructures is emerging in the biomedical sectors [2], [41]. In order to use magnetic sensors in magnetic biosensing, the MR effect of these sensors need to be improved above 10 % [12]. Then these sensors could be used in the early disease detection. Recently, researchers in the USA have developed GMR chips for biomagnetic sensing using FeCo magnetic nanostructures as biomolecular labels (nanotags) and GMR sensors [141], [13]. The GMR sensors developed in this thesis have potential to integrate with the high-saturation magnetization nanoparticles and the cancer biomarker to detect the early symptoms.

Other potential use of GMR sensors is in the position detection. In this case, permanent magnetization patterns can be attached to the object that has to be detected. The attached sensor can detect the changes in the field as a result of object displacement. Other areas where GMR sensors can be applied include quantum configurable logic devices, etc., [142].

7.4 Future Prospects

Nowadays, GMR sensors based on ferromagnetic multilayers are continuously gaining interest for industrial applications as they offer some intrinsic advantages such as small sizes and large MR effects at small magnetic fields over Hall effect or AMR sensors. The room temperature sensitivity of GMR sensors is also much larger than the sensitivity of Hall effect or AMR sensors. With the constant improvement in state-of-the-art processing and manufacturing capabilities, the sensitivity of these multilayers is expected to rise further.

Co-Au granular alloys developed in this thesis have exhibited superparamagnetic-like behaviors. The alloys deposited at the higher current densities are found to contain smaller Co grain sizes. These grains are highly conducive to molecular binding processes free of magnetic agglomeration. These kinds of behaviors make them suitable for applications in many technological fields [11], [13]. One area where these super-paramagnetic like grains have potential for use is biomagnetic sensing [9], [12].

All of the results presented in this thesis lay out the basis for developing magnetronic and biomagnetic technologies to be used in improving the early detection and treatment of various chronic diseases. To realize the potential that ferromagnetic hybrid nanostructures have for developing magnetronic and biomagnetic technologies, collaboration between electrical engineers, physicists, and biologists and/or chemists is necessary.

The pulsed-current deposition that was used in this thesis can be extended to deposit magnetic nanowires in complex geometries that are not usually possible via sputtering, molecular beam epitaxy, or e-beam evaporation methods. Similarly, the magnetic anisotropy studies carried out in this thesis can be extended to granular alloys, nanoparticles, and multilayer systems that have not been covered in this thesis but deserve consideration in the future.

References

- [1] J. M. D. Coey, *Magnetism and Magnetic Materials*. Cambridge: Cambridge University Press, 2010. Ch.15.
- [2] Y. Jing, S. He, T. Kline, Y. Xu and J. P. Wang, "High-magnetic-moment nanoparticles for biomedicine," in *IEEE Annual International Conference: Engineering in Medicine and Biology Society (EMBC 2009)*. 2009, pp. 4483-4486.
- [3] C. Rizal, "Study of magnetic anisotropy and magnetoresistance effects in ferromagnetic Co/Au multilayer films prepared by oblique incidence evaporation method," *J. Magn. Magn. Mater.*, vol. 310, pp. e646-e648, 2007.
- [4] C. Rizal and Y. Ueda, "Magnetoresistance and magnetic anisotropy properties of strain-induced Co/Ag multilayer films," *IEEE Trans. Magn.*, vol. 45, pp. 2399-2404, 2009.
- [5] C. Rizal, "Magnetoresistance and magnetic properties of Co(t_{Co})/Cu multilayer films," *IEEE Trans. Magn.*, vol. 46, pp. 2394-2396, 2010.
- [6] C. Rizal, P. Gyawali, I. Kshatry and R. K. Pokharel, "Strain-induced magnetoresistance and magnetic anisotropy of Co/Cu multilayers," *J. Appl. Phys., American Institute of Physics*, vol. 111, pp. 07C107, 2012.
- [7] C. Rizal, Y. Ueda and R. K. Pokharel, "Magnetotransport properties of Co-Au alloys," *Int. J. of Appl. Phys. and Math.*, vol. 1, pp. 161-166, 2011.
- [8] C. Rizal, P. R. Gyawali and R. K. Pokharel, "Magnetic and microstructural properties of FeCo nanostructures." in *IEEE International Magnetic Conference (Intermag 2012)*, Vancouver, BC, May 7-12, 2012, pp. 1-2 (accepted).
- [9] B. Srinivasan, Y. Li, Y. Jing, Y. H. Xu, X. Yao, C. Xing and J. P. Wang, "A detection system based on giant magnetoresistive sensors and high-moment magnetic nanoparticles demonstrates zeptomole sensitivity: Potential for personalized medicine," *Angewandte Chemie Inter. Ed.*, vol. 48, pp. 2764-2767, 2009.
- [10] E. I. Cooper, C. Bonh, J. Heidmann, Y. Hsu, P. Kern, J. W. Lam, M. Ramasubramanian, N. M. Robertson, L. T. Romankiw and H. Xu, "Recent developments in high-moment electroplated materials for recording heads." *IBM J. Res. Dev.*, vol. 49, pp. 103-126, 2005.
- [11] M. H. Kang, B. W. Choi, K. C. Koh, J. H. Lee and G. T. Park, "Experimental study of a vehicle detector with an AMR sensor," *Sens. Actuat. A: Phys.*, vol. 118, pp. 278-284, 2005.
- [12] S. X. Wang and G. Li, "Advances in giant magnetoresistance biosensors with magnetic nanoparticle tags: Review and outlook," *IEEE Trans. Magn.*, vol. 44, pp. 1687-1702, 2008.
- [13] Y. Li, B. Srinivasan, Y. Jing, X. Yao, M. A. Hugger, J. P. Wang and C. Xing, "Nanomagnetic competition assay for low-abundance protein biomarker quantification in unprocessed human sera," *J. Am. Chem. Soc.*, vol. 132, pp. 4388-4392, 2010.
- [14] T. McGuire and R. Potter, "Anisotropic magnetoresistance in ferromagnetic 3-d alloys," *IEEE Trans. Magn.*, vol. 11, pp. 1018-1038, 1975.
- [15] M. Viret, D. Vignoles, D. Cole, J. M. D. Coey, W. Allen, D. S. Daniel and J. F. Gregg, "Spin scattering in ferromagnetic thin films," *Phys. Rev. B*, vol. 53, pp. 8464-8468, 1996.

- [16] S. S. P. Parkin, "Giant magnetoresistance in magnetic nanostructures," *Annu. Rev. Mater. Sci.*, vol. 25, pp. 357-388, 1995.
- [17] E. T. Papaioannou, V. Karoutsos, M. Angelakeris, O. Valassiadis, P. Fumagalli, N. K. Flevaris and P. Pouloupoulos, "Magnetic, magneto-optic and magnetotransport properties of nanocrystalline Co/Au multilayers with ultrathin Au interlayers." *J. Nanosci. Nanotechnol.*, vol. 8, pp. 4323-4327, 2008.
- [18] H. Zaman, A. Yamada, H. Fukuda and Y. Ueda, "Magnetoresistance effect in Co-Ag and Co-Cu alloy films prepared by electrodeposition," *J. Electrochem. Soc.*, vol. 145, pp. 565-568, 1998.
- [19] L. Albin, G. Carlotti, G. Gubbiotti, L. Pareti, G. Socino and G. Turilli, "Effect of annealing on the magnetic properties of sputtered Co/Cu multilayers," *J. Magn. Magn. Mater.*, vol. 198, pp. 363-365, 6/1, 1999.
- [20] M. Shima, L. G. Salamanca-Riba and T. P. Moffat, "Correlation between structural imperfection and giant magnetoresistance in electrodeposited Co/Cu multilayers," *J. Electrochem. Soc.*, vol. 148, pp. 518-523, 2001.
- [21] Y. Ueda, T. Houga, H. Zaman and A. Yamada, "Magnetoresistance effect of Co-Cu nanostructures prepared by electrodeposition method," *J. Solid. Stat. Chem.*, vol. 147, pp. 274-280, Oct, 1999.
- [22] K. Suenaga, G. Oomi, Y. Uwatoko, K. Saito, K. Takahashi and H. Fujimori, "Study of strain and giant magnetoresistance of Co/Cu magnetic multilayers," *J. Phys. Soc. Jpn.*, vol. 75, pp. 74715-1-74715-5, 2006.
- [23] M. A. M. Gijs and G. E. W. Bauer, "Perpendicular giant magnetoresistance of magnetic multilayers," *J. Adv. Phys.*, vol. 46, pp. 285, 1997.
- [24] Z. J. Yang and M. R. Scheinfein, "Interfacial-roughness effects on giant magnetoresistance and interlayer coupling in Co/Cu superlattices," *Physical Review B*, vol. 52, pp. 4263-4274, 1995.
- [25] U. Hartmann, Ed., Berlin, Heidelberg: Springer Series in Surface Sciences, 2000. Ch.4, pp. 69-73
- [26] Y. Liu, Z. S. Shan and D. J. Sellmyer, "Nanostructure and magnetic anisotropy of Co/Au multilayers," *J. Appl. Phys.*, vol. 81, pp. 5061-5063, 1997.
- [27] K. Yasuhiro, H. Yoshitaka, T. Kingetsu and Y. Masahiko, "In situ observation of epitaxial growth of [Au/Co/Cu] and [Cu/Co/Au] superlattices and their magnetic interface anisotropies," *J. Appl. Phys.*, vol. 90, pp. 5104-5110, 2001.
- [28] P. Morrow, X. T. Tang, T. C. Parker, M. Shima and G. C. Wang, "Magnetoresistance of oblique angle deposited multilayered Co/Cu nanocolumns measured by a scanning tunnelling microscope," *J. Nanotech.*, vol. 19, pp. 1-9, 2008.
- [29] W. Schwarzacher and D. S. Lashmore, "Giant magnetoresistance in electrodeposited films," *IEEE Trans. Magn.* 32(4), pp. 3133-3153, 1996.
- [30] L. Peter, A. Cziraki, L. Pogany, Z. Kupay, I. Bakonyi, M. Uhlemann, M. Herrich, B. Arnold, T. Bauer and K. Wetzig, "Microstructure and giant magnetoresistance of electrodeposited Co-Cu/Cu multilayers," *J. Electrochem. Soc.*, vol. 148, pp. c168-c176, 2001.
- [31] Z. Guo, M. Moldovan, D. Young, L. Henry and E. J. Podlahad, "Magnetoresistance and annealing behaviors of particulate Co-Au nanocomposites," *Electrochem. Solid-State Lett.*, vol. 10, pp. e31-e35, 2007.

- [32] S. Valizadeh, E. B. Svedberg and P. Leisner, "Electrodeposition of compositionally modulated Au/Co alloy layers," *J. Appl. Electrochem.*, vol. 32, pp. 97-104, 2002.
- [33] C. Rizal, A. Yamada, Y. Hori, S. Ishida, M. Matsuda and Y. Ueda, "Magnetic properties and magnetoresistance effect in Co/Au, Ag nano-structure films produced by pulse electrodeposition," *Phys. Stat. Solidi C: Conf.*, vol. 1, pp. 1756-1759, 2004.
- [34] C. Rizal, "Effect of deposition current density on the magnetoresistance, magnetic and microstructure of the CoAu nanostructures," in *2nd International Conference on Nanotechnology: Fundamentals and Applications*, Ottawa, July 2011, pp. 291:1-291:7.
- [35] M. Senda and Y. Nagai, "Magnetic properties of Fe/Co, Fe/CoFe, and (Fe/Co)/SiO₂ multilayer films," *J. Appl. Phys.*, vol. 65, pp. 3151-3156, 1988.
- [36] Y. Ding, J. H. Judy and J. P. Wang, "Magneto-resistive read sensor with perpendicular magnetic anisotropy," *IEEE Trans. Magn.*, vol. 41, pp. 707-712, 2005.
- [37] S. J. Lloyd and J. M. Molina-Aldareguia, "Multilayered materials: A palette for the materials artist," *Phil. Trans. R. Soc. Lond. A*, vol. 361, pp. 2931-2949, 2003.
- [38] Z. J. Huba, K. J. Carroll and E. E. Carpenter, "Synthesis of high magnetization FeCo alloys prepared by a modified polyol process," *J. Appl. Phys.*, vol. 109, pp. 07B514-07B514-3, 2011.
- [39] Q. Nguyen, C. N. Chinnasamy, S. D. Yoon, S. Sivasubramanian, T. Sakai, A. Baraskar, S. Mukerjee, C. Vittoria and V. G. Harris, "Functionalization of FeCo alloy nanoparticles with highly dielectric amorphous oxide coatings," *J. Appl. Phys.*, vol. 103, pp. 07D532-07D532-3, 2008.
- [40] Y. Xu and J. Wang, "FeCo-au core-shell nanocrystals," *Appl. Phys. Lett.*, vol. 91, pp. 233107,12/ 3/2007.
- [41] Y. H. Xu, J. Bai and J. Wang, "High-magnetic-moment multifunctional nanoparticles for nanomedicine applications," *J Magn Magn Mater*, vol. 311, pp. 131-134, 4, 2007.
- [42] Y. Ueda, N. Hataya and H. Zaman, "Magnetoresistance effect of Co/Cu multilayer film produced by electrodeposition method," *J. Magn. Magn. Mater.*, vol. 156, pp. 350-352, 4/2, 1996.
- [43] A. Yamada, M. Shirota, T. Houga and C. Rizal, "Electric and magnetic properties of Fe-Ni based particle and multilayer films produced by pulse control electrodeposition method," *Jpn. Inst. Metals*, vol. 66, pp. 869-872, 2002.
- [44] T. Houga, H. Zaman, S. Chikazawa, "Magnetism and magnetoresistance effect in the Co-Cu and Co-Ag films produced by pulsed-current deposition," in *IEEE International Magnetism Conference*, Korea, 1999, 1 page.
- [45] H. Zaman, S. Ikeda and Y. Ueda, "Magnetoresistance in Co-Ag multilayers and granular films produced by electrodeposition method," in *Digest of the IEEE International Magnetism Conference*, 1997, pp. BQ:04-BQ:04.
- [46] C. Rizal "Pulse electrodeposition of Co/Au multilayers and granular alloys," *Jpn. J. Appl. Surf. Fin. Soc.*, vol. 55, pp. 83-84, 2004.
- [47] A. Yamada, T. Houga and Y. Ueda, "Magnetism and magnetoresistance of Co/Cu multilayer films produced by pulse control electrodeposition method," *J. Magn. Magn. Mater.*, vol. 239, pp. 272-275, 2002.

- [48] K. Wasa, M. Kitabatake, H. Adachi and H. Makoto, *Thin Film Materials Technology*. Burlington: William Andrew, Inc., 2004.
- [49] M. Freeman, "Nanomagnetism: a case history of nanoscience and technology," *The Physics Teacher*, vol. 47, pp. 206, 2009.
- [50] W. Thomson, "On the electro-dynamic qualities of metals: effects of magnetization on the electric conductivity of nickel and iron," *Proc. Royal Soc. of London*, vol. 8, pp. 546-550, 1857.
- [51] N. H. Mott, "The electrical conductivity of transition metals," *Proc. Roy. Soc. A*, vol. 153, pp. 699-706, 1936.
- [52] J. Smith, "Magnetoresistance of ferromagnetic metals and alloys at low temperatures," *Physica*, vol. 17, pp. 612-627, 6, 1951.
- [53] H. Jaeger, D. Haviland, B. Orr and A. Goldman, "Onset of superconductivity in ultrathin granular metal films," *Phys. Rev. B*, vol. 40, pp. 182, 1989.
- [54] I. Inoue, A. Oguri and S. Maekawa, "Theory of giant magnetoresistance in metallic superlattices," *J. Phys. Soc. Jpn.* 60, pp. 376-385, 1991.
- [55] F. Petroff, A. Barthélémy, A. Hamzić, A. Fert, P. Etienne, S. Lequien and G. Creuzet, "Magnetoresistance of Fe/Cr superlattices," *J. Magn. Magn. Mater.*, vol. 93, pp. 95-100, 2, 1991.
- [56] B. A. Jones and C. Hanna, "Contribution of quantum-well states to the RKKY coupling in magnetic multilayers," *Phys. Rev. Lett.*, vol. 71, pp. 4253-4256, 1993.
- [57] D. A. Eastham, Y. Qiang, T. H. Maddock, J. Kraft, J. P. Schille, G. S. Thompson, H. Haberl and A. J. P. Andres, "Quenching of ferromagnetism in Co clusters embedded in Cu," *J. Phys. : Condens. Matter*, vol. 9, pp. L497, 1997.
- [58] J. Kondo, "Resistance minimum in dilute magnetic alloys," *Progress of Theoretical Physics*, vol. 32, pp. 37-49, 1964.
- [59] I. Bakonyi and L. Peter, "Electrodeposited multilayer films with giant magnetoresistance (GMR): Progress and Problems," *Progress in Materials Science*, vol. 55, pp. 107-245, 2010.
- [60] E. Ferrari, F. Da Silva and M. Knobel, "Theory of giant magnetoresistance in granular alloys," *Phys. Rev. B*, vol. 59, pp. 8412, 1999.
- [61] A. Fert and L. Piraux, "Magnetic nanowires," *J. Magn. Magn. Mater.*, vol. 200, pp. 338-358, 10, 1999.
- [62] M. N. Baibich, J. M. Broto, A. Fert, F. N. Van Dau, F. Petroff, P. Etienne, G. Creuzet, A. Friederich and J. Chazelas, "Giant magnetoresistance of (001)Fe/(001)Cr magnetic superlattices," *Phys. Rev. Lett.*, vol. 61, pp. 2472, 1988.
- [63] S. S. P. Parkin, "Giant magnetoresistance in magnetic multilayers and granular alloys," *Mater. Lett.*, vol. 20, pp. 1-4, 1994.
- [64] S. S. P. Parkin, N. More and K. P. Roche, "Oscillations in exchange coupling and magnetoresistance in metallic superlattice structures: Co/Ru, Co/Cr, and Fe/Cr," *Phys. Rev. Lett.*, vol. 64, pp. 2304-2308, 1990.

- [65] C. Rizal and B. Karki, "Magnetic properties of Fe/Cu multilayers prepared using pulsed-current deposition," in *Proceedings: 1st International Conference on Nanomaterials: Applications and Properties, Alushta, Crimea*, 2011, pp. 27-30.
- [66] Y. Harada, Y. Nakanishi, N. Yoshimoto, A. Yamaguchi, M. Nakamura and M. Yoshizawa, "Structural and magnetic properties of epitaxial Fe/Cu multilayers," *J. Magn. Magn. Mater.*, vol. 272, pp. e969-e970, 2004.
- [67] C. Rizal, "Magnetotransport properties of Co/Cu multilayer films," in *Joint Intermag-MMM Conference*, Washington DC, USA, 2010, pp. 1-1.
- [68] C. Rizal, I. B. Chhetry, P. R. Gywali and R. K. Pokharel, "Effect of strain on the magnetoresistance effect and magnetic properties of Co/Ag nanostructures grown using pulsed-current electrodeposition," in *IEEE Nanotechnology Materials and Devices (NMDC-2011)*, The Shila Jeju, Korea, 2011. 5 pages.
- [69] M. Velez and I. K. Schuller, "Sputtering pressure effect on the giant magnetoresistance of Fe/Cr superlattices," *J. Magn. Magn. Mater.*, vol. 184, pp. 275-280, 5/5, 1998.
- [70] R. Ciprian, M. Carbuicchio and G. Palombarini, "Interface phenomena and magnetic properties of Fe/Cr multilayers," *IEEE Trans. Magn.*, vol. 46, pp. 432-435, 2010.
- [71] Y. Ueda, S. Ikeda, S. Hama and A. Yamada, "Magnetic properties and magnetoresistance of Fe/Cr multilayer films prepared by vapor deposition and electrodeposition," *J. Magn. Magn. Mater.*, vol. 156, pp. 353-354, 1996.
- [72] Y. Kobayashi, H. Sato, Y. Aoki and A. Kamijo, "The giant magnetoresistance and the anomalous hall effect in molecular-beam-epitaxy grown Co/Cu superlattices," *J. Phys.: Cond. Matter.*, vol. 6, pp. 7255, 1994.
- [73] E. A. M. van Alphen and W. J. M. deJonge, "Granular Co/Ag multilayers: Relation between nanostructure, and magnetic and transport properties," *Phys. Rev. B*, vol. 51, pp. 8182-8192, 1995.
- [74] S. Araki, "Magnetism and transport properties of evaporated Co/Ag multilayers," *J. Appl. Phys.*, vol. 73, pp. 3910-3916, 1993.
- [75] V. K. Sankaranarayanan, O. Prakash and S. T. Lakshmikumar, "Investigation of Co/Ag discontinuous multilayers prepared by UHV electron beam evaporation," *J. Surf. Sci. Tech.*, vol. 22, pp. 15, 2006.
- [76] C. Christides, "Strong interplay between giant and anisotropic magnetoresistance observed in face-centered-cubic-Co/Au multilayers between 5 and 280 K," *J. Appl. Phys.*, vol. 94, pp. 2516-2523, 2003.
- [77] J. Xu, M. Howson, B. Hickey, D. Greig, E. Kolb, P. Veillet and N. Wiser, "Superparamagnetism and different growth mechanisms of Co/Au (111) and Co/Cu (111) multilayers grown by molecular-beam epitaxy," *Physical Review B*, vol. 55, pp. 416, 1997.
- [78] L. Piraux, J. George, J. Despres, C. Leroy, E. Ferain, R. Legras, K. Ounadjela and A. Fert, "Giant magnetoresistance in magnetic multilayered nanowires," *Appl. Phys. Lett.*, vol. 65, pp. 2484-2486, 1994.
- [79] A. E. Berkowitz, J. R. Mitchell, M. J. Carey, A. P. Young, S. Zhang, F. E. Spada, F. T. Parker, A. Hutten and G. Thomas, "Giant magnetoresistance in heterogeneous Cu-Co alloys," *Phys. Rev. Lett.*, vol. 68, pp. 3745-3748, 1992.
- [80] A. E. Berkowitz, J. R. Mitchell, M. J. Carey, A. P. Young, D. Rao, A. Starr, S. Zhang, F. E. Spada, F. T. Parker, A. Hutten and G. Thomas, "Giant magnetoresistance in heterogeneous Cu-Co and Ag-Co alloy films," *J. Appl. Phys.*, vol. 73, pp. 5320-5325, 1993.

- [81] T. L. Kline, Y. H. Xu, Y. Jing and J. P. Wang, "Biocompatible high-moment FeCo-Au magnetic nanoparticles for magnetic hyperthermia treatment optimization," *J. Magn. Magn. Mater.*, vol. 321, pp. 1525-1528, 2009.
- [82] Y. Ueda, S. Ikeda, Y. Mori and H. Zaman, "Magnetoresistance and magnetism in Fe-Cu alloys produced by electrodeposition and mechanical alloying methods," *J. Mater. Sci. Eng. A- Structural Materials Properties, Microstructure, and Processing*, vol. 217, pp. 371-375, Oct 30, 1996.
- [83] C. Rizal and Y. Ueda, "Magnetoresistance effect of a compositional modulated Fe-Cu-Ni films," in *17th International Conference on Magnetic Films and Surfaces (ICMFS)*, Kyoto, Japan, 2001, pp. 27-28.
- [84] J. P. Wang, W. Shen and J. Bai, "Exchange coupled composite media for perpendicular magnetic recording," *IEEE Trans. Magn.*, vol. 41, pp. 3181-3186, 2005.
- [85] W. K. Shen, A. Das, M. Racine, R. Cheng, J. H. Judy and J. P. Wang, "Enhancement in magnetic anisotropy for hcp-structured Co alloy thin films through Pt addition," *IEEE Trans. Magn.*, vol. 42, pp. 2945-2947, 2006.
- [86] J. Q. Xiao, J. S. Jiang and C. L. Chien, "Giant magnetoresistance in the granular Co-Ag system," *Phys. Rev. B*, vol. 46, pp. 9266-9269, 1992.
- [87] K. Takanashi, J. Park, T. Sugawara, K. Hono, A. Goto, H. Yasuoka and H. Fujimori, "Giant magnetoresistance and microstructure in Cr/Fe and Cu/Co heterogeneous alloys," *Thin Solid Films*, vol. 275, pp. 106-110, 4/1, 1996.
- [88] P. Allia, M. Baricco, M. Knobel, P. Tiberto and F. Vinai, "Giant magnetoresistance in joule heated Cu/Co ribbons," *J. Magn. Magn. Mater.*, vol. 140-144, Part 1, pp. 617-618, 2, 1995.
- [89] Y. Ueda and M. Ito, "Magnetoresistance in Co-Cu alloy films formed by electrodeposition method," *Jpn. J. Appl. Phys.*, vol. 33, pp. L1403, 1994.
- [90] N. Kataoka, H. Takeda, J. Echigoya, K. Fukamichi, E. Aoyagi, Y. Shimada, H. Okuda, K. Osamura, M. Furusaka and T. Goto, "GMR and microstructure in bulk Au/Co nanogranular alloys," *J. Magn. Magn. Mater.*, vol. 140-144, pp. 621-622, 2, 1995.
- [91] J. Q. Xiao, J. S. Jiang and C. L. Chien, "Giant magnetoresistance in nonmultilayer magnetic systems," *Phys. Rev. Lett.*, vol. 68, pp. 2472, 1992.
- [92] S. Ikeda, T. Houga, W. Takakura and Y. Ueda, "Magnetoresistance in $(\text{Co}_x\text{Fe}_{1-x})_{20}\text{Cu}_{80}$ granular alloys produced by mechanical alloying," *Mater. Sci. Eng. A*, vol. 217, pp. 376-380, 10/30, 1996.
- [93] M. Guan and E. J. Podlaha, "Electrodeposition of Au-Co alloys and multilayers," *J. Appl. Electrochem.*, vol. 37, pp. 549, 2007.
- [94] R. F. Soohoo, *Magnetic Thin Films*. New York: Harper and Row, 1965. Ch.7, pp. 93-128
- [95] L. Néel, "Anisotropie magnétique superficielle et structures d'orientation," *J. Phys. Radium*, vol.15, pp. 225-239, 1954.
- [96] S. Taniguchi and M. Yamamoto, "A note on a theory of the uniaxial ferromagnetic anisotropy induced by cold work or by magnetic annealing in cubic solid solutions," *Jpn. Inst. of Metals (Nippon Kinzoku Gakkaishi)*, vol. 19, pp. 269-281, 1954.

- [97] J. P. Wang, "FePt magnetic nanoparticles and their assembly for future magnetic media," *Proceedings of the IEEE*, vol. 96, pp. 1847-1863, 2008.
- [98] Y. Ueda, H. Adachi, W. Takakura, C. Rizal and S. Chikazawa, "Magnetoresistance effect and magnetoanisotropy of Co/Cu multilayered films prepared by electron beam evaporation," *Phys. Stat. Solidi C: Conf.*, vol. 1, pp. 1752-1755, 2004.
- [99] K. Spörl and D. Weller, "Influence of annealing on structure and magnetic anisotropy of Au/Co multilayers," *J. Magn. Magn. Mater.*, vol. 101, pp. 217-218, 10, 1991.
- [100] A. Murayama, K. Hyomi, J. Eickmann and C. M. Falco, "Strain dependence of the interface perpendicular magnetic anisotropy in epitaxial Co/Au/Cu (111) films," *Phys. Rev. B*, vol. 60, pp. 15245, 1999.
- [101] T. G. M. Rijks, R. Coehoorn, M. J. M. De-Jong and W. J. M. De Jonge, "Semiclassical calculations of the anisotropic magnetoresistance of NiFe-based thin films, wires, and multilayers," *Physical Review B*, vol. 51, pp. 283, 1995.
- [102] M. Park, Y. Hong, S. Gee, D. Erickson and B. Choi, "Magnetization configuration and switching behavior of submicron NiFe elements: Pac-man shape," *Appl. Phys. Lett.*, vol. 83, pp. 329, 2003.
- [103] M. Ziese and M. J. Thornton, *Spin Electronics*. Springer Verlag, 2001. Ch.4, pp.71-88.
- [104] B. D. Cullity and C. D. Graham, *Introduction to Magnetic Materials*. Piscataway, N.J.; Hoboken, N.J.: IEEE; Wiley, 2009. Ch.4, pp.133-149.
- [105] S. Chikazumi, Ed., *Physics of Magnetism*. Malabar, FL: Krieger, 1978. Chs. 13 and 14.
- [106] S. Chikazumi, C. D. Graham, *Physics of Ferromagnetism*. Oxford, Oxford University Press, 1997. Ch. 1, pp.7.
- [107] M. Kitada, "Magnetoresistance and microstructure of sputtered Au-Co thin films," *J. Magn. Magn. Mater.*, vol. 208, pp. 244-250, 2000.
- [108] P. Ohresser, J. Shen, J. Barthel, M. Zheng, C. V. Moha, M. Klaua and J. Kirschner, "Growth, structure, and magnetism of fcc Fe ultrathin films on Cu (111) by pulsed laser deposition," *Phys. Rev. B*, vol. 55, pp. 3696-3706, 1999.
- [109] D. S. Geoghegan, A. Hütten, K. H. Müller and L. Schultz, "Magnetoresistance of melt-spun Au-Co," *J. Magn. Magn. Mater.*, vol. 177-181, pp. 1478-1479, 1, 1998.
- [110] Z. Liang Bao and K. L. Kavanagh, "Aligned Co nanodiscs by electrodeposition on GaAs," *J. Cryst. Growth*, vol. 287, pp. 514-517, 1/25, 2006.
- [111] C. Scheck, P. Evans, R. Schad, G. Zangari, J. Williams and T. F. Isaacs-Smith, "Structure and magnetic properties of electrodeposited Ni films on n-GaAs(001)," *J. Phys.: Condens. Matter*, vol. 14, pp. 12329, 2002.
- [112] L. B. Valdes, "Resistivity measurements on germanium for transistors," *Proc. Inst. Rad. Eng.*, vol. 42, pp. 420-427, 1954.
- [113] E. Kolb, M. J. Walker, E. Vélú, M. A. Howson, P. Veillet, D. Greig, J. P. Renard and C. Dupas, "Giant magnetoresistance of dissymmetrical Co/Au multilayers," *J. Magn. Magn. Mater.*, vol. 156, pp. 377-378, 4/2, 1996.

- [114] H. Okamoto, T. Massalski, T. Nishizawa and M. Hasebe, "The Au-Co (gold-cobalt) system," *J. Phase Equilibria*, vol. 6, pp. 449-454, 1985.
- [115] C. Christides, R. Lopusník, J. Mistrík, S. Stavroyiannis and Š. Višňovský, "Effect of Au thickness on magnetoresistance and kerr spectra in Co/Au multilayers," *J. Magn. Magn. Mater.*, vol. 198, pp. 36-38, 6/1, 1999.
- [116] W. Zhang, S. H. Brongersma, O. Richard, B. Brijs, R. Palmans, L. Froyen and K. Maex, "Influence of the electron mean free path on the resistivity of thin metal films," *Microelectronic Engineering*, vol. 76, pp. 146-152, 10, 2004.
- [117] B. Dieny, V. S. Speriosu, S. S. P. Parkin, B. A. Gurney, D. R. Wilhoit and D. Mauri, "Giant magnetoresistive in soft ferromagnetic multilayers," *Physical Review B*, vol. 43, pp. 1297, 1991.
- [118] S. Araki, T. Takahata and T. Shinjo, "Magnetism and magnetoresistance of Au/Co multilayers," *J. Magn. Soc. Japan*, vol. 13, pp. 339-342, 1989.
- [119] E. C. Stoner and E. P. Wohlfarth, "A mechanism of hysteresis in heterogeneous alloys," *Philos. Trans. R. Soc. London, Ser. A*, vol. 240, pp. 599-599, 1948.
- [120] T. Sugiyama and O. Nittono, "Structure and giant magnetoresistance of Co/Ag granular alloy film fabricated by a multilayering method," *Thin Solid Films*, vol. 334, pp. 206-208, 1998.
- [121] J. C. Puipe and F. Leaman, *Editors, Theory and Practice of Pulse Plating*, AESF Soc, Orlando, FL, 1986.
- [122] A. Yamada, T. Houga and Y. Ueda, "Magnetism and magnetoresistance of Co/Cu multilayer films produced by pulse control electrodeposition method," *J. Magn. Magn. Mater.*, vol. 239, pp. 272-275, 2, 2002.
- [123] C. Rizal and B. Karki, "Magnetoresistance and magnetic properties of Co/Au nanostructures prepared using oblique incidence evaporation," in *Proceedings of Soft Magnetic Materials (SMM-20)*, Kos Island, Greece, 2011, pp. 1-1.
- [124] R. M. Bozorth and H. J. Williams, "Effect of small stresses on magnetic properties," *Rev. Mod. Phys.*, vol. 1, pp. 80, 17, 1945.
- [125] E. A. M. van Alphen, P. A. A. van Heijden and W. J. M. de Jonge, "Structural and magnetic properties of Co/Ag multilayers," in *The 6th Joint Intermag Conference on Magnetism and Magnetic Materials (MMM)*, Albuquerque, New Mexico (USA), 1994, pp. 6607-6609.
- [126] L. Wang, C. Clavero, Z. Huba, K. J. Carroll, E. E. Carpenter, D. Gu and R. A. Lukaszew. (2011), Plasmonics and enhanced magneto-optics in Core-Shell Co-Ag nanoparticles. *Nano Lett.* 11(3), pp. 1237-1240.
- [127] R. M. Bozorth, *Ferromagnetism*. New York: Van Nostrand, 1947. pp.76.
- [128] P. M. Levy, Z. Shi, S. Zhang, H. E. Camblong and J. L. Fry, "Interlayer coupling and magnetoresistance of multilayered structures," *J. Magn. Magn. Mater.*, vol. 121, pp. 357-361, 3/2, 1993.
- [129] A. Yamada, C. Rizal, S. Murata and Y. Ueda, "Electric properties of Ni-Co based multilayer films produced by pulse control electrodeposition method," *Jpn. J. Appl. Surf. Fin.*, vol. 55, pp. 151-152, 2004.

- [130] T. Houga, A. Yamada and Y. Ueda, "Resistivity and magnetism of Co/Cu films produced by computer controlled pulse electrodeposition," *Jpn. Inst. Metals*, vol. 64, pp. 739-742, 2000.
- [131] C. P. O. Treutler, "Magnetic sensors for automotive applications," *Sens. Actuat. A: Phys.*, vol. 91, pp. 2-6, 6/5, 2001.
- [132] P. Boyer, D. Meñard and M. Meunier, "Nanoclustered Co-Au particles fabricated by femtosecond laser fragmentation in liquids," *J. Phys. Chem. C* 114(32), pp. 13497 (2010).
- [133] V. Y. Zenou, G. Kusinski, L. Yue and G. Thomas, "Structure and magnetic properties of nanostructured heterogeneous Au-Co alloys," vol. 38, pp. 2679-2688, 2003.
- [134] C. A. Ross, "Electrodeposited multilayer thin films," *Annu. Rev. Mater. Sci.*, vol. 24, pp. 159-188, 1994.
- [135] I. W. Wolf, "Electrodeposition of magnetic materials," *Appl. Phys.*, vol. 33, pp. 1152-1159, 1962.
- [136] C. Rizal and Y. Ueda, "Magnetoresistance effect and magnetic properties of strain induced Co/Cu multilayer films," in *3rd International Nanoelectronics Conference (INEC)*, 2010, pp. 927-928.
- [137] A. Brenner, Ed., *Electrodeposition of Alloys Principle and Practice*. Academic Press, 1963.
- [138] M. Pan, H. Liu, J. Wang, J. Jia, Q. Xue, J. Li, S. Qin, U. M. Mirsaidov, X. Wang, J. T. Markert, Z. Zhang and C. Shih, "Quantum growth of magnetic nanoplatelets of Co on Si with high blocking temperature," *Nano Lett.*, vol. 5, pp. 87-90, 12/09; 01/01, 2004.
- [139] Y. H. Xu, J. M. Qiu, J. Bai, J. H. Judy and J. P. Wang, "FeCo nanoparticles assembled film," *J. Appl. Phys.*, vol. 97, pp. 10J305-10J305-3, 2005.
- [140] C. J. Sun, Y. Wu, Z. Xu, B. Hu, J. Bai, J. P. Wang and J. Shen, "Enhancement of quantum efficiency of organic light emitting devices by doping magnetic nanoparticles," *Appl. Phys. Lett.*, vol. 90, pp. 232110, 2007.
- [141] G. Reiss, H. Brueckl, A. Huetten, J. Schotter, M. Brzeska, M. Panhorst, D. Sudfeld, A. Becker, P. B. Kamp and A. Puehler, "Magnetoresistive sensors and magnetic nanoparticles for biotechnology," *J. Mater. Res.*, vol. 20, pp. 3294-3302, 2005.
- [142] J. P. Wang and X. Yao, "Programmable spintronic logic devices for reconfigurable computation and beyond: History and Outlook," *J. Nanoelectron. Optoelectron.*, vol. 3, pp. 12-23, 2008.

Appendix A: Vibrating Dipole Moment

Figure A-1 shows a magnetic dipole moment with the magnetic moment, M , lying along the x -direction, with the angular frequency, ω , the amplitude of vibration, a , along the z -direction, and the induced voltage at $A(x, y, 0)$ of the coil. The scalar magnetic potential, $\psi(0)$, due to the magnetic dipole moment at $A(x, y, 0)$ is given as:

$$\psi(0) = H_m \times x = \frac{1}{4\pi\mu_0} \left(\frac{Mx}{r^3} \right), \quad (\text{A.1})$$

where x is the horizontal distance from the center of the dipole moment to the center of the coil along the X -axis, μ_0 is the permeability at vacuum, and r is the distance between the center of the magnetic dipole moment and the center of the coil. The scalar magnetic potential along the radial direction at point $A(x, y, 0)$ is given as,

$$\psi(z) = H_r \times z = \frac{1}{4\pi\mu_0} \left(\frac{3Mz \cos(\theta)}{r^3} \right). \quad (\text{A.2})$$

The total magnetic potential (due to the magnetic moment at $z = 0$ and the simple harmonic motion at $z = ae^{j\omega t}$, where $\mathbf{r} = ix + jy + kz$) is given as,

$$\psi(t) = \psi(0) + ae^{j\omega t} \frac{\partial \psi(0)}{\partial z} = \psi(0) + \frac{\partial}{\partial z} \left(\frac{3az(\vec{M} \cdot \vec{r})}{4\pi\mu_0 r^5} \right) e^{j\omega t}. \quad (\text{A.3})$$

A time varying Z -component of the magnetic field, H_z , at point A is given as:

$$H_z(t) = -\nabla \cdot \psi(t) = \frac{\partial \psi(t)}{\partial z} = -\frac{\partial}{\partial z} \left(\frac{3aMxz}{4\pi\mu_0 r^5} e^{j\omega t} \right) = -\frac{3aMx}{4\pi\mu_0 r^5} e^{j\omega t}. \quad (\text{A.4})$$

At the surface area, S , at point A perpendicular to the $x - y$ plane and induced voltage in the detection coil with N turns is given as:

$$V = -N\mu_0 S \frac{\partial H}{\partial t} = \frac{3NSa\omega Mx}{4\pi r^5} e^{j\omega t}. \quad (\text{A.5})$$

That is, V is sinusoidal with an angular frequency, ω . The amplitude, V_0 , is given as:

$$V_0 = kafM \quad (\text{A.6})$$

Where

$$f = \omega / 2\pi.$$

Equation (A.5) shows that the frequency of the film is proportional to the amplitude of the magnetic moment. The proportionality coefficient, k , in (A.6) is equal to

$$k = \frac{3NSx}{2r^5}. \tag{A.7}$$

The value of k is thus, determined by the location and nature of the coil. If a and f are always kept constant, the strength of the magnetization, M , of the sample can be estimated.

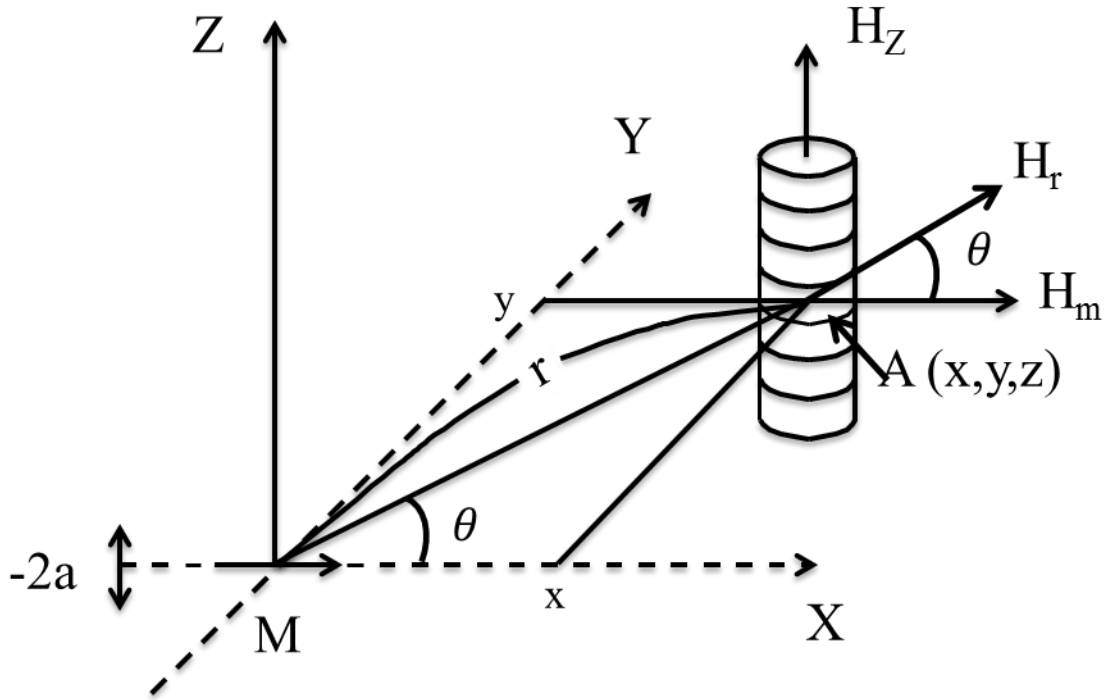


Figure A-1 Vibrating Dipole Moment

Appendix B: Measurement and Data Analysis

Each result presented in this thesis consists of experimental results carried out multiple times under the same conditions (each experiment was repeated from two to five times). In some instances the data points were plotted as is (see, for example, Fig. 2-4) while in other instances only the mean values were plotted (see, for example, Fig. 2-7).

The experimental data points were analysed using two types of statistical analysis tools: one was *R*© and the other was *KyPlot*©. Both of these tools were used to analyse data using linear and quadratic regression analysis, by utilising the method of least squares, and fitted with the models generated from the available data, thus ensuring best fits with minimum errors.

The MR ratios given in Sections 2.3.4, 3.3.3, and 4.3.3 were measured in six different measurement configurations. However, each data point in each diagram shows the average of two values, measured by changing the orientation of the current, for the isotropic multilayers and the average of two values, measured by changing the direction of the applied field and the current, for the anisotropic multilayers.

A functional relationship between strain, ε , and the degree of anisotropy, β , was established in Section 3.3.11 from a set of data containing the variables ε and β . In the process of model building, ε was the predictor variable and β was the response variable. The model fit produced the following line of regression,

$$\beta = 1.09 + 0.48 \times \varepsilon \quad (\text{B.1})$$

The relationship between the percentage change in MR ($\% \Delta MR$) and β in Section 4.3.6 was obtained from the best linear fit using *R*©.

The relationship between the composition of Co in the alloy and the composition of Co in the electrolyte in Section 5.3.1 was plotted using *KyPlot*©. The lines in the graph represent mean values of two data points (for each deposition current density) and were plotted using spline smoothing. The error bars represent standard mean errors (< 3 %) obtained from the regression analysis. Rest of the graphs in this thesis were plotted using *KyPlot*© utilizing the best linear or quadratic fits.